

MESOSCALE EDGE CHARACTERIZATION

A Dissertation
Presented to
The Academic Faculty

by

Katharine Meghan Shilling

In Partial Fulfillment
of the Requirements for the Degree
Doctor of Philosophy in the
Woodruff School of Mechanical Engineering

Georgia Institute of Technology
May, 2006

MESOSCALE EDGE CHARACTERIZATION

Dr. Thomas Kurfess, Advisor
Department of Mechanical Engineering
Clemson University

Dr. Douglas Chinn
Sandia National Laboratories

Dr. Paul Griffin
School of Industrial and Systems Eng.
Georgia Institute of Technology

Dr. William King
School of Mechanical Engineering
Georgia Institute of Technology

Dr. David Rosen
School of Mechanical Engineering
Georgia Institute of Technology

ACKNOWLEDGEMENTS

First, I would like to thank my advisor Dr. Thomas Kurfess. His ideas and guidance were imperative to the development of this thesis. I would also thank the members of my committee, Dr. Doug Chinn, Dr. Paul Griffin, Dr. William King, and Dr. David Rosen for their insight and comments. In addition I would like to acknowledge my group members Austin Chen and Laine Mears for helping me work through the theory and the details. Finally, I would like to thank my friends and family, especially Jiann Su, who provided huge amounts of encouragement and support.

The author would like to take this opportunity to thank the researchers at the National Institute of Standards and Technology (NIST) for their contributions to this work. This work was partially funded by the National Science Foundation under Grant Numbers DMI-0200331 and DMI-9988664. The government has certain rights in this material. Any opinions, findings and conclusions or recommendations are those of the authors and do not necessarily reflect the views of the National Science Foundation or the National Institute of Standards and Technology. Certain instruments or materials are identified in this paper in order to adequately specify experimental details. In no case does it imply endorsement by NIST or imply that it is necessarily the best product for the experimental procedure.

TABLE OF CONTENTS

ACKNOWLEDGEMENTS	III
LIST OF TABLES	VIII
LIST OF FIGURES	IX
SUMMARY	XIII
CHAPTER 1: INTRODUCTION AND PROBLEM STATEMENT	1
PROBLEMS RESULTING FROM POOR EDGE CONDITIONS	1
PROBLEM STATEMENT	2
OBJECTIVES	4
OVERVIEW	5
CHAPTER 2: EDGE MEASUREMENT	7
MESOSCALE MEASUREMENT TECHNIQUES	7
Optical Microscope	8
Scanning Electron Microscope	9
Scanning White Light Interferometer	11
Confocal Laser Scanning Microscope	13
Computed Tomography	15
Scanning Probe Microscopy	16
Profilometry	19
Micro-CMM	20
Digital Volumetric Imaging	21
Autofocusing Probe	22
Microfabricated Scanning Grating Interferometer - μ SGI	24
MEOSOSCALE MEASUREMENT STUDIES	25
Stereolithography	26
LIGA	27
Cutting Edge Measurement	30

Micro-Burrs	31
MESOSCALE EDGE MEASUREMENT	32
CONFOCAL LASER SCANNING MICROSCOPY	35
Operation	35
Resolution	37
3D Capability	39
Sources of Error	41
CONFOCAL MICROSCOPE FOR EDGE INSPECTION	42
Equipment	42
Settings	43
Repeatability	45
Post-Processing	45
REFERENCE ARTIFACTS	49
Test Slides	50
Lateral Test Specimen	51
Tip Characterization	51
Reference Artifact Recommendation	52
SUMMARY	57
CHAPTER 3: EDGE CHARACTERIZATION	58
EDGE CHARACTERIZATION ASSUMPTIONS	58
SIZE	59
SHAPE	61
Ellipse Representation	61
Line	66
Circle	67
Parabola	69
ABRUPT CHANGES	81
TRENDS	83
SUMMARY	86
CHAPTER 4: RESULTS	88

PROCESSING STEPS	88
Edge Orientation and Data Sectioning	89
CUTTING TOOL INSERTS	91
Chamfered Tool	93
Honed Tool	102
Tool Insert Conclusions	110
LIGA	110
STEREOLITHOGRAPHY	114
Plus-X	120
Minus-X	126
SUMMARY	129
CHAPTER 5: EDGE SPECIFICATION	130
EXISTING BURR AND EDGE CLASSIFICATION	130
Burr Types	131
Schafer's Burr Classification	131
Gillespie's Edge Quality Classification Scheme	133
Takazawa's Edge Quality Classes	135
MESOSCALE EDGE SPECIFICATION	137
Components	137
Discussion	141
SUMMARY	141
CHAPTER 6: CONCLUSIONS	142
SUMMARY	142
CONCLUSIONS	144
CONTRIBUTIONS	144
FUTURE WORK	145
CONCLUDING REMARK	147
APPENDIX A: CHAMFERED TOOL EDGE DATA	148
APPENDIX B: HONED TOOL EDGE DATA	152

APPENDIX C: SLA EDGE DATA	156
REFERENCES	158

LIST OF TABLES

Table 1: Mesoscale measurement techniques	7
Table 2: Relative costs for part measurement	35
Table 3: Resolution and pixel size by objective magnification	44
Table 4: Resulting deviations and errors from LIGA edges	113
Table 5: Best-fit shape of measurement area for SLA part built in plus-x location	121
Table 6: Best-fit shape of measurement area for SLA part built in plus-x location	126
Table 7: Overview of edge quality requirements [4; 103]	136

LIST OF FIGURES

Figure 2.1: Diagram of scanning white light interferometer	12
Figure 2.2: Confocal laser scanning microscope	14
Figure 2.3: LLNL CT system [30]	16
Figure 2.4: Typical cutting tool insert [42]	19
Figure 2.5: Autofocusing probe diagram [55]	23
Figure 2.6: Microfabricated scanning grating interferometer	24
Figure 2.7: Stereolithography grid CAD model	26
Figure 2.8: Optical microscope image of grid wall section	27
Figure 2.9: PMMA mold with present, yet undetectable outer edge [2]	29
Figure 2.10: Edge topology for LIGA part [2]	29
Figure 2.11: Tool recommendations based on edge size	33
Figure 2.12: Confocal laser scanning microscope	36
Figure 2.13: Resolution limit based on size of Airy disk [73]	38
Figure 2.14: Surface location by parabola fit	41
Figure 2.15: Zeiss LSM510 confocal microscope at NIST	43
Figure 2.16: Raw data, surface found by maximum intensity	46
Figure 2.17: Effect of surface location algorithm. Maximum intensity (a) and Center (b)	47
Figure 2.18: The proper threshold value can be selected easily, (a) has a threshold value of 28 and (b) is the same data with a threshold value of 29.	48
Figure 2.19: Examples of two filtered data sets, (a) uses a median filter, (b) uses a mean filter.	49
Figure 2.20: Top three scans of 635 μm sphere	54
Figure 2.21: Sine bar	55
Figure 3.1: Expected edge structures	59
Figure 3.2: Differentiation between edge, top, and side	61
Figure 3.3: Rotated ellipse parameters	62
Figure 3.4: Requirements for quadratic rational Bezier circle	64
Figure 3.5: Quantities for line fitting	66

Figure 3.6: Circle parameters	67
Figure 3.7: Error in center and radius vs. angle of arc of circle for several noise levels	68
Figure 3.8: Edge conditions represented by parabolas	69
Figure 3.9: Parabola parameters	70
Figure 3.10: Parameters for finding closest point on quadratic Bezier curve	72
Figure 3.11: Example of multiple solutions for u	73
Figure 3.12: Residual errors vs. noise level for parabola fitting	75
Figure 3.13: Residual errors vs. height of parabola for parabola fitting	76
Figure 3.14: Residual errors vs. angle of rotation for parabola fitting	77
Figure 3.15: Vertex and focus error vs. noise level for parabola fitting	78
Figure 3.16: Vertex and focus error vs. included angle of parabola for parabola fitting	79
Figure 3.17: Vertex and focus error vs. angle of rotation for parabola fitting	80
Figure 3.18: Parabola mimicking a line	81
Figure 3.19: Generated data with a single burr	82
Figure 3.20: Residual error from generated data with a single burr	83
Figure 4.1: Flow chart for processing of single CLSM data set	88
Figure 4.2: Flow chart for processing several CLSM data sets to obtain global trend information	89
Figure 4.3: Cylinder parameters	90
Figure 4.4: Cutting tool insert properties for (a) honed and (b) chamfered tools	92
Figure 4.5: Representative data set from tool inserts	93
Figure 4.6: Land length and height for chamfered edge	94
Figure 4.7: Measured values vs. slice number for a single chamfered tool measurement	95
Figure 4.8: Slices 9 and 16 from chamfered tool	96
Figure 4.9: Residual values vs. slice number for chamfered tool measurement	96
Figure 4.10: Average land length and height, with 2σ error bars, for chamfered tool	97
Figure 4.11: Height and land length for all measurements of chamfered tool	98
Figure 4.12: X-bar chart for land length of chamfered tool	100
Figure 4.13: S chart for land length of chamfered tool	100
Figure 4.14: Representative slices from measurement areas 4 and 8 of chamfered tool	102
Figure 4.15: Angle (θ) and radius (r) for honed edge tool insert	103

Figure 4.16: Radius and included angle for representative honed measurement area	104
Figure 4.17: Circle fit residuals for representative honed edge tool measurement area	104
Figure 4.18: Slices with residual values and radii outside of 2σ	105
Figure 4.19: Radius and included angle for all slices of all measurement areas of honed tool	106
Figure 4.20: X-bar chart for radius of honed tool, outliers removed from individual measurements	108
Figure 4.21: S chart for radius of honed tool, outliers removed from individual measurements	108
Figure 4.22: Honed edge tool data	109
Figure 4.23: LIGA edge structure measured by X-SEM [62]	111
Figure 4.24: LIGA edge measured at 150x	111
Figure 4.25: Representative fit of LIGA edge data to $70 \times 70 \times 70 \mu\text{m}$ cube	112
Figure 4.26: QQ plot of residuals vs. standard normal	113
Figure 4.27: LIGA edge data	114
Figure 4.28: Model used for hole test	115
Figure 4.29: Build locations for SLA case study	115
Figure 4.30: Location of measurement area for SLA parts	116
Figure 4.31: Edge of stereolithography part, captured at 20x	117
Figure 4.32: Edge of stereolithography part, captured at 10x	118
Figure 4.33: Line created from SLA edge data	119
Figure 4.34: Example of acceptable (a) and unacceptable (b) best-fit parabola	120
Figure 4.35: X-bar chart for x-size of SLA part built in plus-x location	122
Figure 4.36: S chart for x-size of SLA part built in plus-x location	122
Figure 4.37: X-bar chart for y-size of SLA part built in plus-x location	123
Figure 4.38: S chart for y-size of SLA part built in plus-x location	123
Figure 4.39: X-bar chart for slope of SLA part built in plus-x location	124
Figure 4.40: S chart for slope of SLA part built in plus-x location	124
Figure 4.41: Data representative of change in y-size	125
Figure 4.42: X-bar chart for x-size of SLA part built in minus-x location	127
Figure 4.43: X-bar chart for y-size of SLA part built in minus-x location	128

Figure 4.44: X-bar chart for slope of SLA part built in minus-x location	128
Figure 5.1: Burr size characteristics [97; 98]	131
Figure 5.2: Quadrant-based classification scheme and corresponding classes of allowable edge quality proposed by Schafer [100]	132
Figure 5.3: Classified edge conditions [100]	132
Figure 5.4: Allowable edge conditions with Level E, "Break edges ____ to ____ mm minimum" [102]	134
Figure 5.5: Allowable edge conditions with Level F, "Round edges ____ to ____ mm radius" [102]	135
Figure 5.6: Edge condition not allowed by Level F, "Round edges ____ to ____ mm radius" [102]	135
Figure 5.7: Edge size representation	139
Figure 5.8: Example edge shapes for curved (R), chamfered (C), and undefined (U) edges	139
Figure A.1: Slices 1-6 for representative chamfer data	148
Figure A.2 Slices 7-12 for representative chamfer data	149
Figure A.3: Slices 13-18 for representative chamfer data	150
Figure A.4: Slices 19-20 for representative chamfer data	151
Figure B.1: Slices 1-6 for representative honed data	152
Figure B.2: Slices 7-12 for representative honed data	153
Figure B.3: Slices 13-18 for representative honed data	154
Figure B.4: Slices 19-20 for representative honed data	155
Figure C.1: Slices 1-6 for representative SLA data	156
Figure C.2: Slices 7-10 for representative SLA data	157

SUMMARY

In mesoscale manufacturing desired dimensional and surface characteristics are defined, but edge conditions are not specified in design. The final edge conditions that exist in mesoscale objects are created not only by the manufacturing process but, because of their size, also by part handling procedures. In these parts, the concern is not only with burrs, which can be formed by some mesoscale manufacturing processes, but also with the shape and size of the edge. These properties are critically important as the edge can constitute a large percentage of the smallest features of mesoscale objects. For example, if a very sharp edge with a radius of $25\text{ }\mu\text{m}$ ($\sim 0.001\text{ in}$) exists on both sides of a part, this edge constitutes 50% of a $100\text{ }\mu\text{m}$ feature, a reasonable size for a mesoscale structure. Undefined edge geometry can result in measurement, assembly, and operational difficulties.

Due to the potential problems caused by edge conditions, it is desirable to have the ability to measure and characterize the edge conditions of parts. This thesis considers mesoscale measurement tools to provide an edge measurement tool recommendation based on edge size and properties. A set of analysis techniques is developed to determine the size and shape of the measured edge, locate any local inconsistencies such as burrs or dents, and track trends in calculated parameters as a function of edge position. Additionally, a standard method for communicating design requirements is suggested in order to differentiate between acceptable and unacceptable edges.

CHAPTER 1: INTRODUCTION AND PROBLEM STATEMENT

In recent years there has been a significant increase in the number of manufacturing methods able to produce mesoscale parts ($> 100\text{ }\mu\text{m}$) with microscale features (100 nm to $100\text{ }\mu\text{m}$). Parts produced by these processes are found in a variety of devices, including the small mirrors used in digital projection displays and ink jet heads for printers. The processes span a wide range of fields, from traditional manufacturing such as turning and milling to extended lithography methods such as LIGA (and layer-based manufacturing methods like stereolithography). Generally speaking, the processes used to create mesoscale objects are not part of mature fields.

In traditionally manufactured components, final edge conditions are critical to performance. Burr removal is a chief concern because of the problems burrs can create with the measurement, assembly, and operation of the component. Unfortunately, edges are rarely specified or measured for mesoscale components. The edges of mesoscale parts are particularly difficult to measure because most of the common measurement tools are unable to properly collect edge data. This inability has been reported as a hindrance to obtaining correct dimensional measurements [1; 2].

Not only does proper edge measurement and characterization contribute to more accurate dimensional measurements, it can be used to identify problems in assembly or operation, and provide process feedback regarding edge condition.

PROBLEMS RESULTING FROM POOR EDGE CONDITIONS

Consideration of edge conditions is a critical component of traditional manufacturing, especially removal of burrs. A burr, by definition, is “a thin ridge of

material produced in cutting or shaping metal” [3]. Burrs can cause a multitude of problems with assembly and operation of systems. Gillespie [4] outlines several problems caused by improperly finished edges:

- Interference fits in assembly.
- Jammed mechanisms.
- Scratched mating surfaces may allow seals to leak.
- Increased or changed friction.
- Increased wear on moving parts.
- Short circuits.
- Metal contamination.
- Excessive stress concentrations.
- Edge craters, fractures, and crumbling from initially unsmooth edges.
- Turbulence and nonlaminar flow.
- Inaccurate dimensional measurements.

Although Gillespie is referring to objects of traditional scale, it is clear that many of these problems can adversely affect mesoscale objects and assemblies. Of particular note is the last bullet, inaccurate dimensional measurements, which has been seen in the mesoscale measurement studies presented in Chapter 2.

PROBLEM STATEMENT

In traditionally manufactured objects, edges are designed to have a radius or chamfer in order to eliminate burrs. Burrs are thin, usually triangular, ridges along the edge of the workpiece. In traditional manufacturing, they are often caused by shearing sheet metal, trimming forgings and castings, or machining. These burrs can cause several

problems. First, they can interfere with assembly. Second, they can cause jamming, misalignment, and short circuits. Third, they can reduce the fatigue life of the component by causing stress concentrations. Finally, if the burrs become dislodged during operation, they can interfere with machine operation or contaminate lubricants.

In mesoscale manufacturing desired dimensional and surface characteristics are defined, but edge conditions are not specified in design. The final edge conditions that exist in mesoscale objects are created not only by the manufacturing process but, because of their size, also by part handling procedures. In these parts, the concern is not only with burrs, which can be formed by some mesoscale manufacturing processes, but also with the shape and size of the edge. These properties are critically important as the edge can constitute a large percentage of the smallest features of mesoscale objects. For example, if a very sharp edge with a radius of $25\text{ }\mu\text{m}$ ($\sim 0.001\text{ in}$) exists on both sides of a part, this edge constitutes 50% of a $100\text{ }\mu\text{m}$ feature, a reasonable size for a mesoscale structure. Undefined edge geometry can result in measurement, assembly, and operational difficulties.

Many mesoscale measurement tools are top-down systems created to measure nominally planar surfaces. An edge is inherently non-planar, and thus difficult to measure properly with these systems. If the edge of the surface of interest is not measured properly, the resultant measurement will likely be incorrect. The larger the edge is, the larger the potential measurement error. In addition to measurement errors, an edge that protrudes beyond the desired part size can affect both fit and operation. Burrs or loose particles on the part have the potential to create serious problems during operation.

Due to the potential problems caused by edge conditions, it is desirable to have the ability to measure and characterize the edge conditions of parts. An ideal measurement and characterization strategy enables process monitoring as well as part qualification. In order to differentiate between acceptable and unacceptable conditions, edges must be considered and specified in design.

OBJECTIVES

The goal of this thesis is to provide a basis for the consideration of edges of mesoscale parts. This requires examination of three areas; edge measurement, edge characterization, and edge specification.

The first objective of this work is to provide a recommendation for a tool to measure mesoscale edges. Mesoscale edges for this work are defined as 1 to 200 μm in size. In order to provide a measurement method recommendation, it is necessary to analyze the ability of current mesoscale measurement techniques to collect edge data. The recommendation must be based on edge properties, including material and expected size.

The second objective of this work is to develop a set of tools to characterize a mesoscale edge. Tools are needed to provide 2D information (e.g., size and shape) from edge segments, to recognize local disturbances, and to identify trends resulting from changes across the entire edge. Collected data are used to demonstrate the characterization tools.

The final objective of this work is to provide the foundation for a mesoscale edge specification method. An edge specification method is important because it allows the designer to communicate acceptable edge conditions in a standard format. It is necessary

to create an edge specification method specifically for mesoscale edges because their size creates concerns that are not considered in other methods.

OVERVIEW

Mesoscale edges, for this work, can range from one to hundreds of micrometers, depending on the process used to create the part. Because of the wide range of sizes, there does not exist a single measurement tool that is capable of measuring all mesoscale edges. In Chapter 2, the wide variety of mesoscale measurement tools are discussed. Recommendations are made for selection of a measurement tool based on edge size and material properties. The measurement tool selected for this work is discussed in detail, and measurement results are presented. The need for a well-known object to serve as a validation tool is also discussed.

With the edge measured, it is desirable to formulate a methodology for describing and characterizing the edge. In this work, the method for representing the edge segment is critical. In addition to handling edges of different shapes and sizes, the representation method needs to allow for a straightforward comparison between the edges, for both 2D and 3D properties. The characterization methodology is described in Chapter 3.

In Chapter 4, the characterization techniques developed in Chapter 3 are applied to data collected by methods described in Chapter 2. Studies of several objects are presented.

Not only is it important to understand the shape and the size of the edges, it is necessary to provide a method for describing desired edge conditions. Several of these methods exist in the field of deburring and edge finishing. However, the assumptions made in these classification schemes are unacceptable for mesoscale edges. In Chapter 5,

existing edge classification schemes are combined with knowledge of mesoscale edge requirements to form a proposed mesoscale edge specification scheme.

Finally, Chapter 6 provides conclusions based on the work presented in the previous chapters. A list and description of intellectual contributions is provided. Recommendations for future work in this field are made.

CHAPTER 2: EDGE MEASUREMENT

MESOSCALE MEASUREMENT TECHNIQUES

Tools for mesoscale metrology are mainly derived from techniques of the semiconductor industry or are scaled-down versions of macro-scale measurement tools. These tools can be grouped according to contact type, output type, and commercial availability. A list of the tools that are reviewed in this section is shown in Table 1.

Table 1: Mesoscale measurement techniques

Commercial Systems	Non-Contact	Systems Under Development	Non-Contact
	Optical Microscopy		Autofocusing Probe (DVD)
	Scanning Electron Microscopy		Micro-Scanning Grating Interferometer
	Atomic Force Microscopy (Non-Contact)		
	Scanning White Light Interferometry		
	Confocal Laser Scanning Microscopy		
	Tomography		
	Contact		
	Atomic Force Microscopy (Sliding, Tapping)		
	Profilometry		
	Micro-Coordinate Measuring Machine		
	Destructive		Output
	Digital Volumetric Imaging		image
			2.5 dimensional data
			3 dimensional data

For mesoscale edge measurement, there are certain characteristics which are desirable in a measurement tool. It is desirable that the tool is non-destructive because, depending on the process, edges may need to be measured for all parts; which is not possible with a destructive tool. Second, it is desirable that the tool require no modifications of the test part, such as coating with a conductive material. Third, it is desirable that the tool be non-contact. The edges of mesoscale parts are small and even a

moderate amount of force placed over such a small area could cause significant elastic or plastic deformation, neither of which is desirable. Also, the static forces between the contacting probe and the object could create measurement error. Additionally, contacting tools require that the part be fixtured. Fixturing a mesoscale part without any effect on the dimensions is not trivial. It is also desirable that the output from the measurement system be a cloud of data points rather than an image. The edges are 3D, and 3D interpretation of a 2D image is prone to error and uncertainty. All tools are discussed with these desired characteristics in mind.

Optical Microscope

Optical microscopes are used to inspect relatively large mesoscale objects such as those fabricated from the LIGA process, which has the capability of producing parts that are a few mm tall. The underlying operating principles for optical microscopes include spatial resolution determined by the Rayleigh criterion and detected edge sharpness determined by a combination of hardware (e.g., lens type, CCD camera) and lighting conditions (e.g., coaxial lighting, ring lighting).

Optical microscopes have the advantage of being fast and non-destructive. Rarely do test parts have to be modified (e.g., coated with a conductive material) from their original form. The ultimate limiting factor for resolution of optical metrology hardware is diffraction and the ability of the microscope to produce images with clear intensity changes in order to accurately detect edges. Resolution can be as good as $0.5\text{ }\mu\text{m}$ [5]. Often locating the edge of a part is difficult, as observed location varies with lighting condition, noise, and assumptions made in the edge position algorithm [6]. Other

significant errors of optical techniques typically stem from interference, resonance, shadowing, secondary reflections, and lens distortions [7; 8].

Ceremuga [2] characterizes an optical microscope that is heavily used for MEMS inspection, and his results show good agreement with the stated specifications of the machine. Other topics analyzed in his work include choosing the best location on intensity curves of optical microscopes to determine the actual location of an edge. Also, as discussed in an earlier chapter, the optical microscope had difficulty locating the edge of the parts and required the use of a correction factor in reporting object dimensions.

An important limitation of optical microscopes for MEMS inspection is inability to acquire true 3D data. Some optical microscopes are integrated with software that uses image processing techniques to determine the z-height at which the scan is taking place. The current state-of-the-art software uses a projected Ronchi grid to determine the height at which the microscope is focused in one region of the image [9]. If the region selected has multiple focus points (i.e., the region selected is not all on one plane), the algorithm assigns the average value for the Z-height. Further edge detection algorithms are run to extract X and Y data from the microscope image. This technique, in theory, produces 3D data from an image; however, the algorithms used after finding the Z-height in one location of the image assume that all of the data are on the same plane. Thus, the data acquired from vision systems such as these can be characterized as 2.5D data sets.

Scanning Electron Microscope

One of the primary tools used for analysis of mesoscale devices is the scanning electron microscope (SEM). SEMs are capable of producing high resolution images of conductive objects on the angstrom scale. SEMs operate by scanning a focused beam of

high energy electrons across a conductive sample contained in a vacuum. As the electron beam hits the conductive surface, secondary electrons are knocked loose. These secondary electrons are counted by and used to create an image of the sample. SEM resolution can be better than 10 nm [5].

Postek [10] provides a thorough analysis of the capabilities of SEMs. To summarize, the accuracy of the images captured is highly dependent on machine capability and the specific part being examined. Beam-sample interactions (i.e. charging) are shown to greatly influence the results of any measurement taken with the device. Additionally, despite the high resolutions of the SEM, the output is typically generated from the electron detector and displayed on a cathode ray tube rastered in synchronization with the electron beam. The final result is a 2D image on a screen. Since coordinate data not an output from the SEM, performing any analysis other than line width measurements directly with the SEM software becomes difficult. Thus, SEMs are ideal for visualizing mesoscale parts and edges, but are inadequate tools for quantitative analysis of mesoscale devices.

Marchman [11] raises the issue of determining edge position from the SEM image. An edge appears as an intensity change in the image. Depending on the image analysis technique used, the location of the edge can vary greatly. Marchman [11] found this can cause as much as a 100 nm difference for a 500 nm line width measurement.

An alternative SEM process is called X-SEM. This process is destructive and requires the sample to be cross-sectioned. The cross-section is then imaged in an SEM. Often this technique is used to determine sidewall and height characteristics [12]. Lagerquist et al. [13] discusses use of the X-SEM process to characterize top-down SEM

images, which require interpretation of intensity and are sensitive to sidewall geometry. The X-SEM technique could potentially be used for mesoscale edge measurement; however, it requires the destruction of the sample to collect edge profiles.

In a study concerning edge characteristics, Marschner et al. [14] describes a method of using two top-down SEM images, one taken with a small tilt angle (3° to 6°), to gain information regarding top edge rounding and the sidewall profile. The result of the two scans found to be very sensitive to the algorithm used to combine the two images. However, when compared to X-SEM images, the results did not match well.

Scanning White Light Interferometer

A third method of mesoscale part inspection is scanning white light interferometry (SWLI). Although initially developed for surface characterization, such as finding surface roughness, it is currently being used to make dimensional measurements of mesoscale parts. White light interferometers have sub-nanometer resolution in the scanning direction, at best sub-micron resolution in the lateral directions, and can be used on a multitude of parts with different surface finishes [15].

The interferometer works on the principle of interference. Within the objective, a light beam is split, with one beam going to the object surface and the other to a reference surface. These light waves bounce back and interfere with each other, forming a pattern of light and dark bands, called fringes. For the SWLI, Figure 2.1, a piezoelectric crystal is used to create small movements in the objective perpendicular to the surface of interest. As the reference surface within the objective moves, the result of the combination of the reflected light varies. Several images are captured and then

combined. Based on the interference pattern, or fringes, and the wavelength of light employed, it is possible to extract coordinate data. [16]

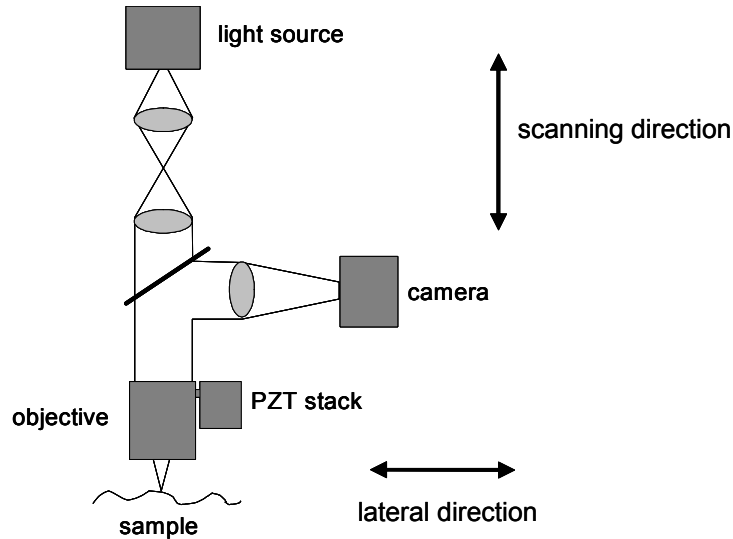


Figure 2.1: Diagram of scanning white light interferometer

White light is commonly used in scanning interferometers because it allows for higher resolution by comparing data from multiple wavelengths. Additionally, it is possible to resolve step height changes greater than one quarter of the wavelength [17].

The SWLI has the ability to quickly measure step heights changes and deflections. When integrated with an image processing system, a SWLI can also provide lateral dimensions. However, the lateral resolution of commercially available systems is lacking, except when equipped with high power objectives which severely limit the field of view. Additionally, these tools are limited in their ability to measure sloped surfaces. The largest slope that can be identified is typically around 30° with a 100x objective [18]. As the objective power decreases, the largest identifiable slope also decreases.

Despite these limitations, white light interferometry is heavily used to determine surface roughness, structural support analysis, deflection curve verification, and material

property analysis of mesoscale parts [1922]. Shilling [23] has also used SWLI to analyze mesoscale devices with relative success. In the study, SWLI provided good results except at the edges of parts which tended to be non-square. Because of the slope limitations inherent in the machine, data is not gathered from the edges of a part, resulting in an incomplete data set. The inability of the SWLI to collect data from sloping surfaces renders it incapable of providing edge data.

Confocal Laser Scanning Microscope

Confocal Laser Scanning Microscopy (CLSM) combines a confocal microscope with a scanning system in order to image an entire specimen. A CLSM has four basic elements – point illumination, point detection, a confocal lens system, and a method of scanning the image. Although scanning can be performed in several different ways, it is most often done by moving the beam which alleviates focus problems caused by objective lens scanning and is faster than specimen scanning [24].

Confocal microscopy is different from conventional microscopy in that it creates an image point by point. Also, because of the double pinhole lens system, when the sample is moved out of the focal plane of the objective, the light intensity at the detector decreases rapidly, in effect, allowing the system to focus on a single plane. By moving focus location, a different plane can be imaged. With a scanning system added, the system has the ability to scan multiple times on different imaging planes, resulting in a 3D data set. Structure dimensional measurements are in the range of micrometers with nanometer accuracy.

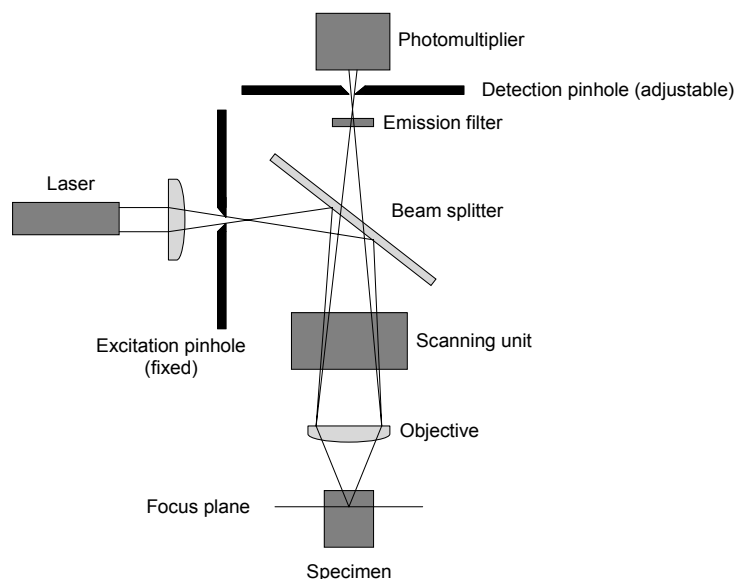


Figure 2.2: Confocal laser scanning microscope

The CLSM has been used to quantify changes in surface morphology and film thickness of polymer coatings during the UV degradation process [25]. Additionally, work has been done to use this system to perform 3D analysis of microstructures such as micro end mills and hot embossing tools, both with overall dimensions on the order of 1mm [26]. One of the most important advantages found was the ability of the microscope to measure steep slope, up to almost 90° on a part with minimal surface roughness. This measurement requires a high resolution, high numerical aperture objective, which has a limited lateral measuring field unsuitable for measuring the entire object. Because of this, a stitching procedure was used to combining scans taken with several objectives.

The CLSM has been found in this work to have the ability to measure mesoscale edges. This tool is discussed in greater detail in a succeeding section of this chapter.

Computed Tomography

Computed tomography is a radiographic technique that provides a method for locating and sizing planar and volumetric detail in three dimensions. Computed tomography machines measure a complete set of line-integrals over the designated cross-section [27]. Computers are used to reconstruct an image of a cross sectional plane through an object from the collected data. Stacking these images provides a three-dimensional image appropriate for making quantitative measurements.

A system for computed tomography has been developed by Aracor [28] that provides 25 μm resolution and 2 μm accuracy for a 10 mm diameter object. By using algorithms to calculate edge position within a pixel, the accuracy is approximately an order of magnitude lower than the resolution. At high resolution, it takes approximately one day to image a part.

Lawrence Livermore National Laboratory (LLNL) is currently developing a system that combines x-radiography with computed tomography to non-destructively provide internal detail of mesoscale structures [29]. The goal of the LLNL system is 1 μm resolution over a 1 mm field of view, with each scan taking tens of minutes. In order to achieve this goal, an extremely small, bright x-ray source and/or a high collection efficiency x-ray imaging optics are required. A synchrotron is used as the x-ray source. The design of the imaging optic requires special considerations because the x-rays can penetrate most optical materials and mirrors. It was decided that Wolter multilayer imaging optics would be used to improve collection efficiency [30]. The system, as designed, is shown below in Figure 2.3.

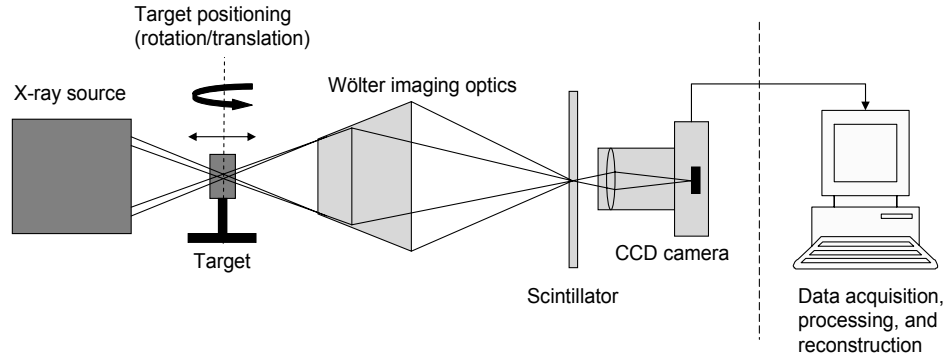


Figure 2.3: LLNL CT system [30]

Computed tomography provides non-destructive characterization of internal structures of mesoscale devices. Also, it can be used to inspect metallic or non-metallic, solid or fibrous, smooth or irregular surfaced specimen. The results can be used for quality control, flaw detection, dimensional measurement, and reverse-engineering [31]. There is the possibility, however, of artifacts in the resulting image that are due to the physics and mathematics of the system and can not be removed. Additionally, complete scans are quite time consuming and require a significant amount of data processing.

The high-resolution computed tomography system, under development by LLNL, could be a potential measurement tool for larger mesoscale edges in the future.

Scanning Probe Microscopy

Scanning probe microscopes (SPMs) offer an alternative to non-contact techniques. SPMs are characterized by their high resolution (sub-angstrom). The two most widely used SPMs are the scanning tunneling microscope (STM) and the atomic force microscope (AFM). The older of the two technologies, the STM, was developed in 1982 [32]. This technique uses a metallic probe that is brought into close proximity of a conductive surface so that a small current flows between the probe and surface. The current is held constant by a feedback control scheme, allowing the probe to track the

height of the surface [7]. Structural, chemical, and electrical properties can be measured with an STM. Sub-angstrom resolution is attainable in the normal direction of the surface, and angstrom-scale resolution is attainable in the lateral directions of the surface.

Atomic force microscopy (AFM) is the newer SPM technology and retains the resolution of the STM, but is not limited to conductive surfaces [33]. The measurements of an AFM are performed with a sharp probe that collects a series of line scans across the surface of a part. The topography of the part is measured by bringing the probe close to the specimen and measuring the repulsive and attractive forces on the probe tip. In the z-direction, AFMs have high sensitivity, typically with a resolution of 0.05 nm. Resolution in the x and y-directions are also high, ranging from 2-10 nm [34].

An AFM is capable of working in both a contact and non-contact mode to collect surface data. In contact mode, the method of data acquisition is similar to a profilometer where the probe tip slides along the surface of the specimen and the relative height changes are measured. Shear stresses that arise from sliding the probe tip across the surface of a part can be eliminated by using a setup in which the probe tip oscillates as it traverses across the surface (i.e., tapping mode). AFMs can also be used in a non-contact method, where the Van der Waals forces between the probe tip and specimen are measured and converted to coordinate data. Though having the advantage not contacting the surface of the specimen and eliminating tip erosion [35], this method has lower resolution and is less stable than either the sliding or tapping modes.

Atomic force microscopes have been used to measure micro- and mesoscale parts with limited success. Sidewalls of parts with heights of 2 μm have been successfully measured with AFMs [13; 36; 37]. The tip geometry (e.g., conical, flared, etc.) is shown

to have a significant impact on the measurement results. Probes with sharp tips have been developed that have a full cone angle of less than 5° and have been used to successfully characterize bottom corner (foot) geometry of lines and trenches [38].

There are certain limitations to SPMs, particularly in measuring larger parts. STMs, as previously mentioned, are limited to parts with conductive surfaces. Electronic inhomogeneities can also have significant effects on the topographical image of the probe [32]. Vibrations in the probing mechanism also limit gap width stability which, in turn, can affect the fidelity of the measurements. All SPMs are limited, in the same sense as white light interferometers, to the maximum, measurable slope changes in a surface or between surfaces. When features with perpendicular sidewalls are scanned, the data typically exhibit a slope or curtain that is actually not present [39]. The height of measurable features is also limited to the probe length which is typically less than $10\text{ }\mu\text{m}$ in commercial systems. This limitation severely prohibits the inspection of most mesoscale edges.

Profilometry

Profilometry is similar to scanning probe microscopy, but on a large scale. A probe, often with a spherical tip, traverses the sample, maintaining contact by applying a force at the probe tip. The movement of the probe in the lateral and vertical directions is recorded and converted into a surface profile. Profilometers are frequently used to determine surface texture, form error, angle of surface inclination, and dimensions of traditionally manufactured parts. The vertical resolution of the Form Talysurf is 10 nm [40]. Lateral resolution is not considered as critical for these machines, and is on the order of 1 μm .

At Kennametal, a cutting tool insert manufacturing company, profilometers are used to measure the hone radius and chamfer of the cutting edge [41]. A typical chamfered edge cutting tool, used primarily on ceramic tool materials, would measure to be a 20° chamfer angle, 125 μm land length, and a hone radius of 12.5 μm . A typical tool is shown in Figure 2.4.

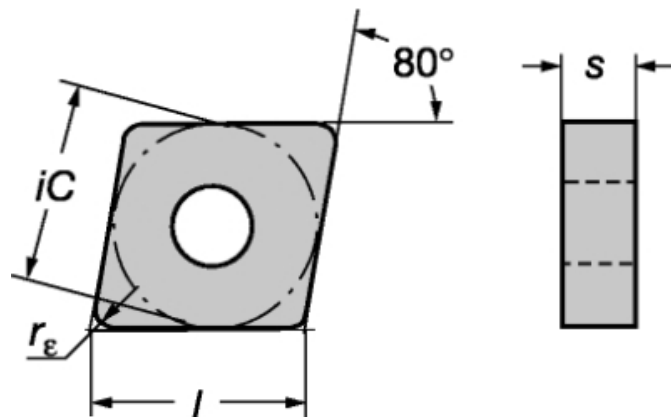


Figure 2.4: Typical cutting tool insert [42]

Kennametal uses a diamond stylus to trace the radius of the cutting edge, specifically the hone radius. In the case where the geometry of the tool edge includes a

chamfer, each trace is extended to measure the land length of the chamfer, the angle of the chamfer, and the hone radius. Typically, in order to fully characterize the tool, several traces are made at the leading edge, nose and trailing edge.

Although profilometry can be used to measure large edges of other mesoscale objects, the properties of this tool make it less than ideal for softer or inconsistent surfaces.

Micro-CMM

Small-scale coordinate measuring machines (CMMs) have and are being developed for their use in geometric characterization of mesoscale objects [43]. These devices have working volumes up to 400 by 400 by 100 mm [44]. Sub-micrometer uncertainties are being targeted with nanometer resolution [45].

Various approaches are being taken to the scaling down of components of a traditional CMM [4649]. The greatest potential advantage of these machines will be their ability to acquire true 3D data from microfabricated parts. One of the main issues to be addressed is the size, quality and calibration of the probe tip used for inspection. The smallest size probes to date are on the order of 0.1 mm [50]. In addition, the design of a sensing system to detect the small displacement forces of the probe is a challenge. Many systems are in a developmental stage with one commercial system, the F25 by Carl Zeiss Industrial Metrology available.

The Zeiss F25 3D coordinate measuring machine has a measuring volume of one cubic decimeter. The uncertainty for this volume is 250 nm at a resolution of 7.5 nm. The machine is designed for stylus diameters of 200 to 500 μm , with stylus tip diameters of 50 to 700 μm , with a free shaft length of up to four mm. The probe forces are less than

0.5 mN/ μ m. In addition to the touch probe, the F25 incorporates an optical sensor for 2D metrology [51].

Like the computed tomography machine, the micro-CMM holds promise for the future of mesoscale metrology. It is too soon to determine how the micro-CMMs will respond to the challenge of mesoscale edge measurement.

Digital Volumetric Imaging

Digital volumetric imaging (DVI) was developed by Resolution Sciences, Inc. to offer an alternative to traditional histotechnology, the process of fixing and embedding tissues in wax, sectioning them, and viewing the sections one by one. DVI allows a sample to be viewed either a section at a time, or as a 3D image.

The first step in DVI is to embed the sample into an appropriate solid. This solid block is then mounted into the machine, and material is removed until the sample is reached. A 2D image of the sample face is taken with resolution of 0.22 to 4.4 μ m, depending on the objective being used. Different lighting conditions are available for different types of analysis. After the image is captured, the sample is moved to the cutting station, where a microtome removes a thickness from 0.25 to 4.4 μ m with a diamond knife. The sample is then retracted to the imaging station using a technique that has reproducibility of better than 100 nm. The process of imaging and slicing the sample is repeated until the entire block has been imaged. The set of 2D images are then converted into a 3D image set. Special software allows the either individual slices or the entire data set to be viewed [52]

An important benefit of this type of analysis is that it produces a 3D data set with fairly high resolution. Additionally, interior defects can be located and analyzed.

Unfortunately, DVI is a destructive technique and for this technology to be applied to samples made from hard materials, the process needs to be improved. The selection of the proper embedding material, additives to promote surface adhesion, sample orientation, sample location within the block and the embedding technique are all critical in imaging hard materials.

Several trials have been conducted to image mesoscale samples, specifically those made with the LIGA process [53]. A 664 μm nominal diameter gear was imaged to provide information regarding absolute dimensions and sidewall angles. A full 3D data set was collected. It was noticed that striations were created in the surface because of degradation of the cutting surface of the knife. These striations created noise problems at the surface boundaries, causing edge measurement problems. Also, a brass ball bearing was imaged as a potential calibration artifact. The image contained good surface detail, showing a spiral pattern, typical of the process used to manufacture ball bearings. However, adhesion of the sample to the embedding material was a problem, with the ball bearing releasing from the sample block during sectioning.

This method, although allowing for a 3D data set from a mesoscale object, is not ideal for edge characterization for several reasons – the technique is destructive, smearing at boundaries has been observed, and poor sample adhesion can cause the measurement process to fail.

Autofocusing Probe

The autofocusing probe, shown in Figure 2.5, combines a 6-axis micro-positioning stage with an autofocusing laser probe commonly found in CD and DVD players to create a non-contact measurement system. The autofocusing laser probe works

on the principle that when laser light is projected through specific optics (beam-splitter, quarter-waveplate, and objective) and reflected (through quarter-wave plate and on to photodiode array), it will take on different shapes depending on if the light is focused on the sample surface. The sample surface can then be focused by actuating the objective lens through the use of a voice coil until the focused shape is achieved. Because the lens position is proportional to the current passed through the voice coil, a measurement of the current will provide displacement information [54]. The displacement of a number of discrete points can be collected into an image showing the surface of the sample [55].

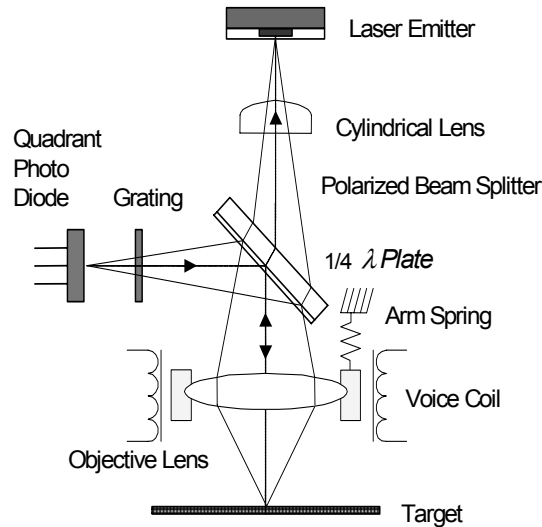


Figure 2.5: Autofocusing probe diagram [55]

Similar to many measurement techniques that rely on reflected light, the DVD probe can not focus on areas in which the light is not directly reflected back to the probe, such as in the case of chamfers and fillets, ruling out its' ability to measure mesoscale edges. Additionally, relatively high reflectivity is required to achieve focus.

As a further example of the probes inability to measure edges, the probe has been used in a preliminary study to image micro-gears on the order of 1 mm in diameter, created using the LIGA process. The results achieved using the DVD probe were

compared to those using SWLI. Different results were obtained from each of the two systems, with the results from the DVD probe underestimating the amount of material present. It is believed that this is a result of the inability of the system to focus on surfaces at an angle to the probe [55].

Microfabricated Scanning Grating Interferometer - μ SGI

The microfabricated scanning grating interferometer, or μ SGI, has been developed to allow for parallel scanning of dynamic and static devices [56]. The μ SGI is based on traditional laser interferometry, but operates on the micro-scale. The system, manufactured using standard silicon processing techniques, measures distance by using a reflective diffraction grating. The diffraction grating is located on a transparent substrate with a micro-lens, fabricated using a reflow technique. The light reflected from the diffraction grating and the sample is collected by photo diodes. The system is shown in Figure 2.6.

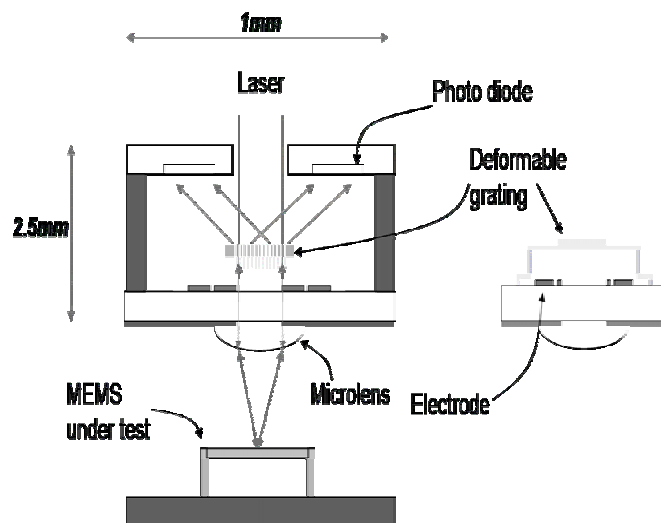


Figure 2.6: Microfabricated scanning grating interferometer

As with all interferometers, the intensity change due to displacement takes the shape of a sine wave. The diffraction grating is deformable to allow higher vertical displacement sensitivity by staying within the linear portion of the sine wave, allowing for a vertical resolution of 0.5 nm. The lateral resolution is 3.6 μm [57].

This system has a couple of distinct advantages over traditional interferometry. First, it has been designed to be produced in an array to allow for faster inspection by using several μGSI in parallel. Second, the system has the ability to make both static and dynamic measurements. Hall and Degertekin [58] show initial results for the displacement measurements of acoustic transducers. However, these tools are currently limited to changes in step height proportional to the wavelength of light used in the laser source, which limits the range of measurement for the device. In this case, the step height is limited to one quarter of the wavelength of the Helium-Neon laser, or 158 nm. Noise filtering has also been an issue in the development of the μSGI .

Unfortunately, although this system behaves well for measurement of planar mesoscale surfaces, it has the same problems with non-planar surfaces as the white-light interferometer. Thus, the μSGI is unsuitable for mesoscale edge measurement.

MEOSOSCALE MEASUREMENT STUDIES

Mesoscale part manufacturing is a relatively new and broad field. Parts can be made using scaled-down conventional methods such as milling, by additive processes such as stereolithography, or by a lithographic process like LIGA. In previous studies, measurement of parts created by stereolithography and LIGA has been performed. Both cases presented similar problems with regard to obtaining an accurate line width measurement due to edge shape.

Stereolithography

In stereolithography, a computer aided design (CAD) model of the desired part is split within a software package into very thin layers. Each individual layer is drawn on a vat of photosensitive polymer resin using a laser which cures (solidifies) the resin. After one layer is drawn, the resin vat lowers and the next layer is drawn. This procedure is repeated until the entire part has been created.

The laser penetrates the resin to a certain depth, with decreasing intensity at deeper levels and at distances away from the center of the laser spot. In order for the layers to fuse and create a solid part, the layers must be thinner than the depth of penetration so that each scan penetrates into the previous layer. This serves to cure more than one layer at a time. Because the top layers of the part do not have as many (or any) scans above them as the previous layers, they are not cured as completely. The exposure from the laser is directly related to the amount of material cured [59].

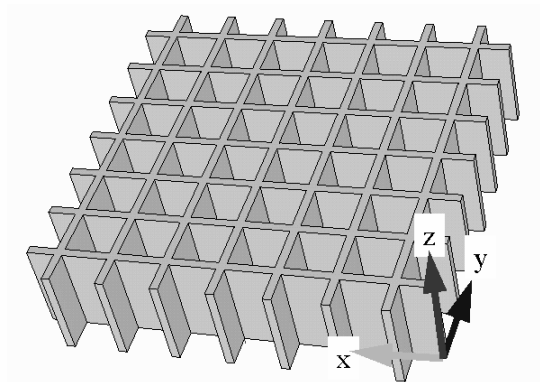


Figure 2.7: Stereolithography grid CAD model

In a study [1], grid parts (shown in Figure 2.7) were produced. Each part was built up along the z-axis (layers in the x-y plane). After building and curing, these top of

the grid walls were measured using scanning white light interferometry (SWLI). The width of these walls was significantly lower than expected (20 μm measured, 70 μm expected). This was due to the conical shaped tip on the top of the grids, as seen in Figure 2.8, a result of incomplete curing [1].

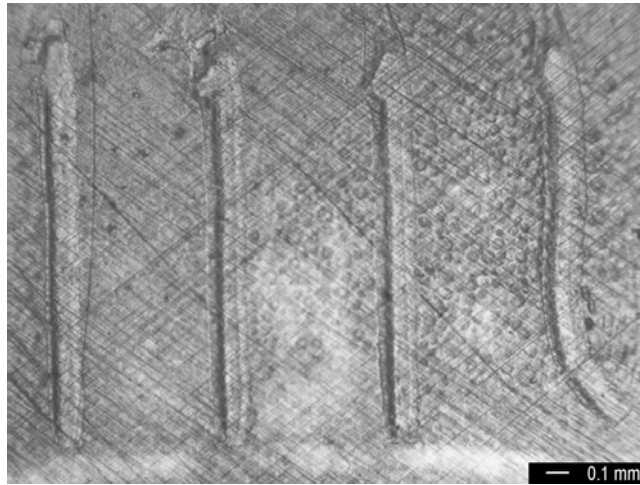


Figure 2.8: Optical microscope image of grid wall section

It is desirable to understand the actual wall thickness of these parts, as opposed to the width at the very top of the wall. In order to accomplish this using 2D metrology, it is necessary to characterize the shape of the edges in order to add a correction factor to the SWLI measurements.

LIGA

Mesoscale parts can also be manufactured using the LIGA process. The abbreviation LIGA comes from the German description of the process to produce these microstructures; lithography (lithographie), electroplating (galvanoformung) and molding (abformung). A mask is created and x-rays from a synchrotron are sent through a mask and onto an x-ray sensitive layer of PMMA (polymethylmethacrylate) resting on a silicon base. The mask blocks the x-rays, leaving some of the PMMA exposed. The unexposed

PMMA is then removed using an organic developer. The remaining material serves as a negative when the wafer is plated, usually with nickel, and lapped. The plated parts are then either released from the silicon base or used as a mold [60]. The final processing step of lapping has been known to create uneven pressure distribution over the surface of the work piece, with a higher pressure at the edge of the work piece. This can create roll-down shape errors at the edges [61]. A LIGA part cross sectioned and measured with a SEM [62] was found to have a rounded top edge.

Ceremuga [2] measured LIGA microstructures with a programmable optical microscope. He found that with some microstructures, the actual feature size could not be measured due to the lack of contrast available for image processing. In these cases, the outer edge of the structure could not be detected consistently. Figure 2.9 shows an image of PMMA photoresist under the best achievable lighting conditions. A faint darker line is present between the void and material side edges. This edge is undetectable to the edge detection algorithms. The contrast between this outer, “void-side” edge and the titanium part does not produce a large enough grayscale gradient to define the edge consistently. The “material-side” edge of the PMMA, on the other hand, is always present and well-defined, and can thus be measured.

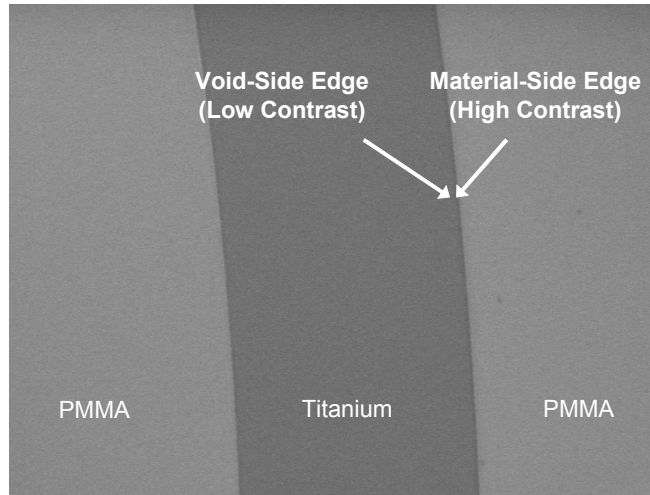


Figure 2.9: PMMA mold with present, yet undetectable outer edge [2]

Ceremuga suggests using a correction factor to account for the difference between the inspected and actual values. Ceremuga found his correction factor by estimating a radius of the top edge from an SEM image, as shown in Figure 2.9. Adjustment of the lighting conditions also provided a second method for measuring edge width [62]. An average edge width of $2.5\ \mu\text{m}$ was measured using this technique. A more accurate method of finding the correction factor, or edge width, is desirable.

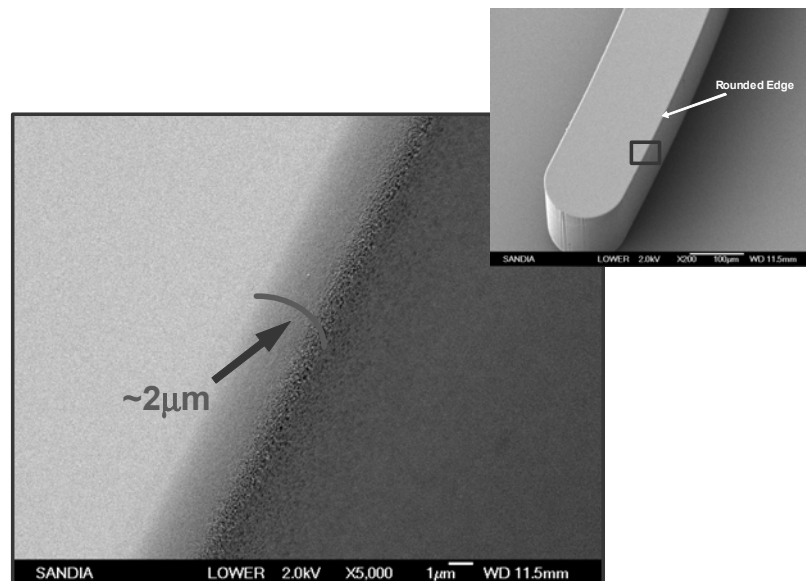


Figure 2.10: Edge topology for LIGA part [2]

Cutting Edge Measurement

Cutting tool edges are critical to performance. Edge sizes range from microscale, including cutting tools for plastic web materials and diamond tools for precision applications, to mesoscale for traditional cutting tool inserts. Cutting edges are often measured to quantify tool wear.

Initially, many tool measurement systems relied on an optical comparator to project the tool edge profile for inspection [63]. Because the optical comparator lacks the ability to see fine detail, video-based systems were developed. The video-based systems have been used to provide profile and wear measurements for cutting tools [63] [64]. Video systems are used both in-process as well as offline.

Li et al. [65] were interested in measuring, with nanoscale precision, the edge radius of diamond tools used in wafer fabrication. Indentations of the tool profile were created by pressing the tools into a piece of copper. The radii (45 nm to 1 μm) of the tool indentations were successfully measured using an atomic force microscope (AFM). Lucca and Seo [66] have used a specially configured AFM to directly measure a diamond cutting tool with an edge radius of 0.25 μm (± 0.002 μm).

Weckenmann and Nalbantic [67] use two sensors to precisely measure the macro shape of an entire tool and the micro shape of the cutting area. The macro shape does not require high resolution, but does require a large measurement area. This requirement is met by a fringe projection system with a measuring range of 40 x 40 x 16 mm, a lateral resolution of 39 μm and a vertical resolution of 4 μm . The micro shape of the cutting area, including the cutting edge and radius, requires a higher resolution. For this measurement a white light interferometer with a measuring range of 2.1 x 2.1 x 100 mm,

a lateral resolution of 3 μm and a vertical resolution of 0.2 μm was used. This combination of tools allows for a complete inspection of a cutting tool insert in a total of four measurement positions.

Measurement techniques able to measure wear in cutting tools used for plastic web materials were evaluated by Budinski [68]. For these cutting tools, it is required that the tool be accurate enough to measure a “sharp” edge (2 - 4 μm radius). Six techniques were evaluated. Metallographic sectioning allows precise measurement with an optical microscope but requires destruction of the tool. Silicon replicas were sectioned with each section measured independently. This technique is limited in the ability of the sectioning technique to create a planar surface as non-planar surfaces create measurement error. Profilometry produces acceptable results except in some cases, however where the load was excessive the stylus plastically deformed the edge. Optical microscopy and weighing of the tool are able to successfully measure the wear volume and mass, respectively. Atomic force microscopy was attempted, but it took excessive amounts of time (up to 8 hr) to set-up the measurement. It was concluded that profilometry with a low stylus load and silicon sectioning are the measurement techniques of choice.

Micro-Burrs

Dow and Scattergood [69] have shown that burrs have a tendency to occur when a grain boundary is crossed due to non-uniform material response. This problem is especially present in mesoscale and microscale objects. Generally a grain size at least two orders of magnitude smaller than feature size is selected to provide uniformity of material response.

Miniature tools, as small as 50 μm in diameter, are used to fabricate mesoscale and microscale parts. Significant burring has been known to occur using hard metal micro end mills [70]. Because burrs on these small parts are difficult to remove, and removal can damage the workpiece, Lee and Dornfeld [71] have studied the formation of micro-burrs and their minimization through process control. Several measurement methods are used to measure height and thickness including contact profilometry, optical microscope method and CMM. In their study, Lee and Dornfeld measured burr height using a surface profilometer because it was observed that the burrs had regular shapes and high hardness. The measured burrs had a height from 5 to 25 μm .

When investigating burr formation from drilling miniature holes, Stein and Dornfeld [72] measured burr height and thickness using a microscope at 100X. The measurements were taken at 90° intervals around the hole. The measured burrs had a height from approximately 70 to 160 μm and thicknesses from 40 to 60 μm .

MESOSCALE EDGE MEASUREMENT

Although there are many tools available for measurement of mesoscale objects, most of these tools are capable only of quantification of planar surfaces. In addition to tools which are new or under-development, the micro-CMM and the computed tomography machine, there are several measurement techniques that have the potential to measure mesoscale edges. Due to the range of edge sizes and materials in mesoscale objects, it is impossible to recommend just one tool for edge measurement. There are three tools which are recommended for non-destructive measurement of mesoscale edges; the AFM, the CLSM, and the profilometer.

Figure 2.11 shows tool recommendations based on edge size. It is not possible to calculate exact size limitations because of tool to tool variations in set-up, noise levels, and resolution. Additionally, all edges of the same size may not possess the same material properties, which is an important consideration in selection of a measurement tool. The measurement tool must be able to collect a sufficient number of data points from the entire edge. This number varies with part properties (i.e., surface roughness) but generally it is desirable to collect 10s of points as a minimum.

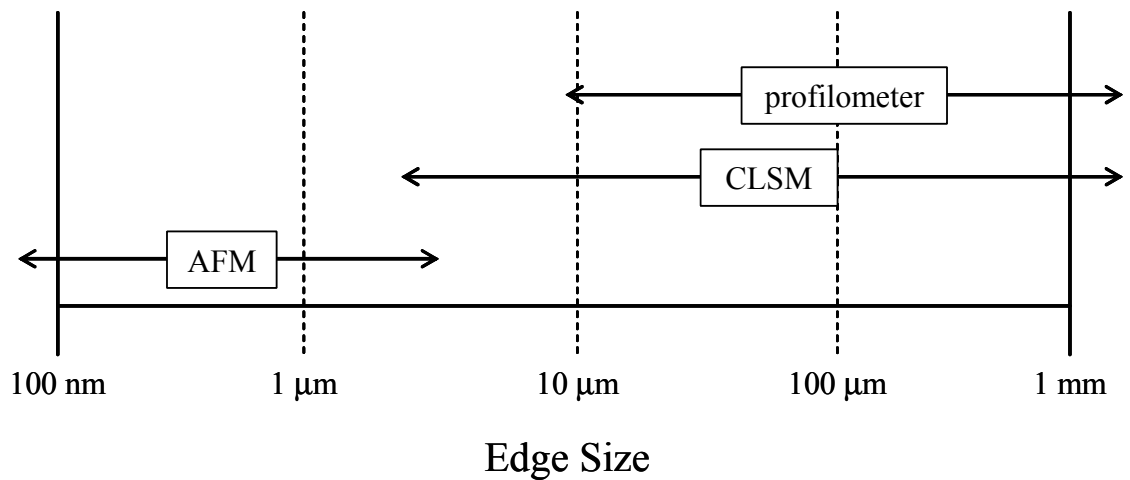


Figure 2.11: Tool recommendations based on edge size

The use of the AFM to measure mesoscale edges is limited by probe length and machine set-up. AFM probe lengths, generally less than 10 μ m, limit the ability of the AFM to measure larger mesoscale edges. In addition to probe length consideration, the ability of the AFM to hold and properly orient the object under consideration must be considered.

For parts with larger edges, a profilometer can be used to collect edge data. The profilometer is most successful with edges made from hard materials. The applied contact force may result in an unacceptable deformation of the edge for softer materials.

The resolution of the profilometer must also be considered for edges on the smaller end of the profilometer range shown in Figure 2.11.

Because the CLSM is not a stylus-based instrument, it is not limited by probe length or contact force. However, the use of reflected light limits resolution and the ability to measure non-reflective surfaces. The CLSM spans the widest range of mesoscale object edges, and will be used exclusively in this work.

The relative cost of measurements with each of the tools may also be a deciding factor and are reported in Table 2. To compute the cost, the capital cost of an average machine is depreciated over 5 years. It is assumed that the machine runs 50 weeks/year at 40 hours/week. The total measurement time is the time required to collect data from 10 measurement areas on a single part. For the profilometer, which takes a line scan as opposed to a measurement area, the measurement area is considered to be 10 line scans. The AFM requires approximately five minutes set-up time and two minutes measurement time for a single measurement area. This results in a total of 70 minutes for 10 measurement areas on a single part. For the CLSM, it takes 2 minutes set-up time and 4 minutes measurement time per measurement area, resulting in 60 minutes for a single part. The profilometer requires 30 seconds set-up time and 30 seconds measurement time per scan line, a total of 100 minutes per part. The total cost for measurement for the AFM and CLSM are comparable, while the cost to measure a part with the profilometer is significantly less, due to the low capital cost.

Table 2: Relative costs for part measurement

Tool	Capital Cost	Cost/Minute	Minutes/Part	Cost/Part
AFM	\$160,000	\$0.26	70	\$18.20
CLSM	\$200,000	\$0.33	60	\$19.80
Profilometer	\$20,000	\$0.033	100	\$3.30

CONFOCAL LASER SCANNING MICROSCOPY

Although confocal laser scanning microscopy (CLSM) is based on basic optical microcopy principles, it has special properties which give the system the advantage of providing the capability to measure 3D surfaces. The operating principles and unique properties of CLSM are discussed in this section.

Operation

The basic CLSM, as shown in Figure 2.12, contains five major components: a light source, objective lenses, a scanning unit, a pinhole, and a detector. In its operation, coherent light from the light source is focused on the excitation pinhole, which acts as a spatial filter. The light then passes through the pinhole and optics, including the objective, to form a single spot on the specimen. The light is reflected off of the specimen, back through the objective, where the beam splitter allows the light to pass through the detection pinhole and into the detector. The confocal microscope can be broken down into four sections: the point source, the confocal lens system, the scanning unit, and the detection system.

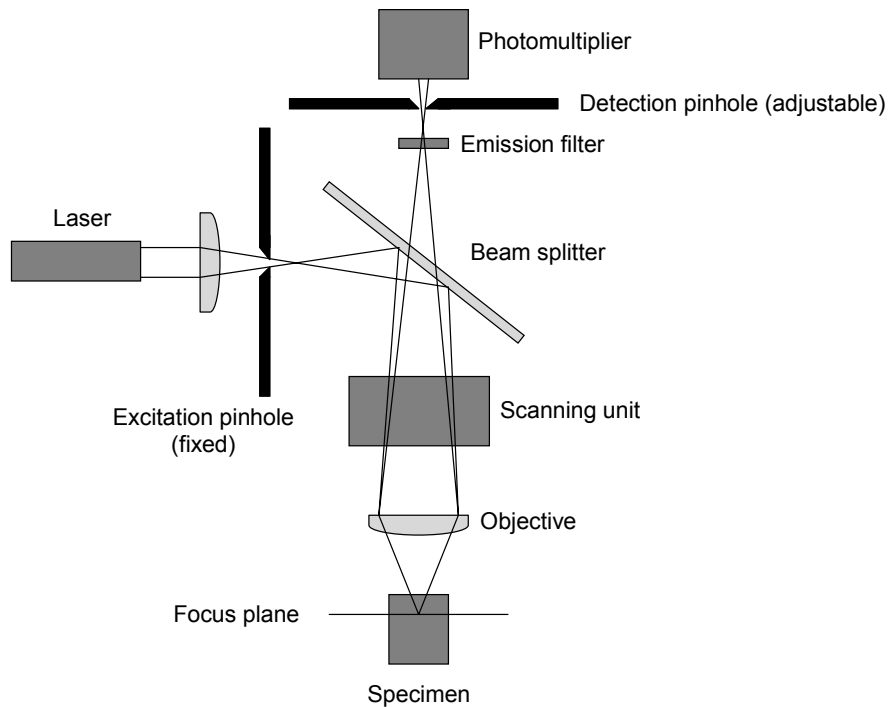


Figure 2.12: Confocal laser scanning microscope

The illumination system delivers the point light source for imaging the specimen. The light is often a laser, providing a cheap, bright, single frequency source. The design is greatly simplified by using a single frequency. The most important characteristic of the light source is that the intensity be stable. If the intensity is not stable, the location of the surface of the specimen can be misjudged. In addition to the light source, the illumination system contains lenses to focus the light on a pinhole to provide a point of light.

Before reaching the specimen, the photons pass through an objective system. After reflecting off of the specimen the photons pass back through the same system, making the system “confocal.” Because the objective lenses are used for both imaging and receiving, the effect of lens aberrations is increased. In order to limit the effects of aberrations, the objective lenses must meet stringent requirements to be used in a

confocal system. Many consider the objective lenses a sticking point for further confocal microscope development [24].

After the photons pass back through the objective lens system, they go through another pinhole and into a photodiode, which counts the number of photons being reflected. The size of the detection pinhole can affect the signal to noise ratio and the resolution of the system. A smaller pinhole transmits fewer photons, lowering the signal (and thus decreasing the signal to noise ratio) while giving better in-plane resolution. A larger pinhole does the opposite, increasing the signal to noise ratio, but at the cost of a worse resolution. In practice, the size of the pinhole is often determined by an equation dependent on the pinhole lens characteristics.

Because imaging is point-by-point, a scanning system is necessary. Although scanning can be performed in several different ways, it is most often done by rastering the beam as this alleviates focus problems caused by objective lens scanning and is faster than specimen scanning [24].

Resolution

Spacing of measurement points and size of diffraction pattern affect the resolution of the system. For optical systems such as the CLSM, light interacting with a small object produces a pattern known as an Airy disk, presented in Figure 2.13(A). Resolution is the ability of the measurement system to resolve between two adjacent objects.

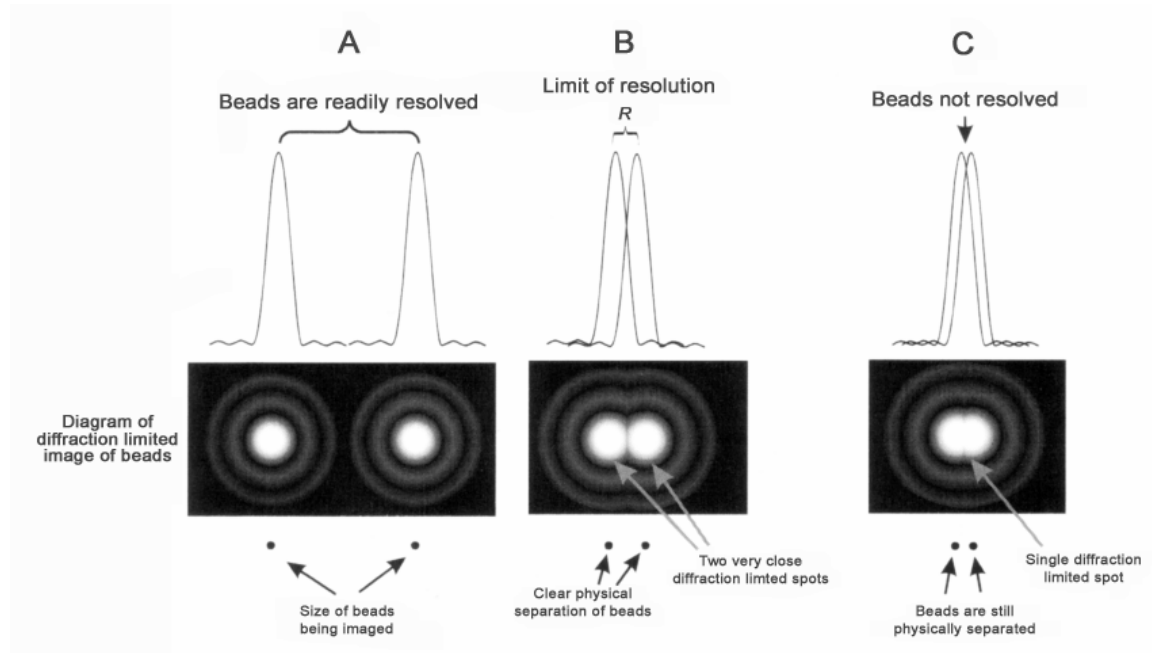


Figure 2.13: Resolution limit based on size of Airy disk [73]

The size of the Airy disk is dictated by the wavelength of the light (λ) and the numerical aperture (NA) of the objective lenses. The relationship between the radius of the Airy disk ($r_{lateral}$) and system properties is given in Equation (2.1). The radius of one Airy disk defines the minimum distance at which two discrete objects can be resolved, as shown in Figure 2.13(B). This calculation assumes ideal conditions with a lens free of aberrations. For real systems the resolution is close to, but does not exceed, this ideal value [73].

$$r_{lateral} = \frac{0.61\lambda}{NA} \quad (2.1)$$

A commonly used equation to describe axial resolution is presented as Equation (2.2) [74]. For all cases presented, the specimen medium is air, thus the index of refraction (η) is 1. Note that changes numerical aperture have a much greater affect on axial resolution than changes in any of the other variables.

$$r_{axial} = \frac{1.4\lambda\eta}{NA^2} \quad (2.2)$$

The Airy disk pattern also affects the perception of small objects. If an object is smaller than Airy disk, it is usually perceived as larger than its actual size. Objects on the order of 0.05 μm can be overestimated by as much as 10 times, resulting in a measured object on the order of 0.50 μm [73].

It is possible to collect data from points that are closer together than the minimum resolution of the system. For continuous surfaces, such as edges, the ability to measure roughness and waviness is limited by resolution. However, resolution does not effect form measurement.

3D Capability

The depth response of the COSM is very important because it gives the microscope the very valuable ability to create a 3D image of an object.

The peak intensity (i.e. the greatest number of reflected photons) occurs when the beam is focused on the plane of the sample. When the sample is moved out of the focal plane of the objective, the reflected light is defocused and does not pass directly through the pinhole, as a result photon count at the detector decreases rapidly. This permits the system to image only the objects present on a single focus plane, as those out of focus do not reflect photons back to the detector. With a set of scanned images of the same x-y

area at different heights along the z axis, this characteristic can be used to determine local surface height through one of several detection algorithms [75].

The simplest detection algorithm is to search for the maximum pixel value. The set of scanned images are almost like slices through the object at different heights. If the photon count, or intensity, reaches a maximum when focused, then for a particular location in the x-y plane, the height of the image which contains the maximum value can be considered the height of the object at that x-y location. However, the sensitivity of this method is limited by the axial scan sampling period, or the z-distance between scans.

In order to overcome this limitation, a parabola can be fit to the highest pixel intensities. Several of the highest intensities are plotted vs. their axial scan height, as shown in Figure 2.14, and a parabola is fit. The surface height is defined as the height that corresponds to the maximum intensity of the parabola. This results in sensitivity greater than the axial resolution of the microscope. Surface position using a parabola fit has been determined to be on the order of 1 nm [75].

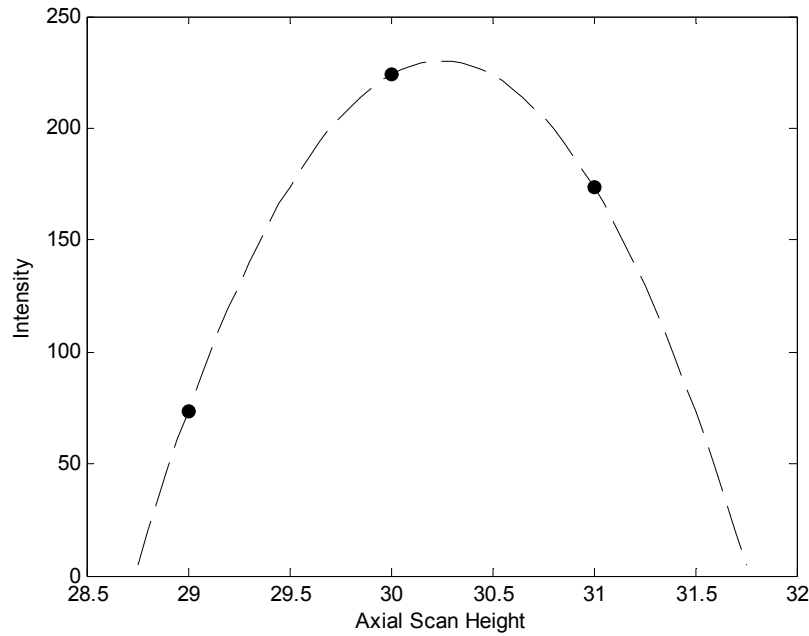


Figure 2.14: Surface location by parabola fit

Sources of Error

Several sources of error exist for CLSM. These can be grouped into three areas, counting statistics, noise within the CLSM machine, and stray light. The first source of error is due to limited accuracy in counting photons described by Poisson statistics [76]. If the same measurement is repeatedly made, the number of photons counted varies according to a Poisson distribution based on the average number of photons counted (n) having a standard deviation (σ) given in Equation (2.3). If $n=100$ and $\sigma=10$, this is referred to as 10% statistics [77]. To increase the precision to 1%, the average number of photons counted must be 100,000. Thus, it is desirable to provide the greatest amount of light possible to the sample in order to increase the average number of photons, lowering the relative standard deviation.

$$\sigma = \sqrt{n} \quad (2.3)$$

Within the machine, the photomultiplier tube is a significant source of error. The photomultiplier tube, in very simple terms, turns absorbed photons into a voltage. The output voltage is proportional to the number of absorbed photons. Noise in the photomultiplier tube can be caused by the process that converts the photon to a photoelectron, dark current, the effect of Poisson statistics on the voltage produced by a single photon, and sampling mismatch of the analog to digital converter. Pawley [78] provides an in-depth analysis of the noise sources related to the photomultiplier tube. The stability of the output of the laser can be a source of noise in CLSM. However, for most commercial systems the variations are very low and contribute little to overall noise levels. Similarly, the electrical noise present in the system circuitry is only a minor contributor to the overall noise level.

Stray light from outside the focus area that is detected is considered a source of noise. Decreasing the size of the pinhole decreases the amount of stray light that enters the photomultiplier, increasing the apparent resolution. However, decreasing the pinhole size also attenuates the amount light detected from the focused area.

CONFOCAL MICROSCOPE FOR EDGE INSPECTION

Equipment

A Zeiss LSM510 confocal microscope, as shown in Figure 2.15, was used in this work to collect data. The microscope is property of the National Institute of Standards and Technology (NIST) in Gaithersburg, Maryland.

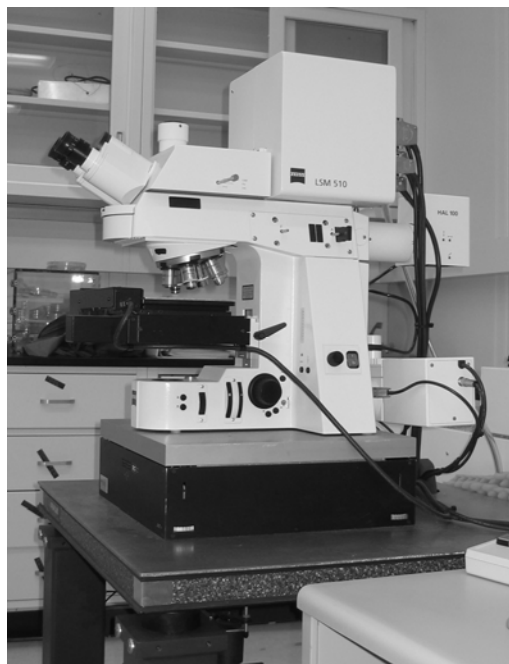


Figure 2.15: Zeiss LSM510 confocal microscope at NIST

For the data presented in this work, a Helium-Neon (HeNe, wavelength 543 nm) laser was used in combination with a 5x, 10x, 20x, 50x, or 150x objective, depending on the desired measurement. The objective, in combination with the image size and system magnification, dictates the x-y resolution. In addition to choosing the light source and the objective, there are other variables which must be defined for each measurement. The distance between each scan in the z-direction (voxel height) is variable. Additionally, a suitable detector gain and pinhole size must be selected.

Settings

The number of pixels captured along with the size of the objective and the zoom determines the size of the x-y pixels. For simplicity, the number of points captured remains 512 by 512 and the zoom constant, allowing the objective to solely determine the point spacing. If a smaller point spacing is desired the number of pixels can range up to 2048 by 2048 for the same area. Additionally, the zoom and objective can be changed

for an even finer pixel size. Lateral resolution is calculated using Equation (2.1). For all measurements in this dissertation, the point spacing and resolution for each objective in Table 3 hold true.

Table 3: Resolution and pixel size by objective magnification

Objective Magnification	Numerical Aperture	Axial Resolution	Lateral Resolution	Point Spacing
5x	0.15	34 μm	2.2 μm	3.6 μm
10x	0.30	8.4 μm	1.1 μm	1.5 μm
20x	0.50	3.0 μm	0.66 μm	0.89 μm
50x	0.50	3.0 μm	0.66 μm	0.35 μm
150x	0.95	0.84 μm	0.35 μm	0.12 μm

In addition to resolution settings, it is necessary to choose a bit-depth for data collection. All data sets in this work were collected as 8-bit values, meaning that the photon count has been scaled so that the maximum is 256, and the minimum is 0.

The voxel height is determined separately for each scan. To delineate the range of scan heights, the user can select the start and end position in the z-direction. The number of slices within that z-range can be chosen to yield the desired voxel height. For this research, the voxel heights range from 0.1 to 5 μm .

A pinhole size must be selected for each scan. The optimum size of the pinhole depends on the numerical aperture (NA), the magnification of the objective in use, and the sample being measured. In most confocal measurement systems, including the LSM510, one Airy disk is the default value for pinhole size, reflecting a compromise between resolution and sensitivity. In this work, this default value was used exclusively.

In addition to the voxel and pinhole size, the detector gain must be chosen for each scan. The detector gain is set as high as possible, to allow the greatest amount of light to be detected without saturating the photomultiplier. Setting the detector gain is critical to the scanning process, and can greatly affect the resulting data set. For example, when imaging a small sphere, it is not possible to image the entire top hemisphere with a single detector gain. The detector gain needs to be set relatively low to keep from saturating the detector for the points on the top of the sphere, which are close to perpendicular to the light beam. Conversely, the detector gain needs to be set relatively high for the sides of the sphere, which are nearly parallel to the light beam. Thus, a single detector gain setting can not be used to scan the entire top hemisphere of a sphere. Similarly, multiple detector gain settings may be required parts with a significant change in slope or reflectivity over the scan area.

Repeatability

Repeatability of the system is the ability of the system to reproduce the same results under the same measurement conditions. The repeatability of the CLSM has not been determined, but is an important quantity to understand if the CLSM is implemented for edge measurement.

Post-Processing

The raw data of a cutting tool insert with a honed edge, displayed in Figure 2.16, was captured by the Zeiss LSM software. The software allows for processing of the raw data and conversion into a 3D surface representation.

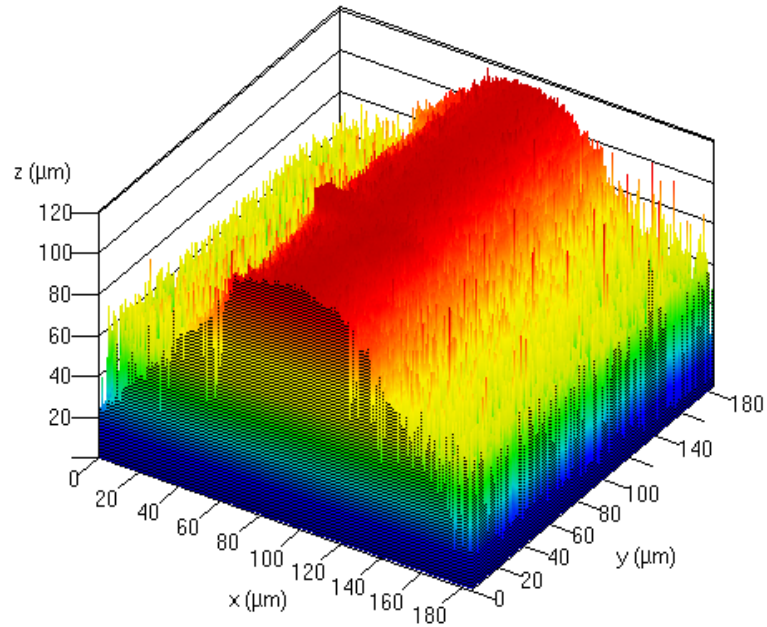


Figure 2.16: Raw data, surface found by maximum intensity

Surface Location

One of the critical data processing tasks is to determine the surface from the voxel intensities. In Figure 2.17a, the surface of each x-y pixel is determined by fitting a parabola to the locations of the brightest voxels in the z-direction, as described in an earlier section and shown in Figure 2.14.

Other options exist for finding the surface height. For example, Figure 2.17b, shows the same data, but with the surface height determined by the center of the parabola fit to the most intense voxels. The result of this processing step is a single surface height for each pixel in the x-y plane.

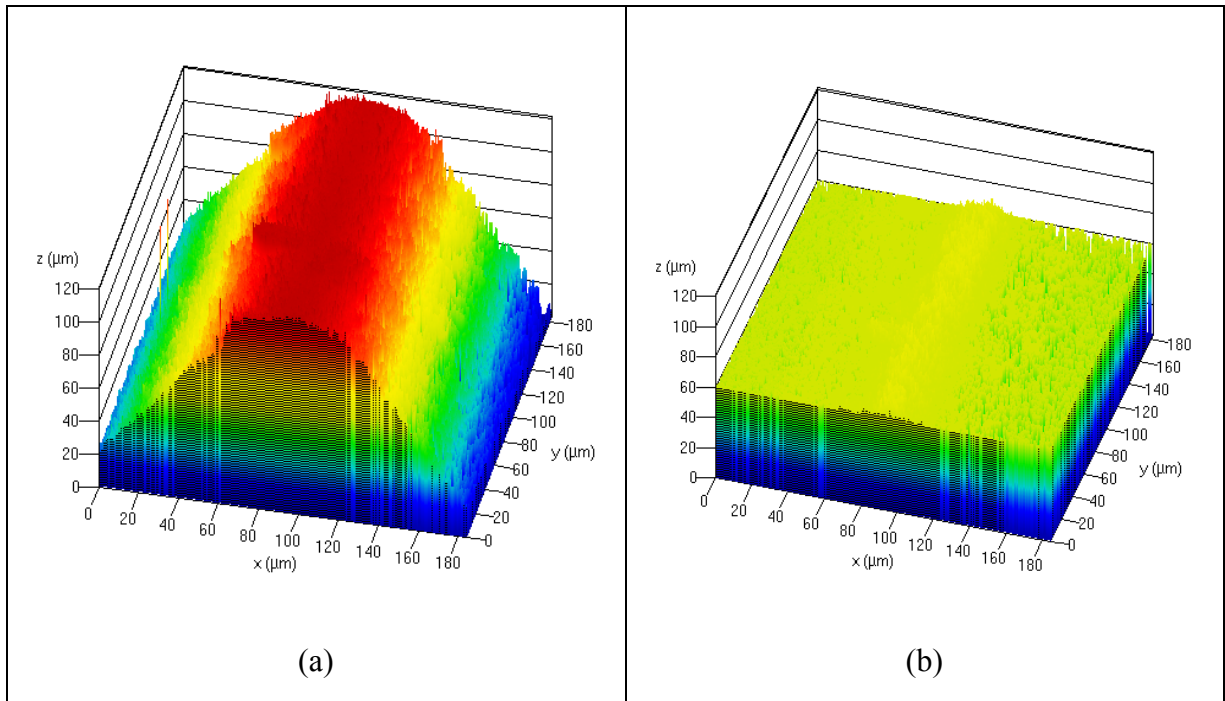


Figure 2.17: Effect of surface location algorithm. Maximum intensity (a) and Center (b)

Setting a Threshold

After the surface is located, there are several steps that can be taken to minimize the noise present in the data set. From the raw data shown in Figure 2.16, it is clear that there is some noise in the system. It is common for the detector to detect low levels of photons even when the surface is not in focus, resulting in background noise. It is possible to remove the background noise by eliminating pixels with a low photon count. This is also known as thresholding. Unfortunately, setting a threshold may remove some valid data points so it is critical to select the threshold value carefully. In most cases, it is simple to choose a threshold value. Figure 2.18(a) shows the data with a threshold value of 28 (out of 256), meaning that all pixels with a maximum intensity below 28 are considered to be noise. Figure 2.18(b) shows the same data set with a threshold value of 29. It is clear that, by changing the threshold value by just one, you have removed a great deal of “background noise.” This transition was evident in virtually all of the data

presented in this work, although the transition number varied slightly. All data presented in this work has had a threshold applied accordingly.

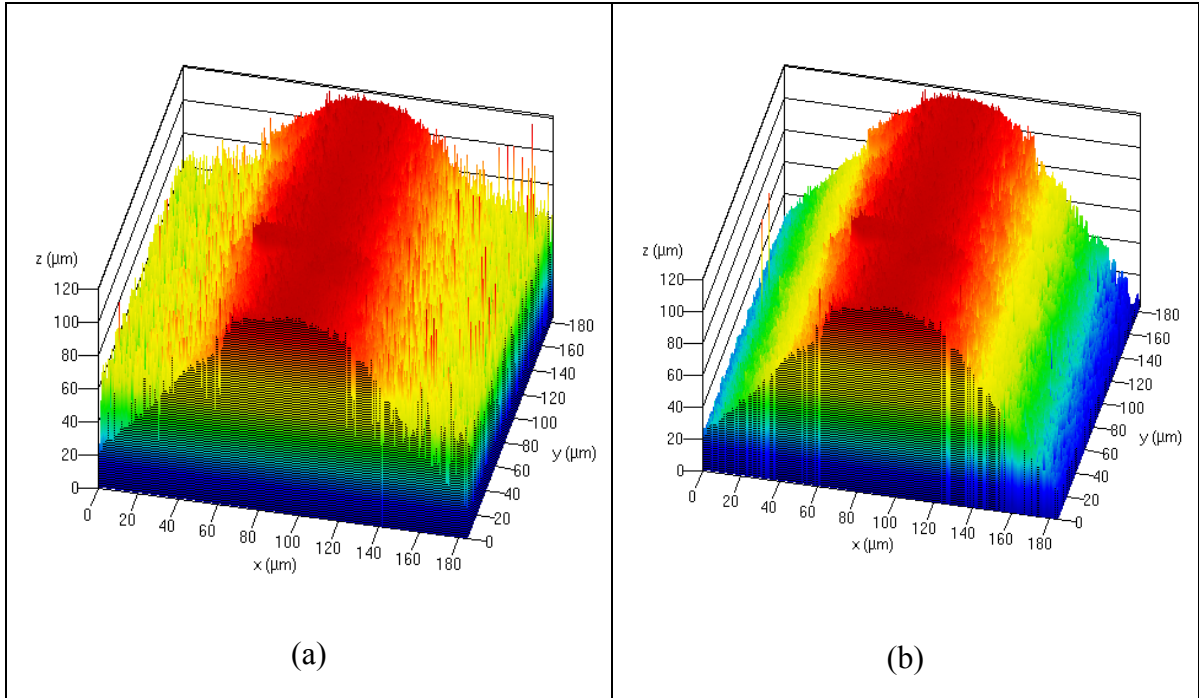


Figure 2.18: The proper threshold value can be selected easily, (a) has a threshold value of 28 and (b) is the same data with a threshold value of 29.

Spatial Filtering

An additional processing step is to choose a spatial filter to remove errant peaks in the data. There are several types of filters available that are frequently used and well understood in image processing. Two of these filters are shown in Figure 2.19. Both filters re-calculate the value for each pixel based on the value of its surrounding pixels. The median filter uses a median value of the pixel being operated on and those surrounding it. The mean, or Gaussian, filter uses the average of these pixels. These data, as well as the majority of the data presented in this work, do contain some pixels that have a zero value. This occurs where the number of photons reflected was not significant enough to distinguish that surface point from background noise, as shown in

Figure 2.18. As can be seen in Figure 2.19(b), the mean filter causes degeneration of the data in the presence of zeros, because the zero values contribute to the average. Fortunately, because the median filter uses a median value, sporadic pixels with zero values do not degenerate the data. This is shown in Figure 2.19(a). The median filter is applied to all data presented.

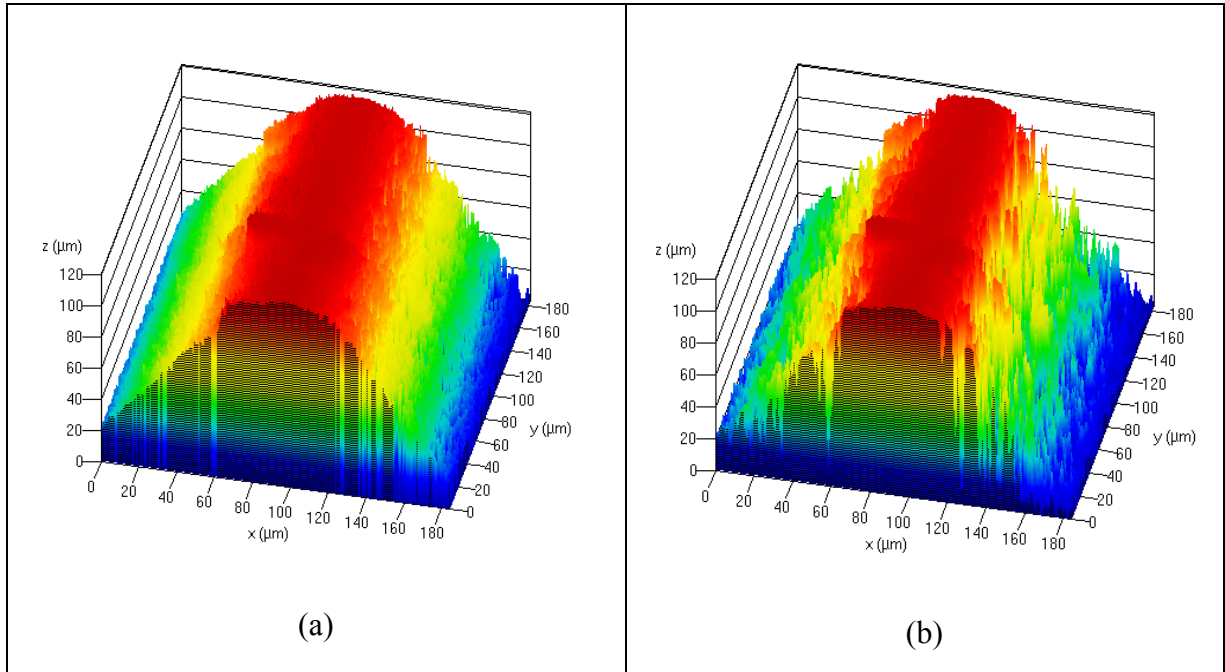


Figure 2.19: Examples of two filtered data sets, (a) uses a median filter, (b) uses a mean filter.

The case studies, presented in Chapter 6, successfully use the CLSM to collect surface data from edges of several mesoscale objects. All data are analyzed using techniques discussed in this section.

REFERENCE ARTIFACTS

Due to the nature of this work, it is important to determine the ability of the CLSM to measure edges of mesoscale structures. In order to correctly measure an edge, the CLSM must be able to measure materials of varying reflectivity at a range of angles.

Unfortunately, the CLSM is not commonly used to measure 3D mesoscale structures. It is most often used to look closely at material properties or to examine the structure of biological specimens, neither of which uses numerical quantification of 3D structures. The calibration scheme for the CLSM reflects these uses. The CLSM used at NIST for material inspection is calibrated using two artifacts, a surface roughness standard with a known periodicity, and a step-height standard. This is not sufficient to show the ability of the CLSM to measure the range of angles present in edges. To demonstrate the ability of the CLSM to measure mesoscale edges, a well-characterized artifact is needed that incorporates a wide range of angles and can be fabricated in a range of materials.

Weckenmann and Lorz [79] studied the use of calibrated workpieces to monitor coordinate measurement machines in place of the special artifacts (e.g., ball plates, ball bars, and step gages) normally used. They were able to successfully calculate the systematic measurement deviations and uncertainties of the measured features through measurement of the calibrated workpieces.

Although there are many artifacts that are used to characterize measurement devices, both 2D and 3D, there does not exist a 3D NIST-traceable mesoscale standard. However, the artifacts do lend insight into possible artifacts to demonstrate the ability of the CLSM to measure mesoscale edges.

Test Slides

In optical microscopy, the dimensions of the object being measured are often calculated by using a stage micrometer with known rulings [80]. Test slides are an extension of the stage micrometer; offering scales, gratings, circles, and squares with known width and spacing. The height of the test pattern is on the order of 10s of nm.

The test slides are useful for testing resolution, contrast, aberrations, depth of field and flatness in optical microscopy, CLSM, and, if plated, for SEM. Although test slides can be used to verify the resolution and magnification of the CLSM, the small height makes test slides unsuitable as a validation artifact for edge measurement.

Lateral Test Specimen

Another tool used in calibration is a lateral test specimen. A common lateral test specimen is a grid with a known pitch and line thickness. Another example of a lateral test specimen is a checkerboard pattern. The lateral specimens are used to check magnification and assess distortion in several directions. Grids and checkerboard patterns could be used to check the resolution of the CLSM but they do not contain the range of angles needed to serve as a reference artifact for edge measurement.

Tip Characterization

Stylus tip characterization is critical to measurements made using SPM, profilometry and CMM. Tip characterization can be done through dimensional metrology or by use of a well-known artifact.

Vorburger et al. [81] compare stylus profilometer tip profiles collected by three techniques: SEM, optical microscope, and sharp edge trace. For the sharp edge trace, the stylus traversed, at a very slow speed, a razor blade edge with a radius of curvature ($0.1\text{ }\mu\text{m}$) much less than that of the stylus tip ($> 1\text{ }\mu\text{m}$). The data collected from both the SEM and the sharp edge trace are acceptable for determining tip profile while the optical microscope is limited to tip radii greater than $10\text{ }\mu\text{m}$.

Many studies have considered the determination of AFM tip shape. Generally, these studies use either a sharp-edged calibration structure or colloidal gold particles. Hubner et al. [82] use a microstructure with a known width and pitch and extremely steep sidewalls for tip calibration. The edge radius of the calibration structures is neglected. Hubner et al. were able to find the tip shape to 10 nm using this method. Colloidal gold particles are uniform spheres and are used in several studies [83; 84] to characterize AFM tip shape.

Reference Artifact Recommendation

Spheres

Spheres hold promise as validation tools as they are widely available in a range of materials and sizes, are inexpensive, and are well-characterized objects.

Polymer nanospheres and microspheres are available for calibration of SEMs, AFMs, CLSMs, and optical microscopes. These particles have NIST-traceable diameters from 20 nm to 1 mm. McNally et al. [85] use a 10 μm diameter polystyrene bead containing a red fluorescent dye, was used to compare 3D microcopy methods. The bead was sliced into 1 μm thicknesses using a microtome to determine its fluorescent structure (dye penetration). McNally et al. demonstrated the ability of the bead to evaluate the working condition of the confocal microscope by using fluorescent measurement data from the bead to identify aberrations and distortions.

Spheres are also used to calibrate CMM and profile measurement machine measurement styli. These calibrations are performed using a steel sphere with a known

radius and high sphericity. For CMMs, a pair of steel spheres at a fixed distance is used for volumetric calibration.

Using small steel spheres as a validation tool was attempted; however several issues were encountered. The first problem in measuring reflective (as opposed to fluorescent) spheres with a CLSM is that the rapidly changing slope of the surface requires several scans with different detector gains. The top of the sphere requires a relatively small gain to prevent saturation while the highly sloped sides require a large gain in order to distinguish the surface from background noise. Unfortunately, there is no automated process for merging scans with inconsistent gain levels because it is not currently possible accurately locate data points at the intersection between scans of different gains.

Figure 2.20 is a view of the first three scans collected from the top of the sphere. The diameter of the sphere is 653 μm . Figure 2.20(a) shows the first scan, Figure 2.20(b) shows the second, and Figure 2.20(c) the third.

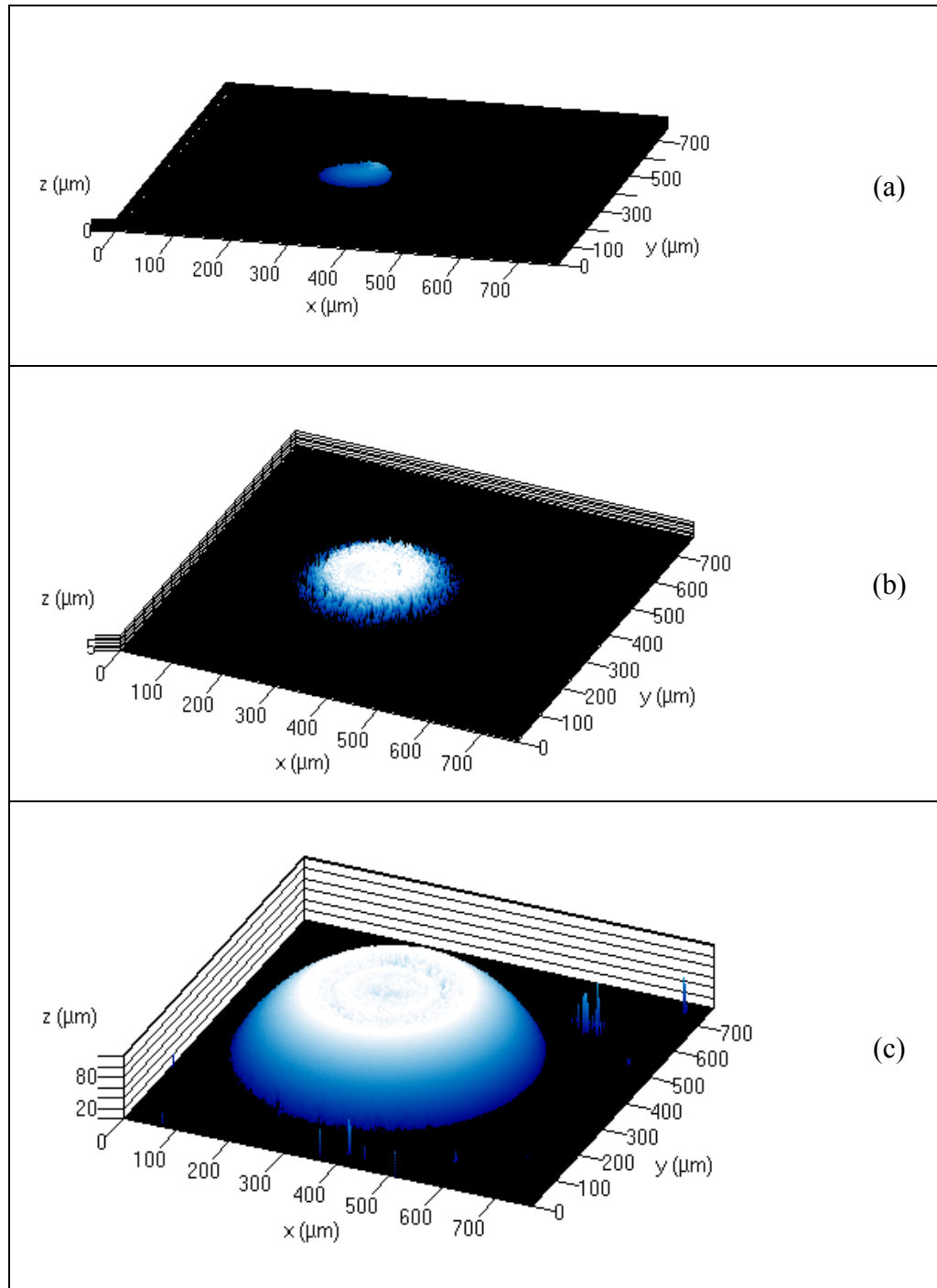


Figure 2.20: Top three scans of 635 μm sphere

The scans were taken without any overlapping regions (e.g., the z-height of the bottom of the first scan is the same as the z-height of the top of the second scan). It can be seen that there is significant reflection from surfaces outside of the scanned range,

especially in Figure 2.20(c), where the top of the scan includes data from the center of the sphere, which should exist only on the top surface. This reflection problem is due to the significant increase in detector gain that is necessary to collect data from the sides of the sphere. Similar problems were observed in spheres with diameters of 381 and 1000 μm .

Due to the problems present in merging data from scans with varying detector gains, the CLSM is not able to properly measure a sphere and thus it is not a suitable object for CLSM validation. Another validation tool is needed.

Sine Bar Concept

A reference artifact that has the ability to represent a range of angles is the combination of a sine bar and a set of gage blocks. A sine bar is a very flat metal bar that rests two balls, as shown in Figure 2.21. Acko [86] created a sine bar able to generate angles with an uncertainty of 1 $\mu\text{m}/\text{m}$ for the calibration of electronic levels.

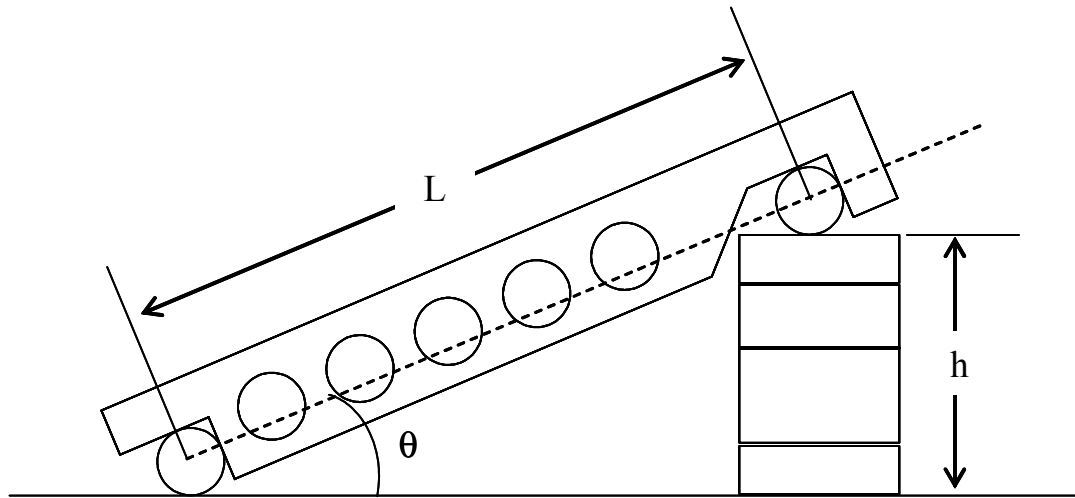


Figure 2.21: Sine bar

The angle can be varied by adjusting total height of the stack of gage blocks. The change in height (h) creates a change in angles (θ), as calculated by Equation (2.4).

Small errors in the combined height of the standards as well as slight form deviations in the sine bar create uncertainty in the angle of the sine bar. Small errors in calculated height have a much larger effect on accuracy when the sine bar is at a high angle. Therefore, it is not recommended to put the sine bar at an angle greater than 45°.

$$\theta = \sin^{-1}\left(\frac{h}{L}\right) \quad (2.4)$$

Future Reference Artifacts

If the difficulty of manufacturing a reference artifact is not considered, there are several reference artifact shapes which would be useful in understanding the ability of a measurement tool to measure edges. Two common edge shapes, which are expected based on knowledge of mesoscale manufacturing processes and previous studies, are a radius and a chamfer.

To understand the ability to measure a chamfered edge, two artifacts are recommended. A single artifact which contains areas at various angles, from 0° to 90° demonstrates the ability of the measurement tool to measure a variety of angles. Second, an artifact that contains two planar surfaces which intersect at a range of angles demonstrates the ability of the measurement tool to measure chamfered edges.

For round edges, two additional reference artifacts are suggested. An artifact that contains a variety of curved surfaces with a range of degrees of a circle demonstrates the ability to measure a curved surface. An artifact that contains the intersections of curved surfaces of varying degrees of arc with planar surfaces demonstrates the ability to measure a curved edge.

SUMMARY

Many measurement tools are available for measurement of mesoscale structures. Although most of the tools are unable to measure a mesoscale edge, three tools are been identified for edge measurement; the AFM, the profilometer, and the CLSM. The Zeiss LSM510 CLSM is used to collect data, machine specifications and analysis methods are presented. A reference artifact is desired to demonstrate the ability of the CLSM to measure an edge. Until a three dimensional mesoscale standard is developed, a sine bar can be used to create a range of angles to test CLSM abilities.

CHAPTER 3: EDGE CHARACTERIZATION

For this work, it is of interest to understand both the size and the geometry of the edge. Methods, used to describe shape and size, find their foundations in both deburring research and traditional coordinate metrology. In deburring, the height, width, and point of highest deviation are all of importance, and serve as the basis of the edge characterization strategy. Coordinate metrology offers methods of describing expected edge shapes (line, circle, and parabola) which allow for easy extraction of the desired quantities. Start and end point of the edge is another concern, this is determined by consideration of the surface conditions of both the top and sidewalls.

The characterization methodology can be considered as a group of algorithms that provide an intuitive representation of different edge qualities. These algorithms must operate both on a small section, or slice, of the edge as well as on the edge in entirety. Size and shape are determined for each independent slice. Trends in the shape and size are tracked by considering edge parameters over the entire edge. Abrupt changes, such as those caused by burrs (or protrusions) and dents, are visible in the trend tracking.

EDGE CHARACTERIZATION ASSUMPTIONS

From previous studies as well as knowledge of processing conditions, the edges of most objects typically follow one of the nominal patterns shown in Figure 3.1. Noise and deviation of form from these nominal patterns must be treated appropriately.

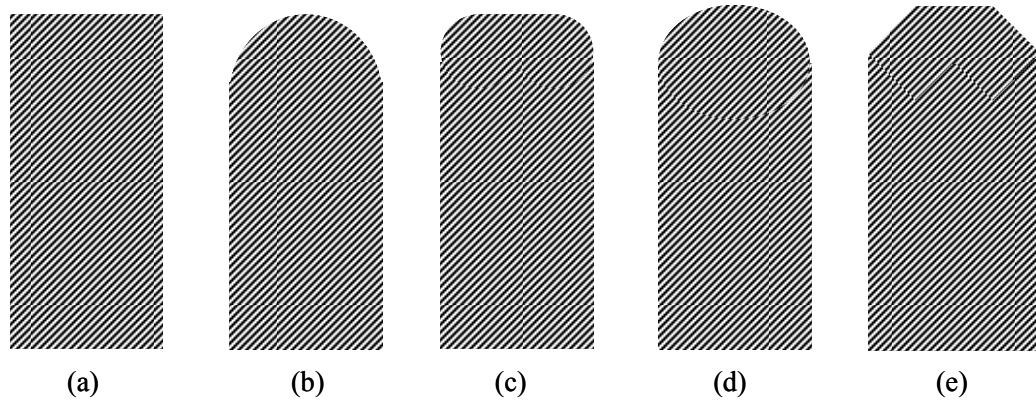


Figure 3.1: Expected edge structures

Before the edge representation method is developed, several assumptions are made about the edge data. First, it is assumed that the top of the object being characterized is flat, and that the sidewalls are straight, except in cases like (b) and (d), where the top is part of the continuous edge. This assumption is used to determine the start and stop points for the edge. Second, tangency between the part and its edge, at the edge end points is not assumed. It can be seen in Figure 3.1, cases (a) (c) and (e), that there exists a discontinuity between the edge and the part. Finally, it is assumed that each continuous edge are considered separately, whether it comprises the entire top of the structure (b,d), or only one side (a,c,e). Although not expected, concave structures such as dents may also exist.

SIZE

Before any processing can be done, the edge data must be separated from the top and the side data. Again, the assumption that the top of the object is planar and that the sidewall is straight is critical because it requires that the side and the top appear as straight lines in two dimensions,

With straight lines representing the top and the side wall, any data that are not part of these straight lines can be considered part of the edge. The edge separation algorithm must address the fact that the top and side are not free of noise.

In order to separate the edge data, lines are fit to the top and side data, starting with the data points at the two extremes. It is assumed that ten percent of the points are from each the top and the side. The edge separation algorithm starts by fitting a line to the first ten percent of the points using a least squares method to minimize the sum of the squares of the normal point to line deviations. The standard deviation of point to line error is calculated.

With the line fit to the first ten percent of the data points, the deviations are calculated for the remaining points. The last point that lies within one standard deviation of the fit line is temporarily considered the final point on the side surface. A line is fit to the temporary side data and the standard deviation is calculated. The last point that lies within one standard deviation of the fit line is the final point on the side surface. The same process is repeated to distinguish between the top and the edge data.

A similar method is been used by Griffith et al. [87] to locate the top and bottom edges of photoresist lines measured by an atomic force microscope. The top and base were fit with straight lines and the threshold used was a two times the standard deviation of the residuals from the fits.

The algorithm is applied to the CLSM data shown in Figure 3.2. The lighter points represent the edge points, the darker points represent the top and side, as found by the algorithm previously described.

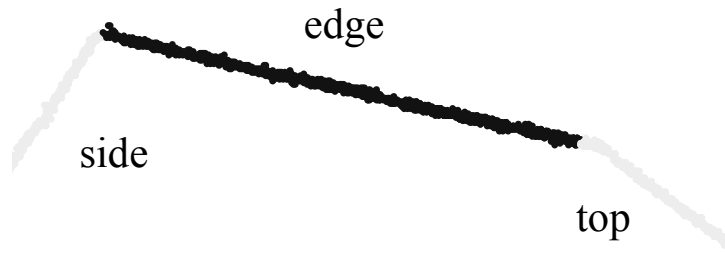


Figure 3.2: Differentiation between edge, top, and side

This edge separation algorithm relies heavily on the stated assumption that the top and side are linear in 2D. If the assumption is not valid for the data set, the transition point from top or side to edge may be unclear. As a result, the size of the separated edge may vary based on the condition of the top and side data. This may cause a Type I error. In statistics, a Type I error is a false negative and a Type II error is a false positive. If the size of the

If there is a defect on the edge near the transition from the top or side the transition point may not be clear, resulting in a variation in the size of the separated edge.

SHAPE

In order to represent the shape of the edge, it is desirable to fit a curve to the data in order use the curve(s) parameters to describe the edge. Ellipses have the potential to representing the expected shapes. However, it is shown that the ellipse is an unsuitable shape for edge fitting, due to the many local minima present.

Ellipse Representation

One method of representation is to find the best-fit ellipse for each curve segment. This easily represents the circular and elliptical edge types, and can also be forced to

represent the chamfered edges: a small segment of a relatively large ellipse mimics a straight line. The curve segments are comparable using standard ellipse parameters.

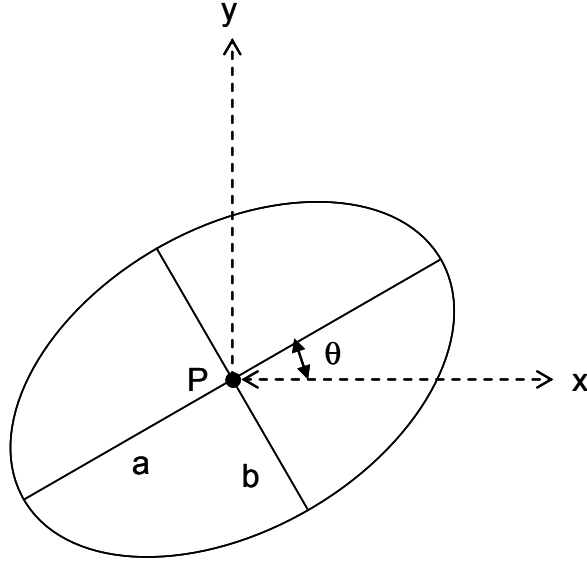


Figure 3.3: Rotated ellipse parameters

The standard parameters can be found in the equation of an ellipse centered at (0,0) with no rotation about its center. This is given as Equation (3.1), where x and y are the x and y -coordinates of points on the ellipse, a is the major axis, and b is the minor axis. Three additional parameters are added with the rotation (θ) and the center point (P) as shown in Figure 3.3, giving the ellipse 5 variables (a, b, P_x, P_y, θ).

$$\frac{x^2}{a^2} + \frac{y^2}{b^2} = 1 \quad (3.1)$$

This method of representation has some significant drawbacks. First, because ellipses do not have a constant curvature, a relatively highly curved section of a large ellipse, or a relatively straight section of a small ellipse can represent similar edge segments. The starting and stopping angles for the edge can be used, but adds two more variables to the 5 variables which are already defined. Due to the extreme number of

variables, using standard ellipse parameters could make the comparison of two similarly shaped segments very difficult.

Fortunately, there is another way to represent ellipses. Quadratic rational Bezier curves have the ability to exactly represent conic sections [88]. The quadratic rational Bezier curve is defined by three data points (P_0, P_1, P_2), and their corresponding weights (w_0, w_1, w_2). The first and last data points lie on the curve, and the vectors from the endpoints (P_0, P_2) to the center point (P_1) define the tangents at the endpoints. The standard form for a quadratic rational Bezier curve is given in Equation (3.2), where u ranges from 0 to 1 and $P(u)$ defines the point along the curve at u .

$$P(u) = \frac{(1-u)^2 w_0 P_0 + u(1-u) w_1 P_1 + u^2 w_2 P_2}{(1-u)^2 w_0 + u(1-u) w_1 + u^2 w_2} \quad (3.2)$$

Although it seems there are still a considerable number of variables to be compared, these can be narrowed down significantly. First, the endpoints (P_0, P_2) are assumed to be known from the data set. Also, there exists a conic shape factor, ρ , given in Equation (3.3).

$$\rho = \frac{w_1^2}{w_0 w_2} \quad (3.3)$$

$$P(u) = \frac{(1-u)^2 P_0 + u(1-u) w_1 P_1 + u^2 P_2}{(1-u)^2 + u(1-u) w_1 + u^2} \quad (3.4)$$

Thus, with the end points known, there exist only three variables, $P_{1,x}, P_{1,y}$, and w_1 as shown in Equation (3.4). If $w_1 \geq 1$ or $w_1 \leq -1$, the resulting conic section is non-elliptical. If $-1 < w_1 < 0$, the resulting conic section is the complement to the ellipse

generated by the same center point and the absolute value of w_1 . Therefore, for an ellipse, $0 < w_1 < 1$, must hold true.

It is possible to define a range of parameter values that meet the criteria for each of the three shapes of interest, the straight line, the ellipse, and the circle. A circle is a special case of an ellipse and its parameter ranges are fairly restrictive. The straight line also has a restrictive set of possible parameters. The ellipse comprises the remainder of the parameters that meet the conic shape factor restriction.

In order to define an arc of a circle using a quadratic rational Bezier curve, the control triangle (formed by the three control points) must be isosceles. The weight of the center control point, w_1 , must be equal to the cosine of the angle between the line joining the endpoints and one of the legs [89], as illustrated in Figure 3.4. If the edge segment is known to be circular in shape, only the angle, θ , need be varied.

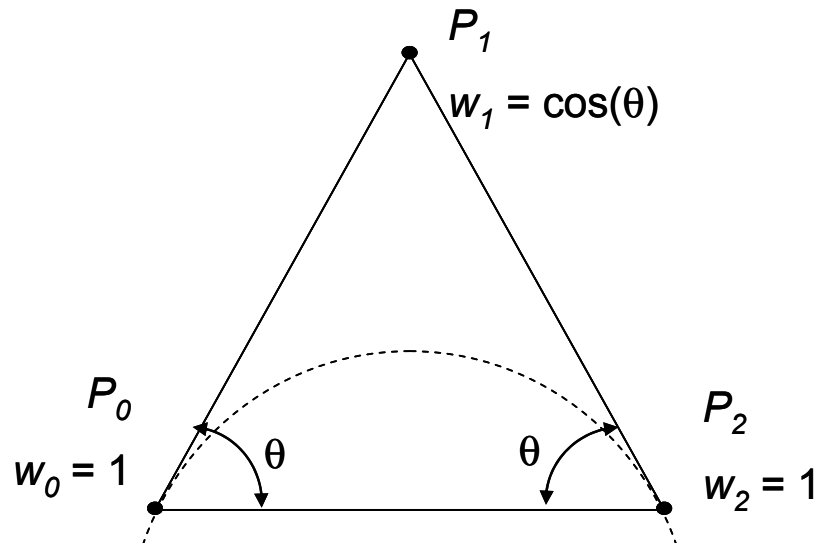


Figure 3.4: Requirements for quadratic rational Bezier circle

Although not exactly a conic section, a quadratic rational Bezier curve with collinear control points represents a straight line. The weight of the center point does not

affect the shape of the curve, nor does the placement distance of the center point along the line from the first to the last control point.

Using a fitting algorithm that varies only the center control point (P_I) and its associated weight (w_I) allows for the fitting of the circle, straight line, and ellipse. The only constraint which needs to be imposed is to limit the values of w_I to the range (0 1), not inclusive. The best fit for these three variables is found using a standard least squares minimization routine that minimizes Equation (3.5), where $(D_{i,x}, D_{i,y})$ is the coordinate of the edge data point and $(P_x(u), P_y(u))$ is its closest point on the Bezier curve.

$$obj = \sqrt{(D_{i,x} - P_x(u))^2 + (D_{i,y} - P_y(u))^2} \quad (3.5)$$

If the shape is previously known to be a circle, the fit can be limited to the angle, θ , as this variable, along with the endpoints allows for a complete description of the quadratic rational Bezier curve. If desired, it is possible to directly calculate the standard conic properties from the quadratic rational Bezier representation [90].

Trials of this method were run using simulated data with known circular, elliptical, and straight edge shapes. It was found that there exist a great number of local minima, causing the fitting algorithm to return the parameters for an incorrect shape. Because this method does not return correct parameters, a different shape characterization method is used.

Due to the problems present in using a single shape to describe all edge conditions, several shapes are used. A line is used to represent a chamfered edge, a circle to represent an edge with a radius, and a parabola to represent all other edges including those with burrs or protrusions. As with the ellipse, the shapes are fit using a least-

squares minimization technique. It is necessary to outline a method for choosing the appropriate shape from the three possibilities.

Line

To represent an edge with a chamfer, a line is the obvious chose. The best fit line parameters, P_1 and P_2 , are found by minimizing the sum of the squares of the deviations.

The deviations are calculated by finding the normal distance $|\overline{PP_3}|$ between each data point, P_3 , and the line $\overline{P_1P_2}$. These quantities are shown in Figure 3.5.

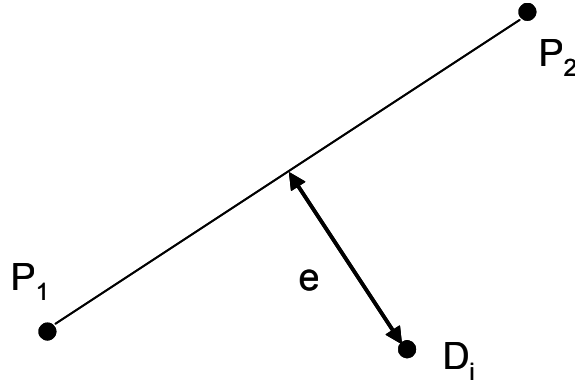


Figure 3.5: Quantities for line fitting

The calculation for normal distance (e) between D_i and the straight line is given below [91].

$$\begin{aligned}
 P &= P_1 + u(P_2 - P_1) \\
 (D_i - P) \cdot (P_2 - P_1) &= 0 \\
 (D_i - P_1 + u(P_2 - P_1)) \cdot (P_2 - P_1) &= 0 \\
 u &= \frac{(D_{i,x} - P_{1,x})(P_{2,x} - P_{1,x}) + (D_{i,y} - P_{1,y})(P_{2,y} - P_{1,y})}{\|P_2 - P_1\|^2} \\
 e &= \|D_i - P\|
 \end{aligned} \tag{3.6}$$

Circle

For parts with a radius, or circular edge, fitting a circle is the clear choice. The circle can also represent a convex edge. There are two circle parameters, the center point (P) and the radius (r), as shown in Figure 3.6.

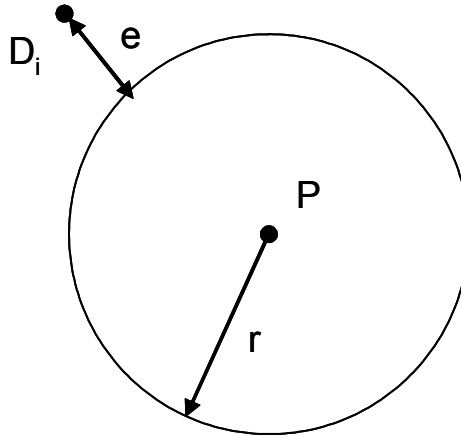


Figure 3.6: Circle parameters

The circle is fit by minimizing the sum of the squares of the point to circle deviations (e). This deviation is calculated in Equation (3.7).

$$e = \sqrt{(D_{i,x} - P_x)^2 + (D_{i,y} - P_y)^2} - r \quad (3.7)$$

When a circle has a radius, the edge contains only a portion of the circle. As a best case, if the edge is a perfect radius, and the sidewall and top are at 90° angles, the edge will be one quarter of a complete circle. It is expected that, for some cases, an even smaller portion of the circle will be present. Without data spanning an entire circle, understanding the performance of the circle fitting routine with respect to the angle of arc present in circle is important. Figure 3.7 shows the relationship between the error present in the center and radius and the amount of arc present for different noise levels. Produced surfaces generally contain deviations which can be represented as Gaussian, or

normally distributed, noise. The noise level indicates the standard deviation of the Gaussian noise added normal to the circle as a fraction of the radius. The error is the sum of the displacement of the center point from the expected center point and the difference between the best-fit and expected radii.

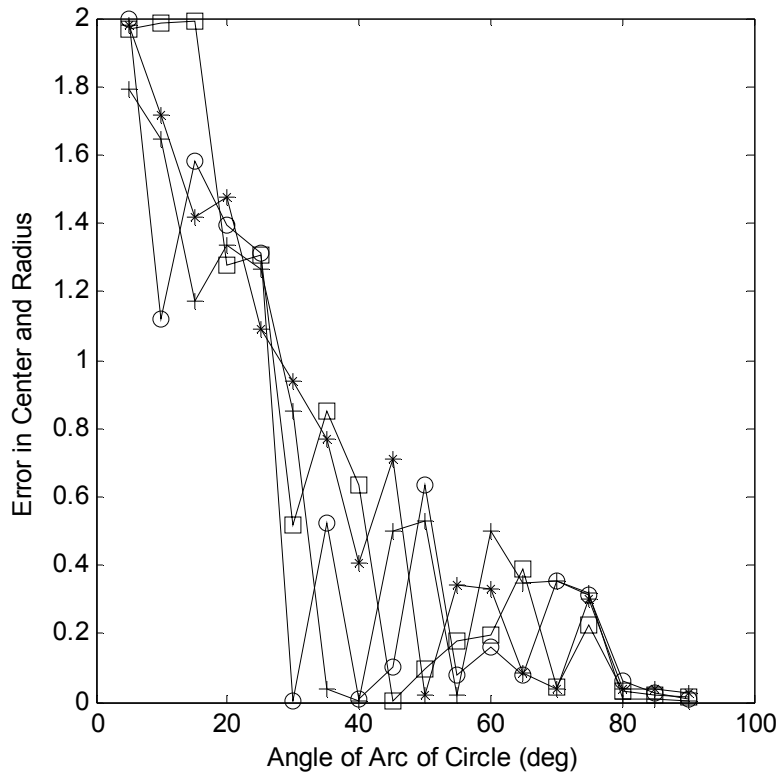


Figure 3.7: Error in center and radius vs. angle of arc of circle for several noise levels

It can be seen that the amount of the circle present does impact the error level in the best-fit for all noise levels. Chernov and Lesort [92] also observe the instability of the fitting method for data sampled along a small arc of 20° or less. It appears that below 30° , the circle fit experiences especially high error levels. Thus, this routine is best suited to circular data containing more than 30° of arc.

Parabola

The line and circle are obvious choices for edge representation. However, these two shapes are not able to accurately represent all expected edge shapes and expected conditions such as burrs and dents, as shown in Figure 3.8.

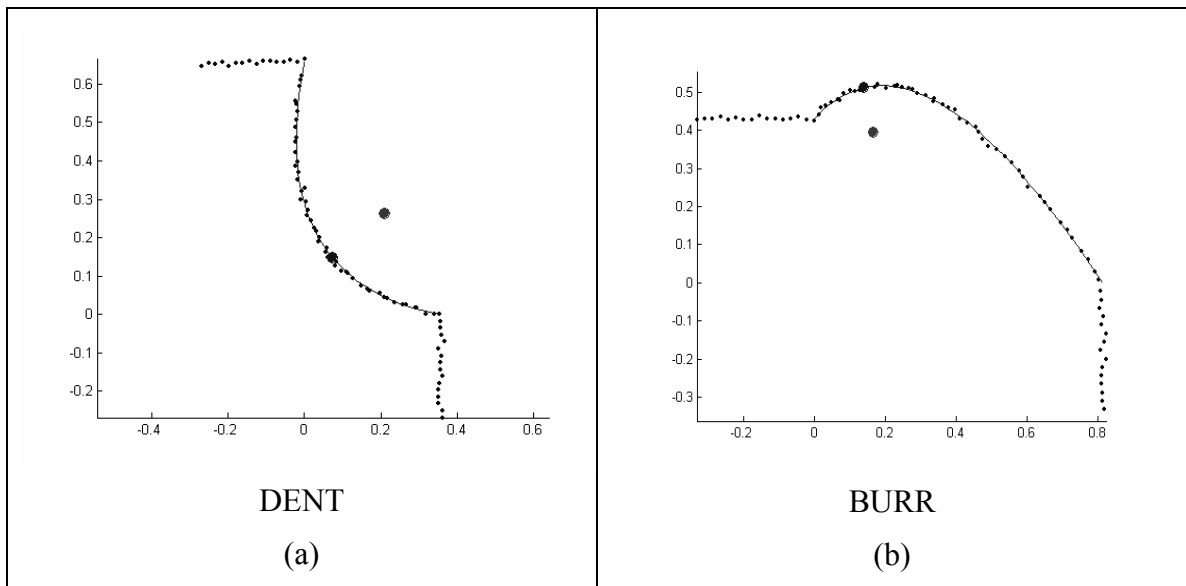


Figure 3.8: Edge conditions represented by parabolas

Polynomial Representation

For shapes and conditions similar to those in Figure 3.8a-b, a parabola can be used to describe the shape. Parabolas have several qualities that make them particularly suitable for this application; the equations are straightforward and like the circle and line, and the fitting parameters are intuitive.

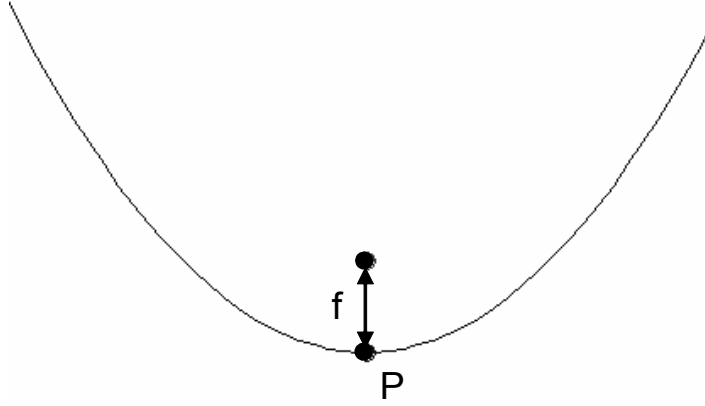


Figure 3.9: Parabola parameters

Two equations are available for axis-aligned parabolas. Parabolas aligned with the y-axis, as shown in Figure 3.9, can be described with a quadratic Equation (3.8) or with a parameter-based Equation (3.9).

$$y = ax^2 + bx + c \quad (3.8)$$

$$(x - P_x)^2 = 4f(y - P_y) \quad (3.9)$$

Unfortunately, these equations describe only axis aligned parabolas. To describe edges, it is critical that the parabola have an additional parameter for rotation. To fit a rotated parabola, the data D can be transformed by rotation, Equation (3.10). The residual can be calculated by using a standard polynomial fit of a y-axis aligned parabola. The rotation angle θ that results in the smallest residual represents the angle of rotation at which the data most closely represents an axis aligned parabola. This angle can be used to transform the parabola parameters, resulting in a rotated best-fit parabola.

$$D_r = \begin{bmatrix} \cos(\theta) & \sin(\theta) \\ -\sin(\theta) & \cos(\theta) \end{bmatrix} D \quad (3.10)$$

There are two methods that can be used to find the rotation angle. The discrete angle polynomial fit rotates the data by one degree increments, for a total of 180° . The

residuals are calculated for each polynomial fit and the rotation with the smallest residual (the angle at which the data is most closely aligned with the y-axis) is chosen as the best fit. The polynomial coefficients are converted into parabola parameters and rotated by the best-fit angle.

The minimized angle polynomial fit is similar to the discrete angle polynomial fit except that it uses a non-linear least squares minimizer to determine the best rotation angle. A non-linear least squares minimizer requires an initial guess. The initial guess given is the best-fit result from the discrete angle polynomial fit.

Quadratic Bezier Representation

In addition to polynomial based representation, parabolas can also be represented using parameter-based Bezier curves. There is a direct conversion between a quadratic Bezier curve and a rotated parabola, so Bezier parameters can be used for fitting and then converted to parabola parameters. In Equation (3.2), the general form for a rational quadratic Bezier curve is given. The general form for a quadratic Bezier curve is similar, but without weights. This equation is given in (3.11), where P_0 , P_1 , and P_2 are the three control vertices that define the control polygon.

$$P(u) = (1-u)^2 P_0 + 2u(1-u)P_1 + u^2 P_2 \quad (3.11)$$

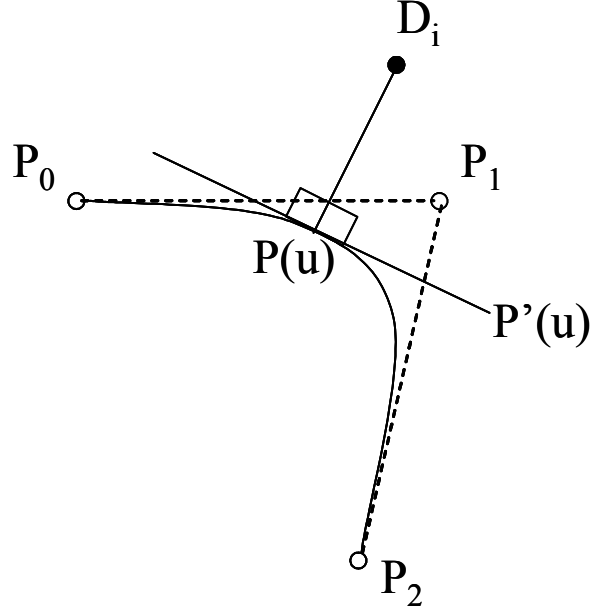


Figure 3.10: Parameters for finding closest point on quadratic Bezier curve

The minimum normal distance from a point to a parabola defined by a Bezier curve can be found analytically because the tangent $P'(u)$ (Equation (3.12)) is perpendicular to the line from the data point D_i to the closest point on the curve $P(u)$ (Equation (3.11)), as shown in Figure 3.10. The mathematical expression for this is given as Equation (3.13).

$$P'(u) = 2[-(1-u)P_0 + (1-2u)P_1 + 2uP_2] \quad (3.12)$$

$$\frac{D_{i,x} - P_x(u)}{D_{i,y} - P_y(u)} = -\left[\frac{P'_y(u)}{P'_x(u)} \right] \quad (3.13)$$

Through algebraic manipulation, it is possible to convert Equation (3.13) into the polynomial expression shown as Equation (3.14).

$$\begin{aligned} 0 &= (a_y^2 + a_x^2)u^3 + (3a_yb_y + 3a_xb_x)u^2 + (2b_y^2 + 2b_x^2 + a_yc_y + a_xc_x)u + (b_yc_y + b_xc_x) \\ a &\equiv P_0 - 2P_1 + P_2 \\ b &\equiv P_1 - P_0 \\ c &\equiv P_0 - D_i \end{aligned} \quad (3.14)$$

Using a root finding method, the equation is solved for u . Up to three roots may exist; in Figure 3.11 the data point D_i exists on the parabola, this point corresponds to the correct solution u_1 , however two additional solutions to Equation (3.14) exist, u_2 and u_3 . To find the correct solution, all real roots are substituted into Equation (3.11) to determine the closest point on the parabola.

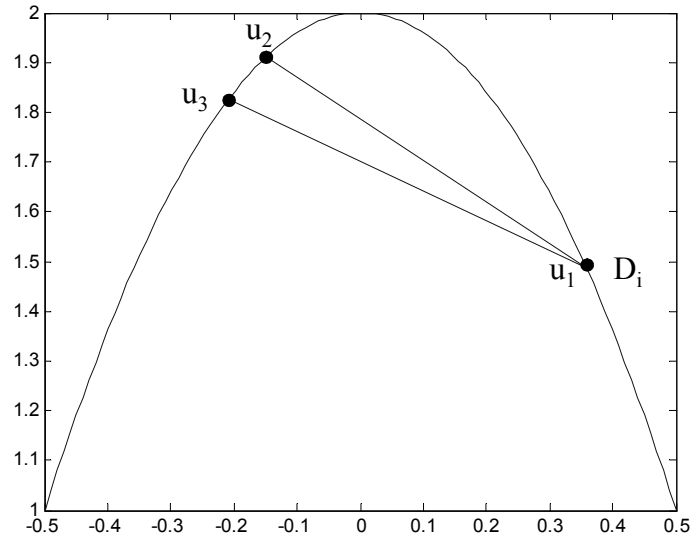


Figure 3.11: Example of multiple solutions for u

Not only do the multiple real roots exist, sometimes the root u may lie outside of the interval $[0, 1]$, implying that it does not exist on curve, as the Bezier curve is finite and defined only on the interval $[0, 1]$. If this occurs and $u < 0$, it is reassigned a value of 0, if $u > 1$, it is reassigned a value of 1. Thus the point to curve deviation is calculated as the distance from the data point D_i to the closer endpoint of the curve.

In order to find the best-fit Bezier curve to the data, the closest point on the parabola is located for each data point. The sum of the squares of the distances from all data points to the parabola is minimized. An initial guess is formulated by taking the

first, middle, and last data points as the three control vertices. The result of the minimization is a set of Bezier control points, (P_0, P_1, P_2) , which define the best-fit parabola.

To extract parabola parameters from the quadratic Bezier form of the equation, Lee [90] has developed the following series of equations, resulting in the focus, F , and the vertex, X . The vertex and the focus are sufficient to completely describe a rotated parabola

$$\begin{aligned}
U &= P_0 - P_1 \\
V &= P_2 - P_1 \\
\alpha &= |U|^2 \\
\beta &= U \cdot V \\
\gamma &= |V|^2 \\
\zeta &= \alpha + \gamma + 2\beta = |U + V|^2 \\
F &= P_1 + \frac{\gamma U + \alpha V}{\zeta}
\end{aligned} \tag{3.15}$$

$$X = P_1 + \left(\frac{\gamma + \beta}{\zeta} \right)^2 U + \left(\frac{\alpha + \beta}{\zeta} \right)^2 V \tag{3.16}$$

Fitting Method Results

In order to compare the three parabola fitting methods, tests are run using a discrete angle polynomial fit, a minimized angle polynomial fit, and a Bezier fit. Several variables, noise, amount of included parabola, and rotation angle, dictate the shape of the final curve. It is of interest to determine the performance of the fitting methods with respect to these variables.

A metric is required for comparison of the performance of the fitting methods. One potential method is to compare the residual errors from the best-fit conditions.

These residuals are easily available as they are calculated as part of the fitting routine. The residual error is compared for generated data containing different noise levels, amount of included parabola, and rotation angles.

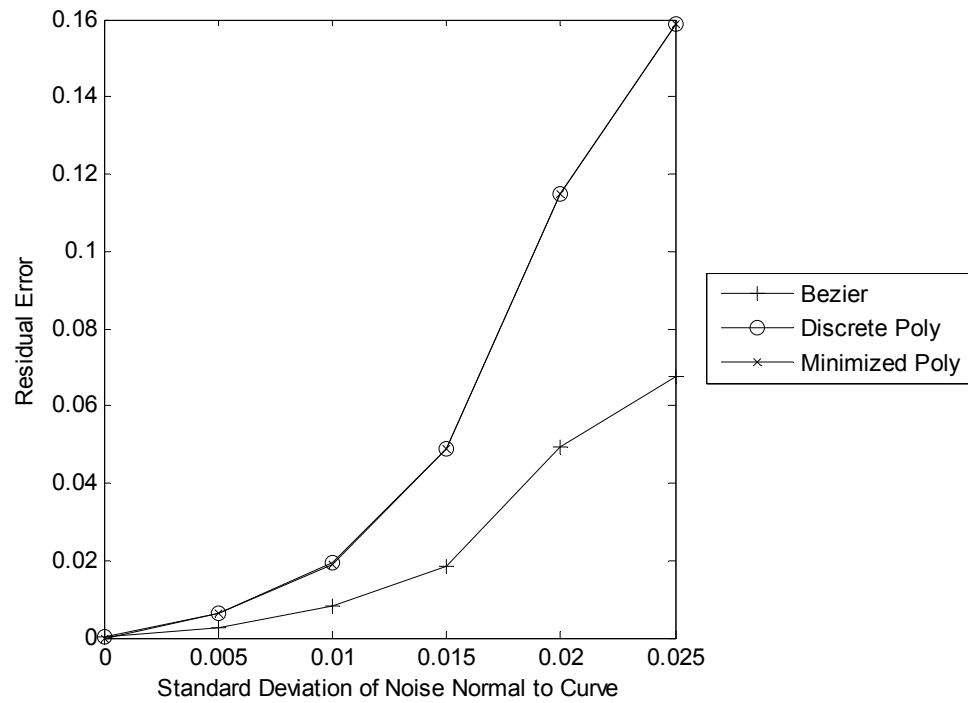


Figure 3.12: Residual errors vs. noise level for parabola fitting

Gaussian noise is added in the normal direction to the parabola. In this case, the parabola is almost axis-aligned to the y-axis with an included angle of approximately 90° . The included angle indicates that the tangent lines drawn at the ends of the parabola are approximately perpendicular. The noise level is the standard deviation of the added Gaussian noise, and varies from 0 to 0.025.

As expected, Figure 3.12 shows that in all cases the residual errors increase as the noise level increases. The two polynomial fitting methods have residuals errors are similar but higher than the Bezier method. It is expected that the errors are similar

because the fitting methods are similar. The lower level of noise for the Bezier method can possibly be explained by the method used to calculate the residuals. Where the Bezier method finds the error normal to the curve, the polynomial method assumes that the x-value is known, and the error lies in the y-value. Thus, the residuals are not calculated normal to the curve, leading to larger residual values. This is most evident with larger noise levels.

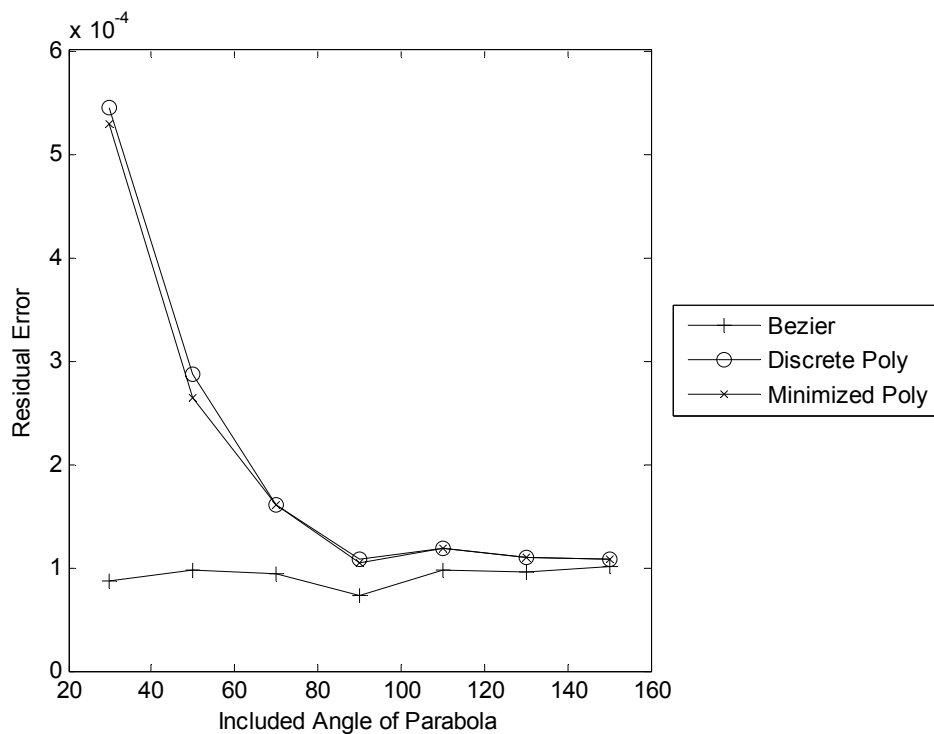


Figure 3.13: Residual errors vs. height of parabola for parabola fitting

The second test varies the included angle of the parabola from 30° to 150° with a noise level of 0.001 and a rotation angle of 45° . As previously stated, the included angle is the angle between the tangent lines at the ends of the parabola. Larger included angles indicate flatter parabolas. All fitting methods performed acceptably by this metric, as the residual errors in Figure 3.13 are acceptably small.

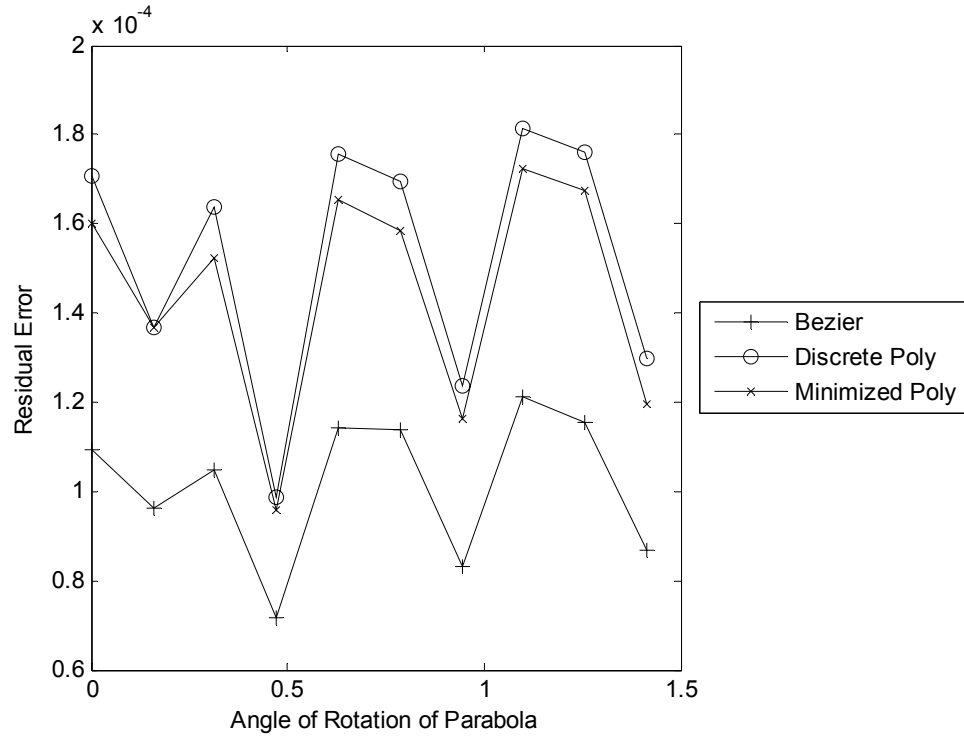


Figure 3.14: Residual errors vs. angle of rotation for parabola fitting

The final variable tested is the angle of rotation from an axis-aligned parabola. The angle of rotation is varied from 0° to 90° . The parabola has a noise level of 0.001 and an included angle of 90° . As shown in Figure 3.14, the residual error levels are sufficiently small. Again, it is observed that the Bezier fitting method results in the lowest residuals, most likely due to the method used for residual calculation. The discrete polynomial fit has the highest residuals. This is also expected as the minimized polynomial is not restricted to finding the best fit among a specified set of angles.

Using the residuals to compare the fitting methods indicates that while all fitting methods are acceptable, the Bezier method tends to achieve the smallest residuals. Because this could be due to the method of calculating the residuals, it is of interest to check the results with a second metric. Since the focus and vertex of the parabola are of interest, it is reasonable to develop a metric using these parameters to compare the

parabola fitting methods. Because the comparison of these methods is done using computer-generated data, the nominal focus and vertex used to create the data is known. The focus and vertex are of equal importance, so the deviations of the fit focus and of the fit vertex from those used for data generation are added and the result used as a second metric for comparison. However, this metric also has limitations. For noisy data the focus and vertex used to generate the data may not be the best fit. The focus and vertex errors presented below are for the same data previously presented in this section.

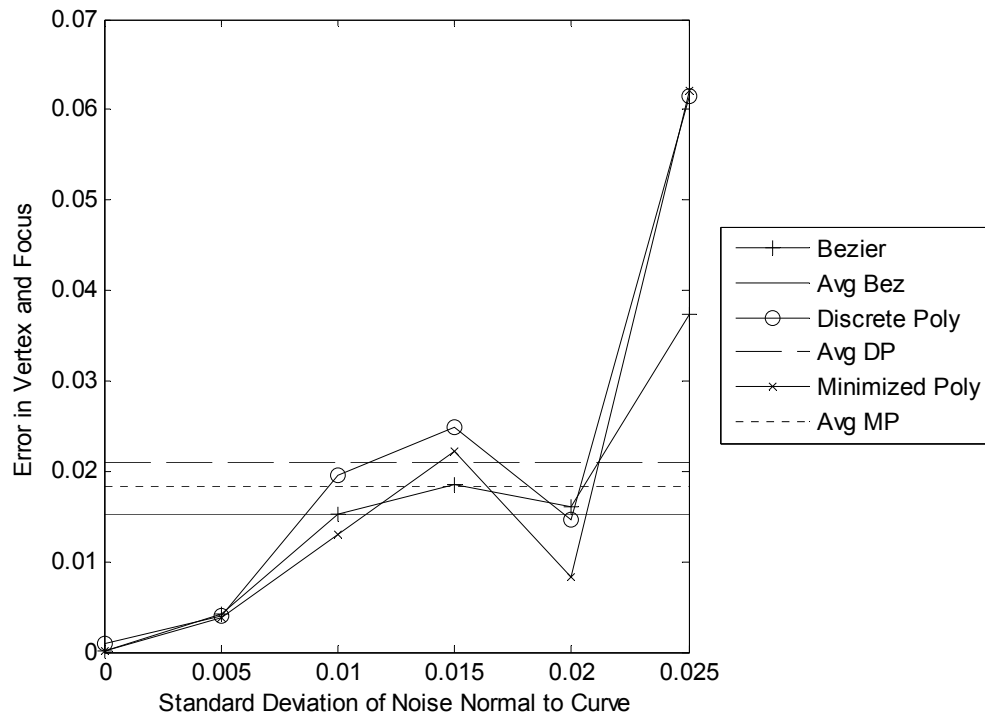


Figure 3.15: Vertex and focus error vs. noise level for parabola fitting

Figure 3.15 shows the vertex and focus error for various noise levels. Also included, in order to aid comparison are average lines, Avg Bez, Avg DP, and Avg MP, representing the average value for the three fitting methods, Bezier, Discrete Poly and Minimized Poly, respectively. Unlike with residual error comparison, the Bezier fitting

method is not the best performer for every data set. The code used for this test was run several times. It is observed that no fitting method can be considered clearly better than the others.

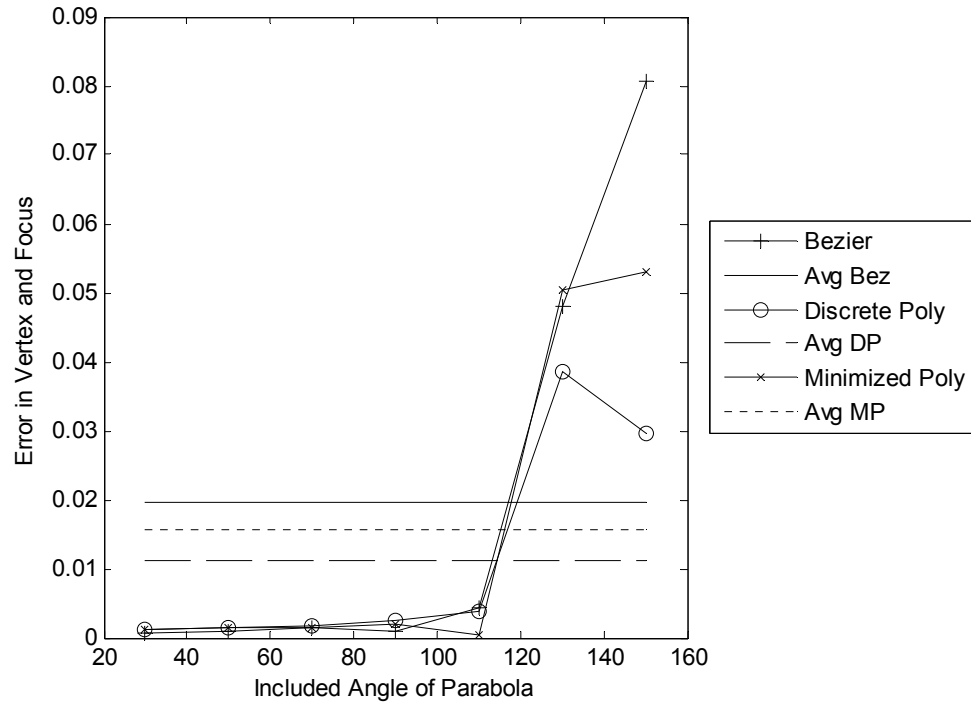


Figure 3.16: Vertex and focus error vs. included angle of parabola for parabola fitting

Figure 3.16 shows the results from variation in included angle. In this case, like the residual comparison, all methods perform very well for sharper parabolas, while they result in more error for flatter parabolas. Interestingly, the discrete polynomial method outperforms the other two in these tests. Although this is unexpected, it can be explained by considering the great influence of noise on the flatter parabolas. Similar to fitting a circle, when the data defines a small percentage of the parabola, the fitting methods tend to be less stable. With the exception of the large included angles, all fitting methods seem to provide acceptable results.

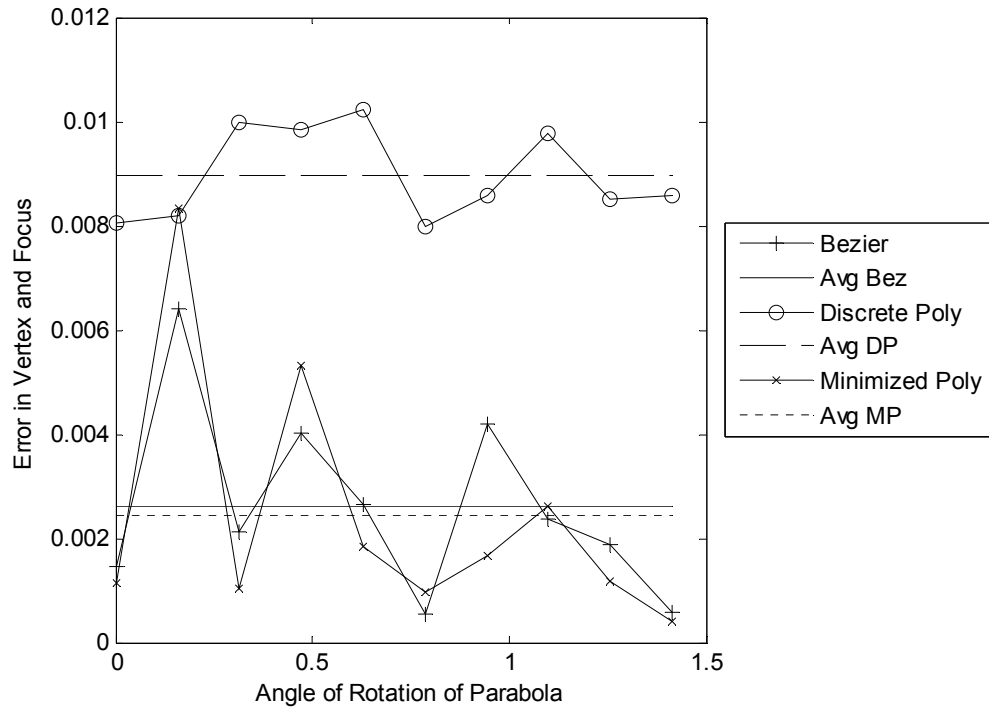


Figure 3.17: Vertex and focus error vs. angle of rotation for parabola fitting

Again, Figure 3.17 shows that all fitting methods provide acceptable results for various angle of rotation. In this case, the results are as expected, with higher errors for the discrete polynomial fit, and smaller errors for the minimized polynomial and the Bezier fitting methods.

Overall, these results show that the minimized polynomial and Bezier methods tend to outperform the discrete polynomial fitting method. Either of these is acceptable for use, but the Bezier fitting method is chosen because the residuals are calculated normal to the curve. This is important because the parabola fitting residuals are compared to the circle and line fitting residuals to determine the appropriate shape. Because the circle and line fitting methods calculate the errors normal to the curve, it is desirable that the parabola fitting method make the same calculation.

Determining appropriate shape

If the nominal shape of the edge is unknown, it is necessary to provide a method for determining the appropriate shape for a given edge. Fortunately, each fitting method relies on minimization of the sum of the squares of the normal distances from each point to the curve. Thus, the appropriate shape can be defined as the shape that results in the smallest residuals, determined by fitting all three shapes to each edge.

Care must be taken, however, to choose a circle or line when appropriate as the parabola can mimic both shapes. Figure 3.18 provides an example of a parabola mimicking a straight line. This condition is avoided by checking to be sure that the best-fit vertex of the parabola lies within the edge.

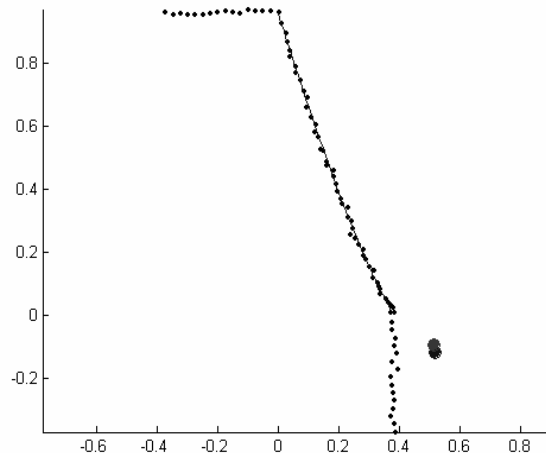


Figure 3.18: Parabola mimicking a line

ABRUPT CHANGES

Up to this point, the edge has been considered only as a series of 2D slices. The data presented in this study are a series of CLSM measurement areas taken around the perimeter of an object. Each measurement is broken into a series of 2D slices to be

analyzed as presented above. In addition to analysis of individual slices, local changes can be analyzed within a measurement area. Any abrupt deviation from a consistent edge should be analyzed and treated with care.

Abrupt changes are sudden local changes in the edge that mark the location of an inconsistency, such as a dent or burr. There are two types of inconsistencies, those that affect only a small portion of the edge, and those that affect the entire edge. Those that affect the entire edge are visible by tracking the trends. Tracking the residuals of the fit within a measurement area provides a simple and effective method for detecting the presence of a small inconsistency.

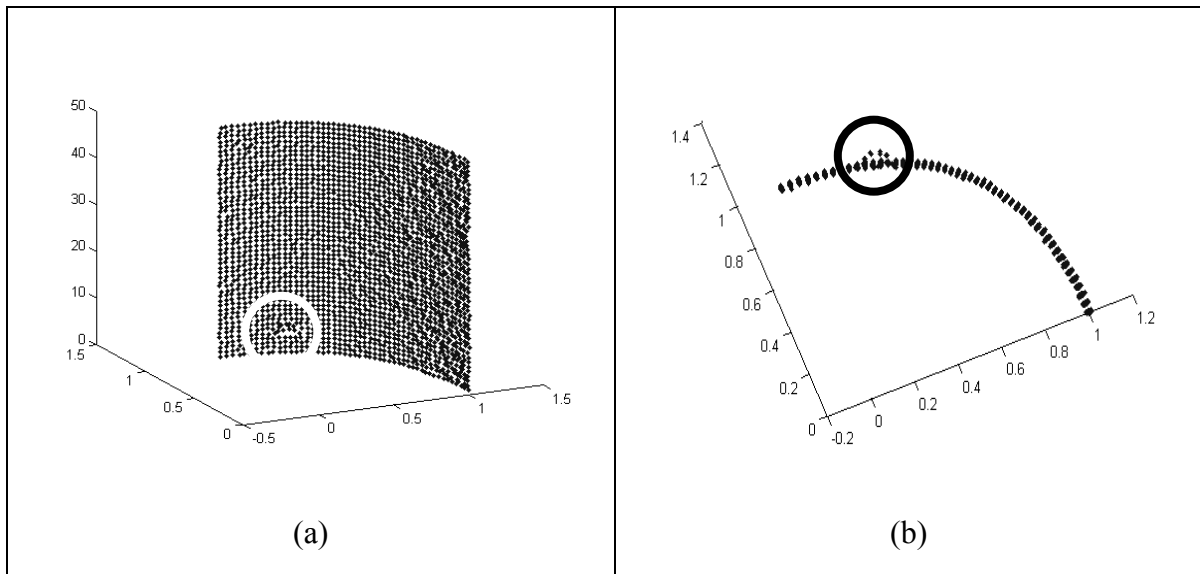


Figure 3.19: Generated data with a single burr

To demonstrate the proposed algorithm, data were generated using a Bezier curve defined by three control vertices located at $P_0 = [0 \ 1]$, $P_1 = [1 \ 1]$, and $P_2 = [1 \ 0]$. The standard deviation of the noise, applied normal to the curve is 0.005. One small burr is added to the curve, as seen in Figure 3.19. The burr exists on slices four through seven.

The residual errors are calculated by a Bezier parabola fit for each of the fifty slices present in the generated data. These errors are plotted vs. the slice number in Figure 3.20. The burr creates a visible elevation of error level in slices four through seven. It is important to analyze these abrupt changes within a measurement area, as noise levels and thus deviations from other measurement areas may vary widely, suppressing changes that are evident in areas with lower noise levels.

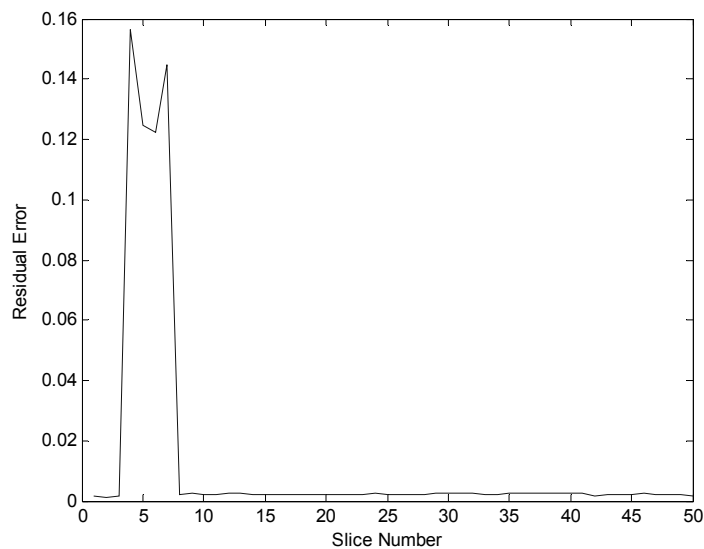


Figure 3.20: Residual error from generated data with a single burr

Additional tests have been run with a single dent, several burrs, several dents, and combinations of burrs and dents. In all cases, the slices containing burrs and dents were identifiable by comparing the relative residual errors for each of the slices. Studies using this methodology are presented in Chapter 5.

TRENDS

In addition to considering slices within a single measurement area, it is also useful to consider the edge as a whole. It is known that physical properties of parts produced by

some processes, such as stereolithography and LIGA, vary by build location. It is expected that these processes may also create edge conditions that also vary with build location. As a result, trends caused by processing parameters are of interest. The analysis and reporting of trends require consideration of all measured areas of the part edge.

Trends are considered by mapping average fit parameters from each measurement area over the length of the edge. Several parameters exist, including size in the x and y directions and individual shape parameters. In addition to the size parameters, for a line the slope is considered, for a circle the radius is considered, and for a parabola the angle and the focal distance are considered.

Trends are identified by use of statistical process control techniques. Statistical process control is used to identify quality, quality tendencies, and process tendencies. Control charts can be used for analysis of past data to test for control and uniformity or in order to control against standards. Two main types of control charts are available for measurable characteristics, those that consider the range of the measurements (R-chart) and those that consider the standard deviation (S-chart). These charts assume a normal distribution. For processes with large samples (>10) control charts are based on standard deviation. The edge measurements presented in this thesis have 10 or 20 slices which indicate the use of control charts based on standard deviation.

Although the goal is not to determine causes of variation within the process which produces mesoscale edges, a combination of X-bar and S charts are used to consider trends within a single part. The average (\bar{X}) and standard deviation (S) of the measurement area are calculated for each of the parameters of interest (i.e., radius) by

consideration of the parameter value (X_i) for each slice within the measurement. The equations for these quantities are given as Equation (3.17) and Equation (3.18). The number of slices in each measurement gives the sample size (n).

$$\bar{X} = \frac{\sum_{i=1}^n X_i}{n} \quad (3.17)$$

$$S = \sqrt{\frac{\sum_{i=1}^n (X_i - \bar{X})^2}{n-1}} \quad (3.18)$$

To calculate the upper control limit, lower control limit, and control limit, it is necessary to calculate the average standard deviation (\bar{S}) and the average value ($\bar{\bar{X}}$) of the measurement areas. These equations are given as Equation (3.19) and Equation (3.20).

$$\bar{S} = \left[\frac{\sum_{i=1}^m (n_i - 1) S_i^2}{\left(\sum_{i=1}^m n_i \right) - m} \right]^{1/2} \quad (3.19)$$

$$\bar{\bar{X}} = \frac{\sum_{i=1}^m n_i \bar{X}_i}{\sum_{i=1}^m n_i} \quad (3.20)$$

The control limits for a parameter value are given in Equation (3.21). The control limits for the standard deviation are shown as Equation (3.22). The factors shown in the equations assume that the sample size is 20. Because the control limits for the process are unknown, the analyzed values are the same data used to determine the control limits. Additionally, the sample sizes are relatively small. Thus, the produced control charts can

not be used for statistical process control purposes but can be used to locate trends in parameters by part location.

$$\begin{aligned} UCL_S &= 1.490\bar{S} \\ CL_S &= \bar{S} \\ LCL_S &= 0.510\bar{S} \end{aligned} \tag{3.21}$$

$$\begin{aligned} UCL_X &= \bar{\bar{X}} + 0.680\bar{S} \\ CL_X &= \bar{\bar{X}} \\ LCL_X &= \bar{\bar{X}} - 0.680\bar{S} \end{aligned} \tag{3.22}$$

Rules exist for the inspection of these control charts [93]. In statistical process control, points beyond the control limits indicate the presence of an assignable cause under the conditions by which the point arose. Location of a single point within the control limits is attributed to random variation. A pattern displayed by several single points within the control limits may indicate the presence of more than random variation. For example, eight consecutive points are above the center line, a trend of eight or more increasing or decreasing points, or a series of alternating high and low points. These rules can be applied to edge characteristics to gain more information.

SUMMARY

In this chapter, methods for characterizing edge conditions have been presented. The first method attempted for characterizing edge shape, using a NURB, was deemed unusable due to the number of local minima present. A second edge shape characterization procedure using a combination of line, circle, and parabola fitting routines was found to adequately represent all expected edge conditions. Several parabola fitting routines were presented. All methods performed acceptably, but the Bezier fitting routine was chosen because the calculation of residual error used allows for

comparison with the line and circle fitting routines. Residual tracking over an edge area indicates the presence of inconsistencies such as burrs. Parameter tracking by statistical process control methods over the entire edge allows for visualization of shape change. Results from applying the methodology developed in this chapter to data collected by the CLSM are presented in Chapter 5.

CHAPTER 4: RESULTS

The CLSM is used to measure a variety of microscale and mesoscale edges. Several objects made of different materials with different edge sizes, conditions, and shapes were measured and analyzed as described above.

PROCESSING STEPS

In order to characterize data collected by the CLSM, several processing steps are needed. It is assumed that the data collected by the CLSM have been trimmed to a reasonable number of points, but still contain data from the top and the side of the object. A flow chart representing the processing steps for a single CLSM data set is shown in Figure 4.1. The first step is to fit a cylinder to the data in order to determine the orientation of the edge in space. With the orientation known, the CLSM is divided into series of slices. Each slice is then analyzed to determine the size and shape parameters by methods discussed in Chapter 3. These parameters are then collected and analyzed in order to locate any inconsistencies or trends present in the local data set.

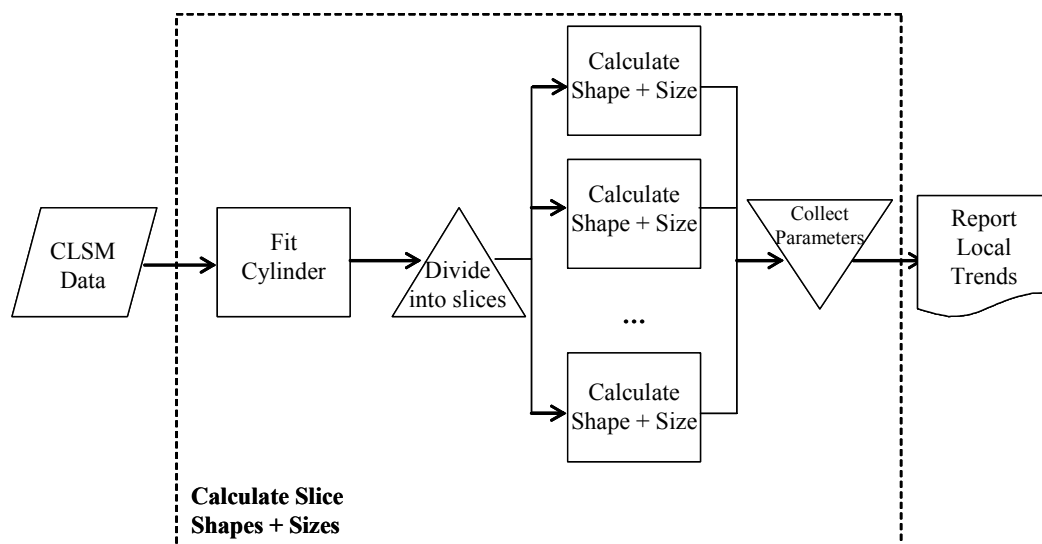


Figure 4.1: Flow chart for processing of single CLSM data set

In order to determine the existence of any global trends in the edges of a single part, shape and size parameters from several measurement areas are compared using statistical process control methods as described in Chapter 3. The flow chart for collecting the data used to locate trends is presented in Figure 4.2. The “Calculate Slice Shapes and Sizes” step is outlined in Figure 4.1.

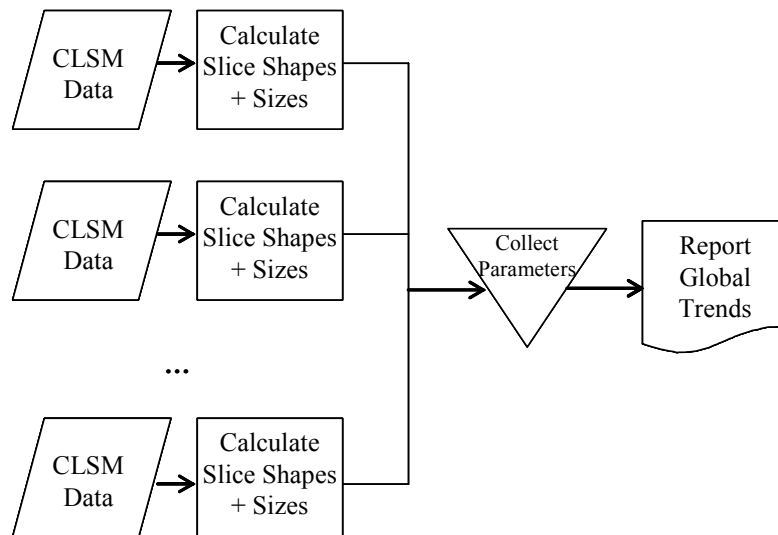


Figure 4.2: Flow chart for processing several CLSM data sets to obtain global trend information

Edge Orientation and Data Sectioning

The first in processing a single CLSM data set is to determine the orientation of the edge in space. This is necessary to create the planes that define the boundaries of each individual slice. A cylinder is fit to the trimmed data to obtain the best-fit axis of rotation. The axis of rotation is parallel to the edge.

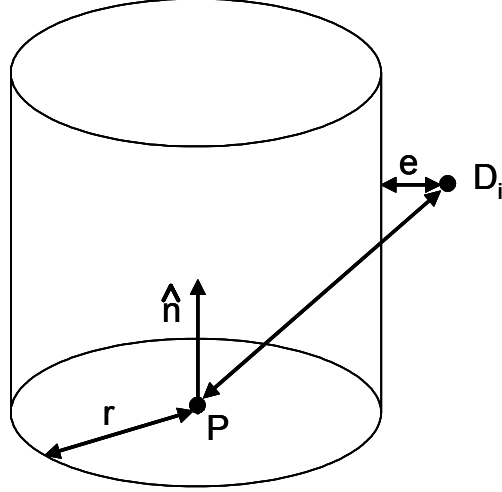


Figure 4.3: Cylinder parameters

A cylinder is defined by several quantities, the radius (r), a unit vector which lies along the axis of rotation (\hat{n}), and a point on the axis of rotation (P). A physical representation of these parameters is shown in Figure 4.3. The point to cylinder deviations for each data point (D_i) can be calculated as shown in Equations (4.1), (4.2), and (4.3) [94].

$$v_1 = D_i - P \quad (4.1)$$

$$v_2 = (v_1 \cdot \hat{n}) * \hat{n} \quad (4.2)$$

$$e = |v_1 - v_2| - r \quad (4.3)$$

In order to perform 2D analysis, the edge must be divided into small sections, or slices. This is done by creating planes perpendicular to the edge at a user-defined interval. All of the data that lies between two adjacent planes is analyzed as a 2D slice.

To facilitate data sectioning, it is useful to transform the edge data so that it is parallel to the z-axis. With the transformation matrix known, the points can be transformed to be axis-aligned using the inverse of the transformation matrix. The number of slices or width of each section is a user-defined quantity. Each point can be

assigned to a slice directly by examination of its z-component. Once the data are divided into slices, they are considered 2D by neglecting the z-component.

The non-edge data must be removed from the edge data in order to calculate the shape and size of the 2D edge. This is done according to the routine established in Chapter 3. The size of the edge is reported and the best-fit shape is determined. The results of all slices from a single measurement are presented together to indicate abrupt changes. The average results from all measurements from each part are presented to indicate trends by location. The processing algorithms described were created and performed using Matlab.

CUTTING TOOL INSERTS

Cutting tools have edges of known shape with an expected size. The size of some cutting tool insert edges lay within the mesoscale edge range considered in this work. Although we are not interested in characterizing the ability of the tool insert manufacturing process to produce consistent edges, cutting tool inserts provide a well-known edge and can be used as an artifact to test the developed edge characterization methods.

Two cutting tools inserts are measured, one with a honed edge as shown in Chapter 2, and one with a chamfered edge. The honed edge tool insert, shown in Figure 4.4(a), is a Kennametal VBMT22111. For honed edge tools there are three main types of hone. This hone is present around the perimeter of the tool. Type “A” is usually a 12.7 μm . radius, Type “B” has a 38.1 μm radius, and Type “C” has a 76.2 μm radius. Additional radii can be made if necessary for specific applications. The tolerances are at best $\pm 12.7 \mu\text{m}$ due to limitations in the manufacturing process [20]. The honed tool has

a clearance angle of 5° and a rake angle of 5° resulting in a cutting edge included angle of 80° .

The chamfered tool insert, Figure 4.4(b), is a Sandvik CNGA432T0625. This tool insert is specified as having a land width of $150\text{ }\mu\text{m}$ at an angle of 25° . The chamfer is present around the perimeter of the tool.

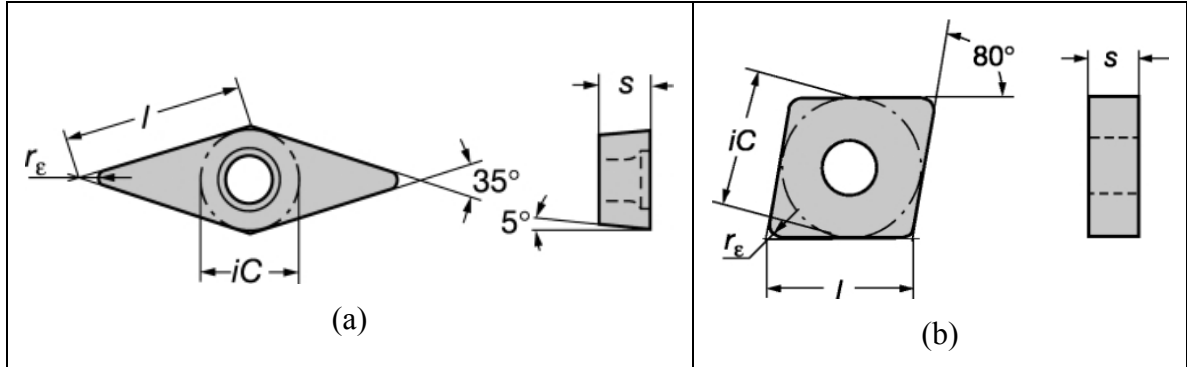


Figure 4.4: Cutting tool insert properties for (a) honed and (b) chamfered tools

Representative data from the chamfered edge and honed edge are shown in Figure 4.5. The data are measured with the part held at approximately a 45° angle. Specimen tilting has also been used in work by Hattori et al. [95] to minimize the influence of a steep slope. Several angles were chosen, and it was observed that, for the chamfered tool, an angle that results in the chamfered section of the tool edge close to perpendicular to the light tend to require a lower detector gain, making it more difficult to measure the top and side.

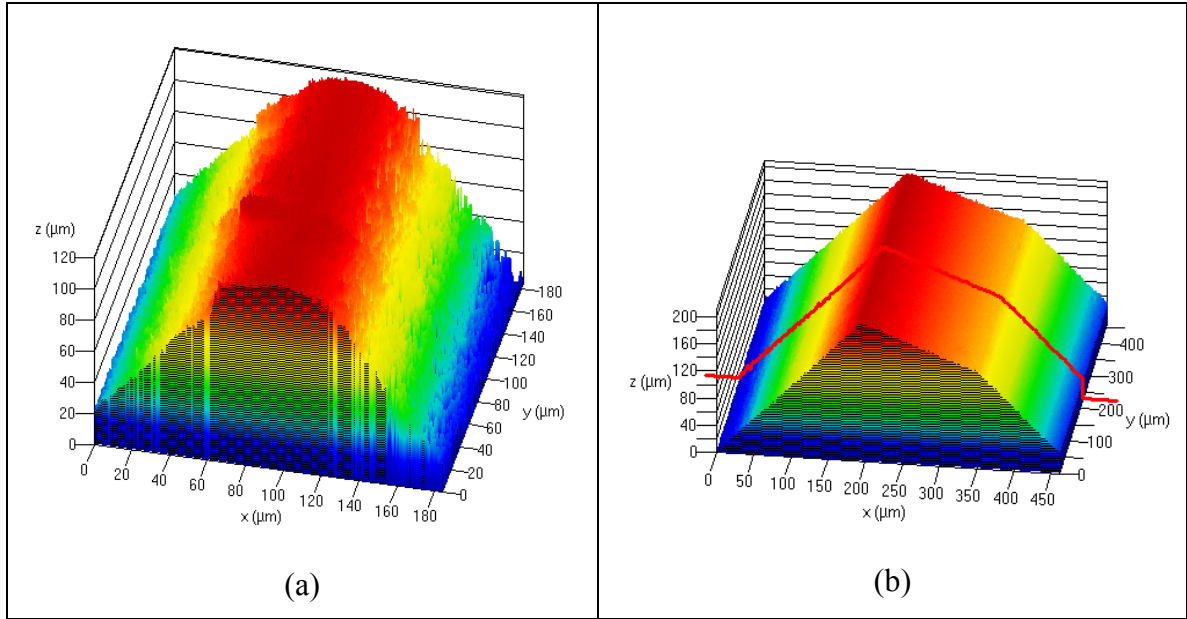


Figure 4.5: Representative data set from tool inserts

Chamfered Tool

The chamfered tool was measured in 12 locations, evenly spaced across the four sides of the top edge of the cutting tool (2 per side). Each measurement is made with the 20x objective, resulting in a point spacing of $0.90\ \mu\text{m}$, covering an approximate area of $460\ \text{by}\ 460\ \mu\text{m}$. The axial point spacing is $2\ \mu\text{m}$.

For each measurement location, the edge was broken into 20 slices. For each slice, the edge is determined by the method previously described. The height is defined as the distance that the edge covers along the side of the tool and the land length is the distance that the edge covers along the top of the tool, as shown in Figure 4.6

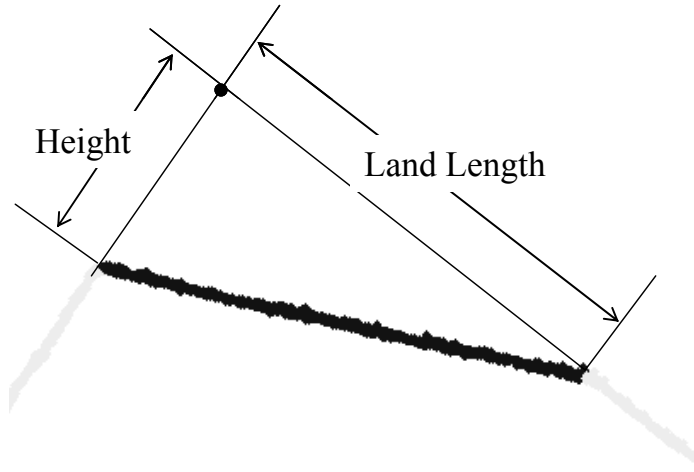


Figure 4.6: Land length and height for chamfered edge

Data from one measurement area are considered. The calculated height and land length and the residuals from fitting a line to the edge data for each slice are presented in Figure 4.7. Data from all slices are presented in the Appendix. The average land length is $146.1 \mu\text{m}$ and the average height is $65.5 \mu\text{m}$, resulting in an angle of 23.8° . The standard deviation of land length measurement ($\sigma = 5.6 \mu\text{m}$) is greater than the standard deviation of the height measurement ($\sigma = 2.5 \mu\text{m}$). This is caused by the procedure for separating the top and side data from the edge data. The land length and height is highly dependent on the determined intersection between the edge data and the top data. The angle between the top and the edge is approximately 24° . Because the angle is relatively small, some edge points may appear to lie on the top surface. The transition from side to edge has an angle of approximately 66° . The sharper angle results in less variation in edge height measurements.

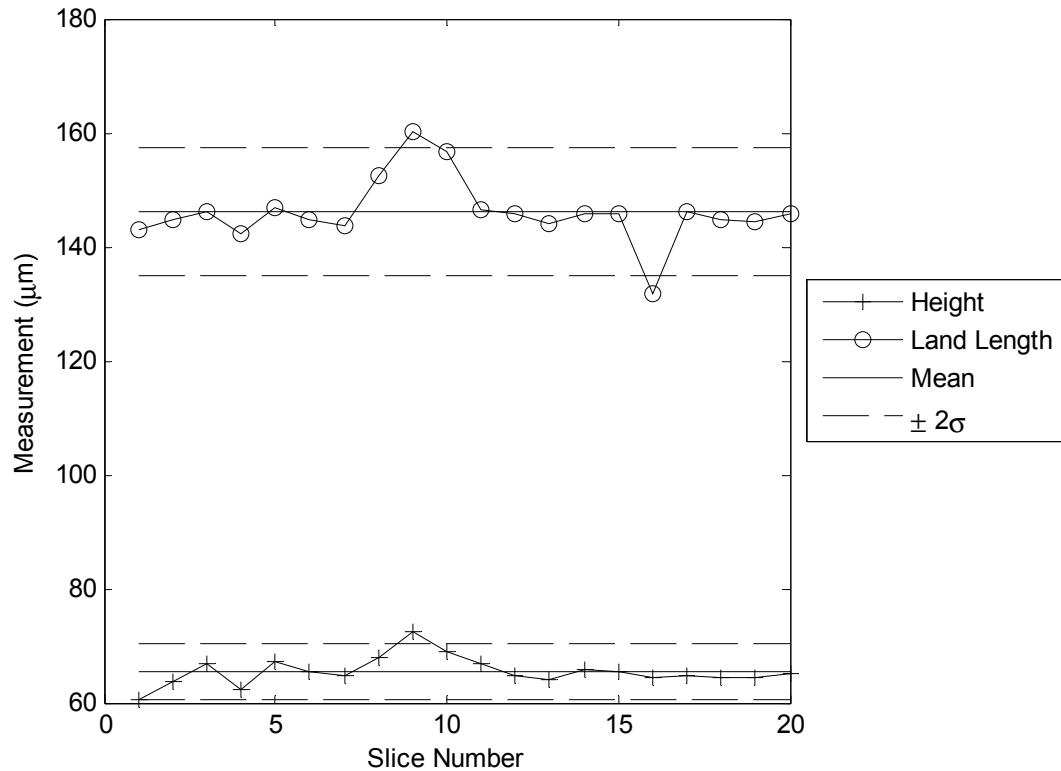


Figure 4.7: Measured values vs. slice number for a single chamfered tool measurement

By inspection of Figure 4.7, it can be seen that slice 9 lies beyond 2σ for the height measurement and slices 9 and 16 lie beyond 2σ for the land length. Examination of the data from these two slices, shown in Figure 4.8, reveals a region of extra material on the side (to the right of the images) of slice 9 and a burr on the edge of slice 16. Because the side of slice 9 does not conform to the edge separation assumption that the top and side be linear in 2D, the size of the separated edge is a function of the condition and side data. This is an example of a Type I error. In statistics, a Type I error is a false negative and a Type II error is a false positive. In this case, a slice with a good edge was indicated due to a problem not on the edge but on the side. For initial studies, it is preferable to have a Type I error to a Type II error because edges are flagged for careful examination, not for rejection.

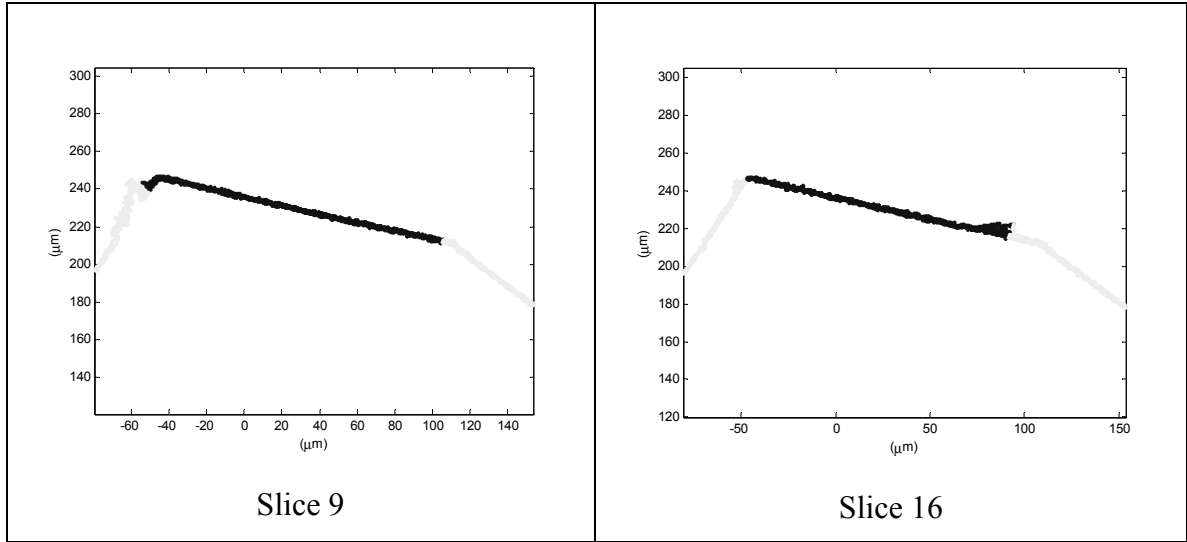


Figure 4.8: Slices 9 and 16 from chamfered tool

In addition to being evident in the plots of height and length vs. slice number, the effect of the extra material present in slices 9 and 16 is also visible in the plot of the line-fit residuals vs. slice number, given in Figure 4.9.

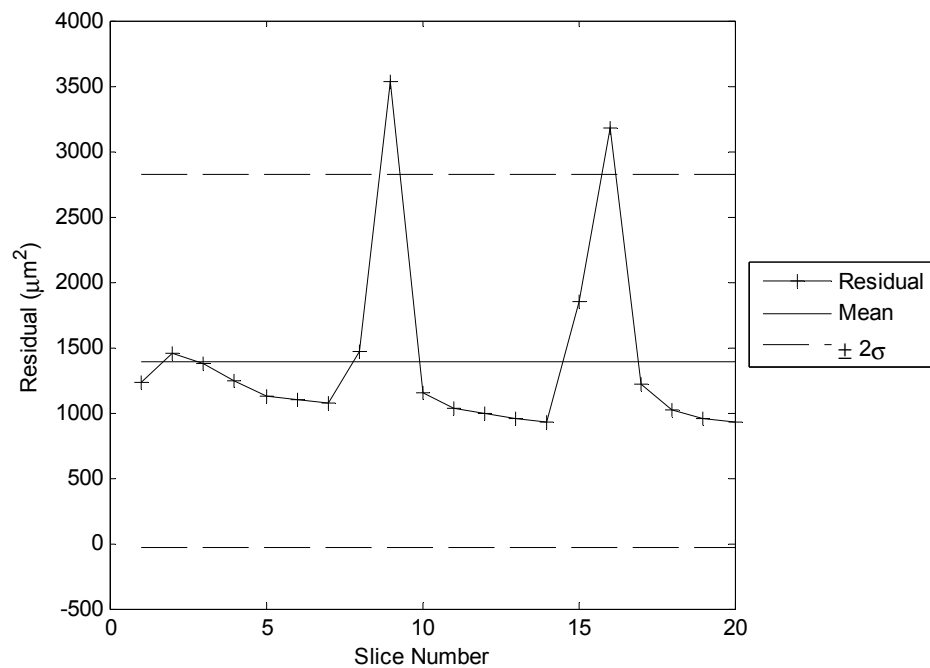


Figure 4.9: Residual values vs. slice number for chamfered tool measurement

The height, land length, and residuals were determined for 20 slices for each of 12 measurement areas on the chamfered tool. A plot of the average land length and height along with error bars representing two times the standard deviation for each of the measurement areas is shown in Figure 4.10.

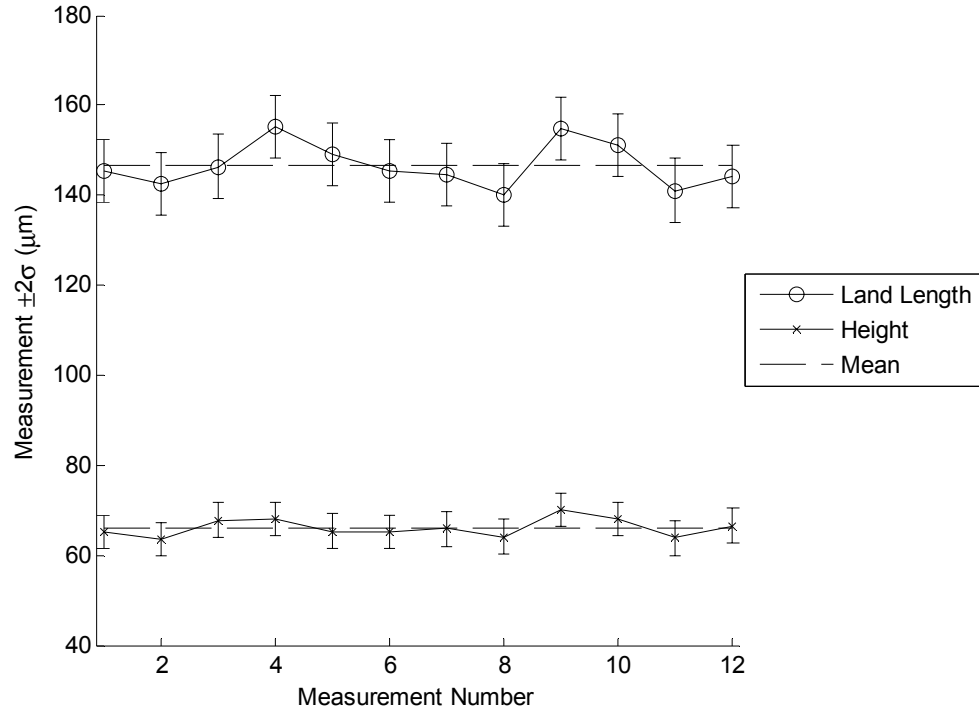


Figure 4.10: Average land length and height, with 2σ error bars, for chamfered tool

A plot of the land length for each of the slices of each of the measurements, 240 slices total, is shown in Figure 4.11. Vertical lines mark the boundaries of measurement areas. The mean and standard deviation (σ) of all slices are calculated for both the height and land length. Lines representing the overall mean and $\pm 2\sigma$ are displayed.

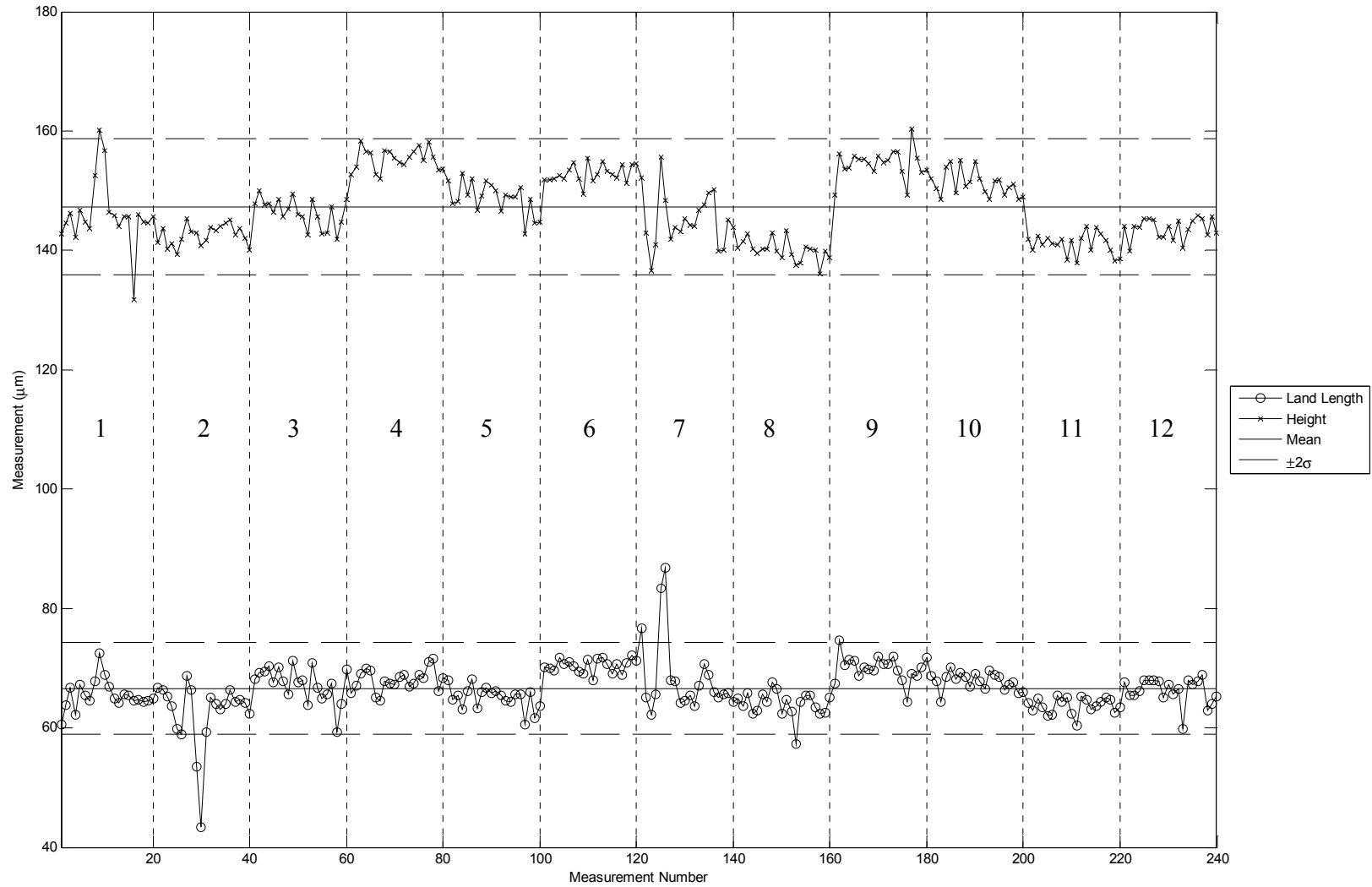


Figure 4.11: Height and land length for all measurements of chamfered tool

Several observations can be made by examining the data. First, there are a significant number of outliers which have the effect of increasing the standard deviation of the measurement. As shown previously, these outliers indicate local disturbances, and thus are not considered representative of the data as a whole. The second observation that can be made is that, while the data within a measurement is generally consistent, there is a great deal of variation from measurement to measurement. Statistical process methods are used to gather more information regarding this observation.

Because the level of variation between measurements for land length seems to be greater than the level of variation in the height, \bar{X} -bar and S charts will be constructed for this variable. The construction of \bar{X} -bar and S charts is discussed in detail in Chapter 3. As previously stated, the outliers within a measurement indicate a local disturbance. Because we are interested primarily in detecting global trends, points outside of $\pm 3\sigma$ are removed. Thus, the sample size (n) varies from measurement area to measurement area, between 17 and 20.

The average (\bar{X}) and standard deviation (S) of the measurement area are calculated by consideration of the land length (X_i) for each slice within the measurement. In order to obtain the upper control limit, lower control limit, and control limit the average standard deviation (\bar{S}) and the average value ($\bar{\bar{X}}$) of the measurement areas are calculated. The calculations for these quantities as well as the upper, lower, and central control limits are in Chapter 3 as Equations (3.17) to (3.22). The \bar{X} -bar chart is given as Figure 4.12 and the S chart is given as Figure 4.13.

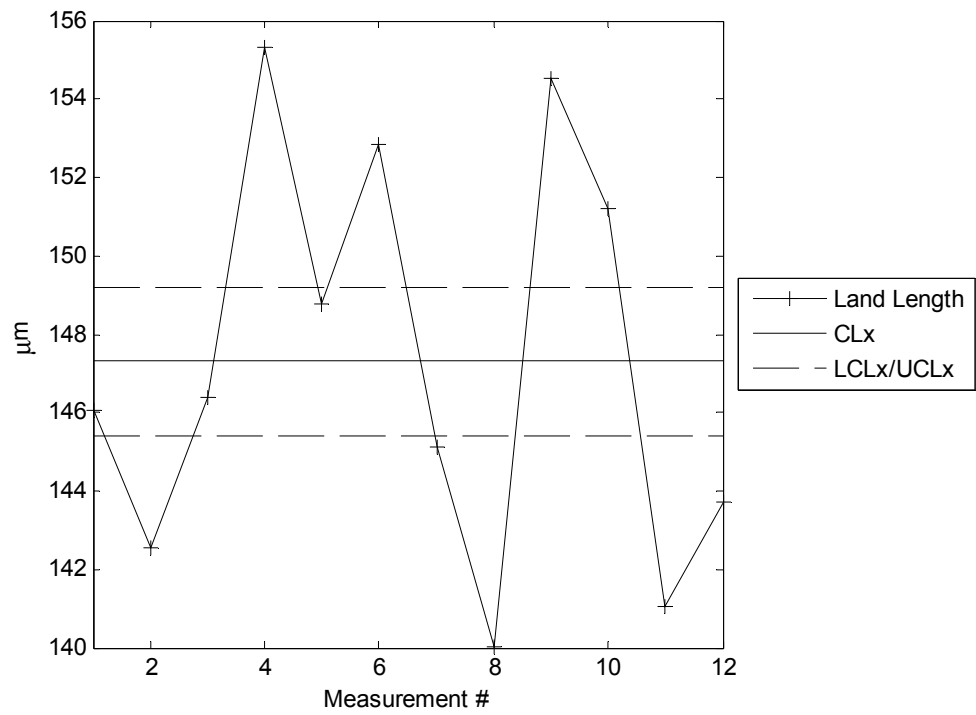


Figure 4.12: X-bar chart for land length of chamfered tool

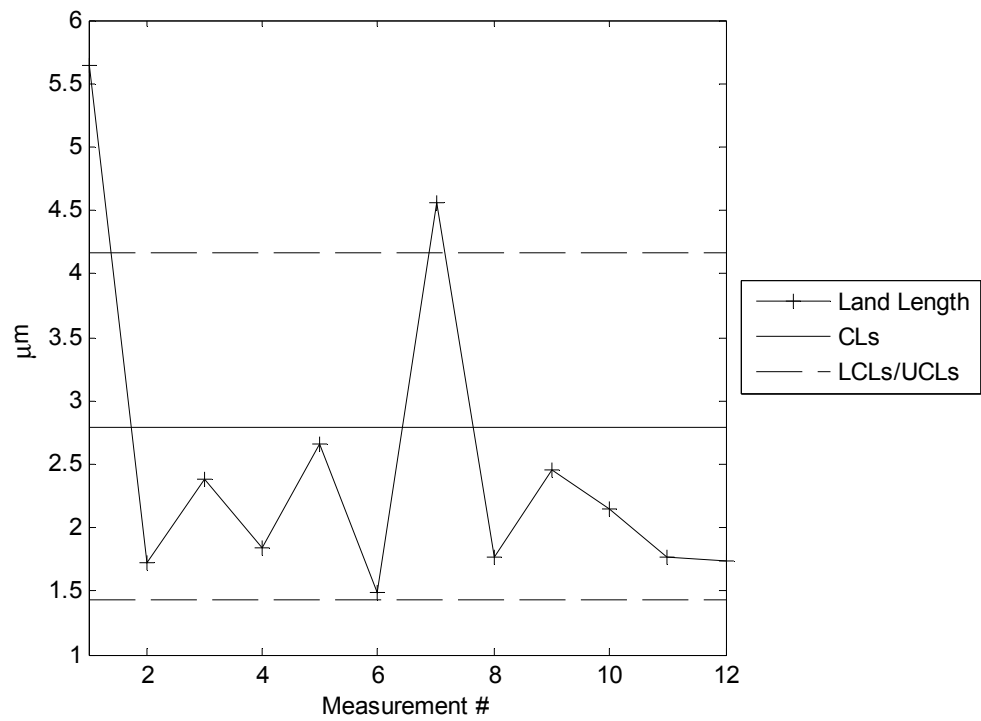


Figure 4.13: S chart for land length of chamfered tool

The X-bar chart displays the average land length value for each of the measurement areas (with outliers removed). Although no trends are apparent by examination of the X-bar chart, the data reveal that this process is considered “out of control” because more than one (in this case 9 out of 12) values exist beyond the upper or lower control limits. The relative compactness of the control range indicates that the standard deviations of the individual measurement areas are relatively small. The S chart confirms the controlled local standard deviations (except in measurement 7). The presence of a number of points outside of the control limits in the X-bar chart indicates that there is a wide range of reported values that can not be explained by random variation. This is confirmed by inspection of land length data in Figure 4.11. This variation can be attributed to either production or measurement conditions.

To ensure that the variation is a function of measured quantities rather than processing algorithms, representative sample slices from measurement areas 4 and 8 are displayed in Figure 4.14. The slice from measurement area 4 clearly has a greater land length than the slice from measurement area 8. Therefore, it is apparent that the variation that exists within the measured data and is not a function of processing algorithm but instead is a function of the measured data. The variation in measured data can be caused by either the manufacturing process or the measurement tool. In this case it appears that the data from the CLSM are of high quality so the variation can be attributed primarily to the manufacturing process.

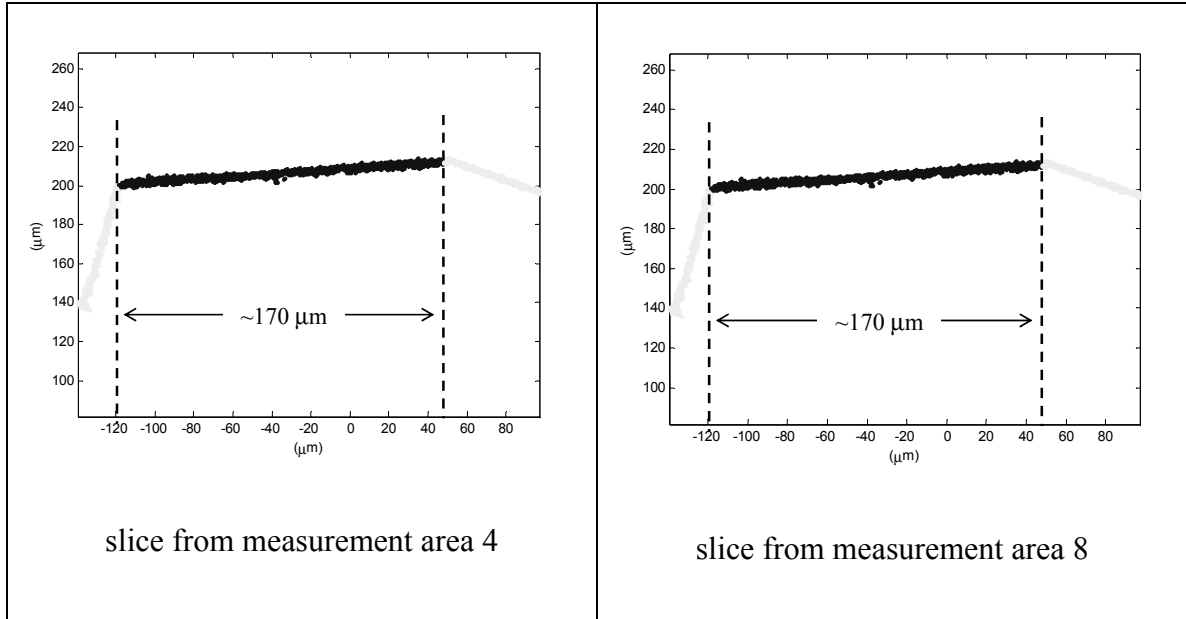


Figure 4.14: Representative slices from measurement areas 4 and 8 of chamfered tool

Honed Tool

The honed tool was measured in 16 locations, evenly spaced across the four sides of the top edge of the cutting tool (4 per side). Each measurement is made with the 50x objective, resulting in a point spacing of $0.36\ \mu\text{m}$, covering an approximate area of 184 by $184\ \mu\text{m}$. The axial point spacing is $1\ \mu\text{m}$. Each measurement is divided into 20 slices. The edge is extracted from the top and side data in the same manner as the chamfered tool. The included angle, θ , is recorded as the angle between the fit lines for the top and side. The radius of the edge, r , is calculated by fitting a circle to the edge data. These quantities are diagrammed in Figure 4.15.

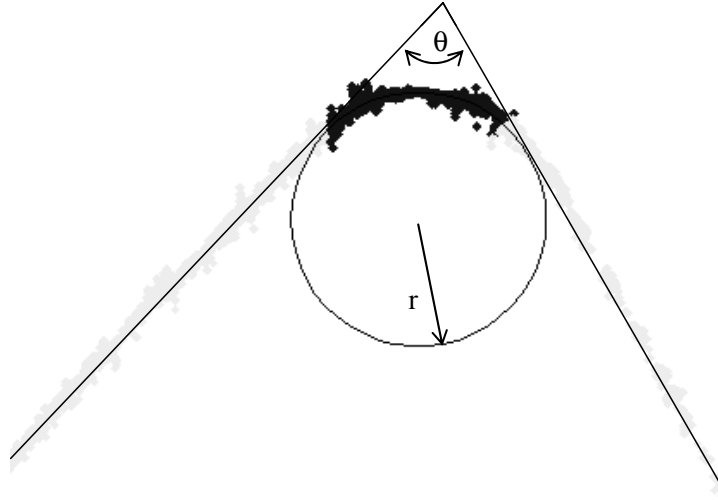


Figure 4.15: Angle (θ) and radius (r) for honed edge tool insert

Representative data from a single measurement are analyzed. The average fit radius for the 20 slices is $34.4\text{ }\mu\text{m}$ with a standard deviation of $11.5\text{ }\mu\text{m}$. The average included angle is 74.6° with a standard deviation of 1.2° . The calculated radius and included angle for each slice are presented in Figure 4.16. The residuals of the circle fit used to find the radius are shown in Figure 4.17. Data from all slices are presented in the Appendix.

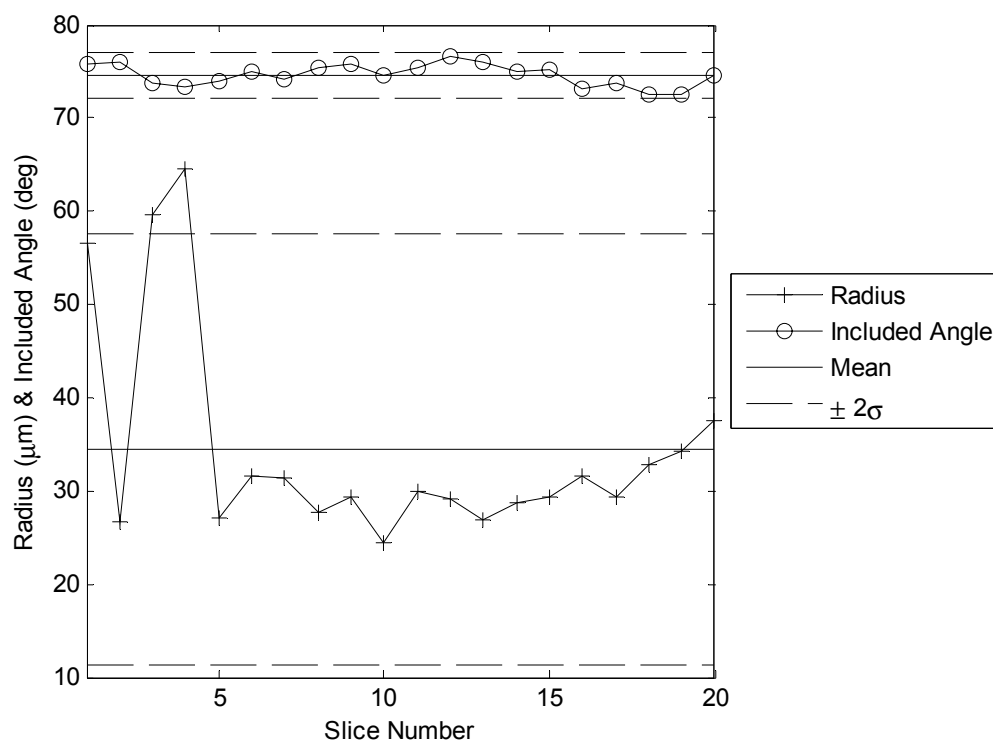


Figure 4.16: Radius and included angle for representative honed measurement area

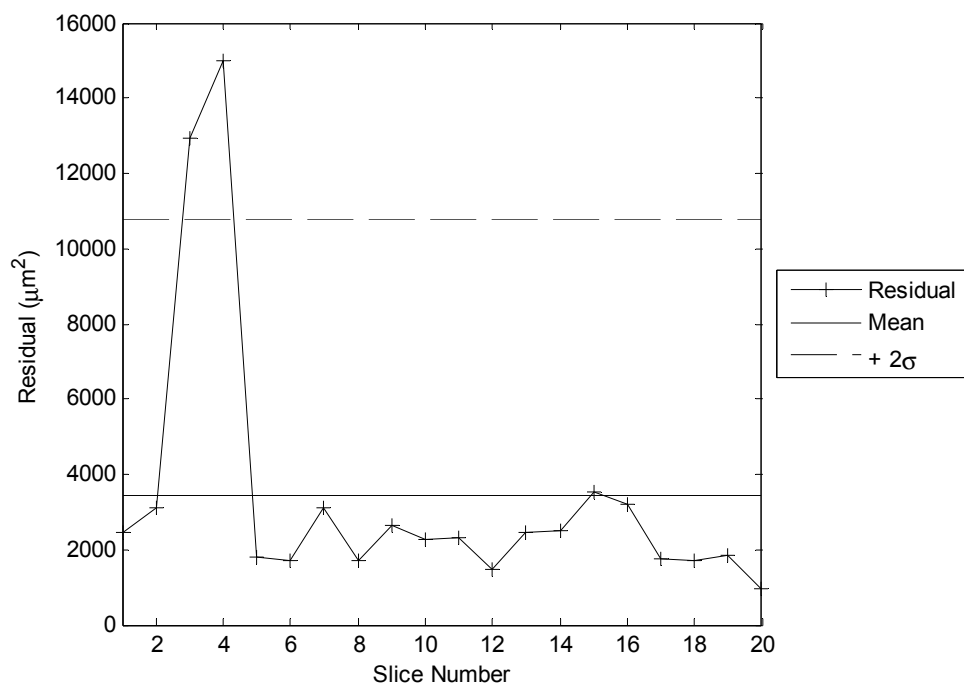


Figure 4.17: Circle fit residuals for representative honed edge tool measurement area

From the data presented in Figure 4.16 and Figure 4.17, slices 3 and 4 require further consideration due to the fit residuals and radii which both lie beyond 2σ . Figure 4.18 provides the data from these two slices. Examinations of the data reveal that the edge finding algorithm has included points in the edge that appear to be on the side of the tool. This is because the side of the tool is not linear; there appears to be a slight protrusion in the collected data. This protrusion causes the line defining the side to be shifted. The data points are assigned to the edge because they do not lie on the shifted line. Therefore, examination of the edge radius and associated residuals of this measurement area reveals a slight protrusion on the side of the tool.

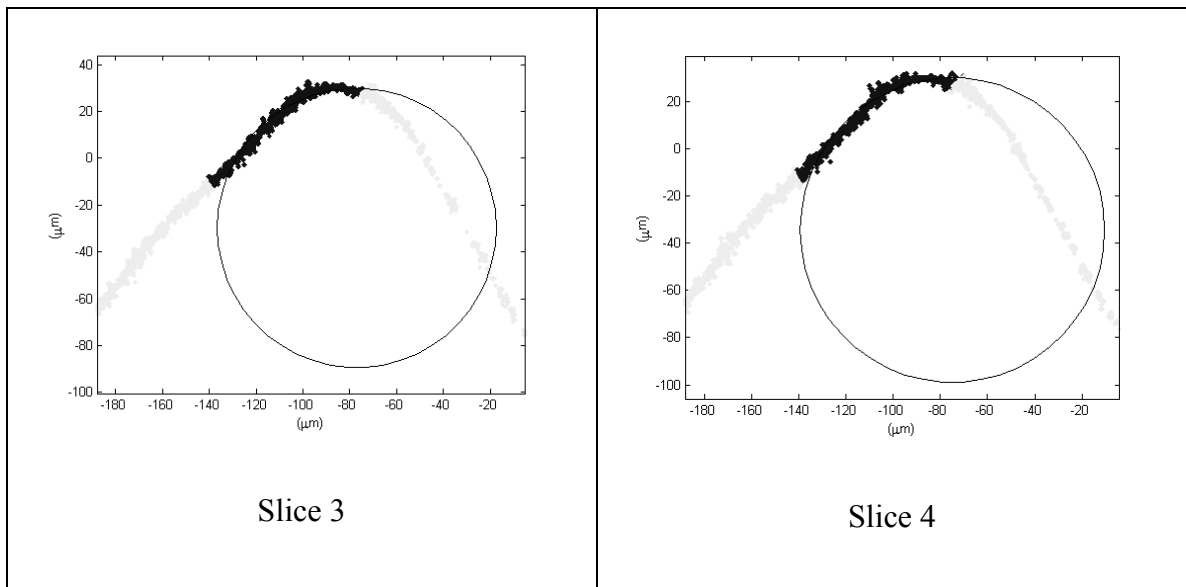


Figure 4.18: Slices with residual values and radii outside of 2σ

In addition to inspection of a single measurement area to locate local inconsistencies, data from 16 measurement areas representing the entire tool edge are considered to analyze global trends. Data from 20 slices for each of 16 measurement areas are presented in Figure 4.19.

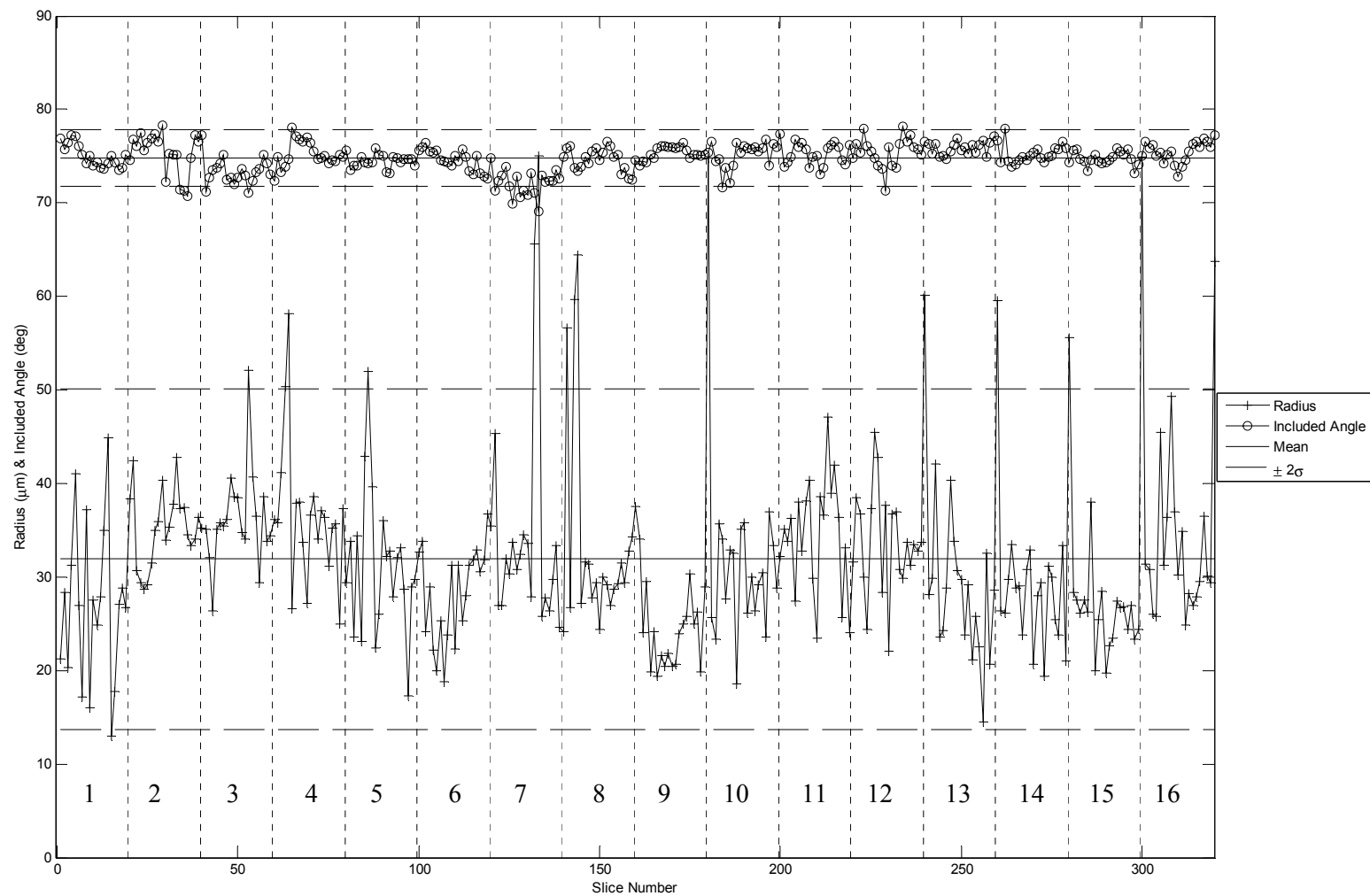


Figure 4.19: Radius and included angle for all slices of all measurement areas of honed tool

The mean radius of all slices from all measurement areas is 31.9 μm with a standard deviation of 9.1 μm . The mean for included angle is 74.8° with a standard deviation of 1.5°. The relatively low number of points representing the edge (when compared to the number of points representing the top and side) in combination with the apparent noise in the data is one cause for higher variance in the radius fit. Another cause of high variance is the instability of the edge point extraction method when faced with non-linear edge and side data, as observed in Figure 4.18.

X-bar and S charts were created for the radius and the included angle. The outliers of each measurement area were removed from the radius calculations because they are indicative of problems with the side and top data and not necessarily the edge radius. The remaining data was used to create X-bar and S charts for the radius. The X-bar and S charts for the included angle are based on all collected data. The data is processed in the same manner described for the chamfered tool.

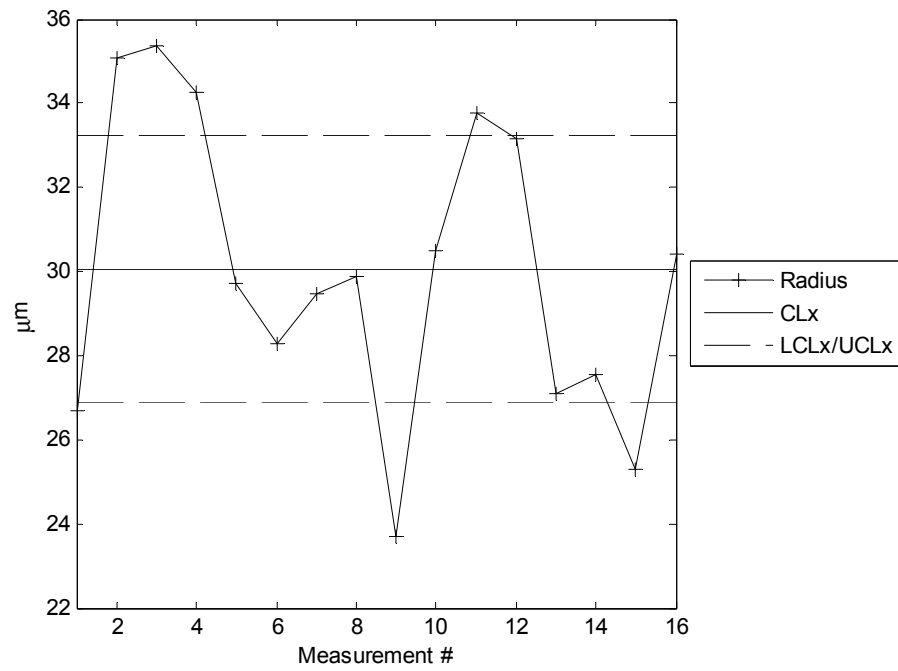


Figure 4.20: X-bar chart for radius of honed tool, outliers removed from individual measurements

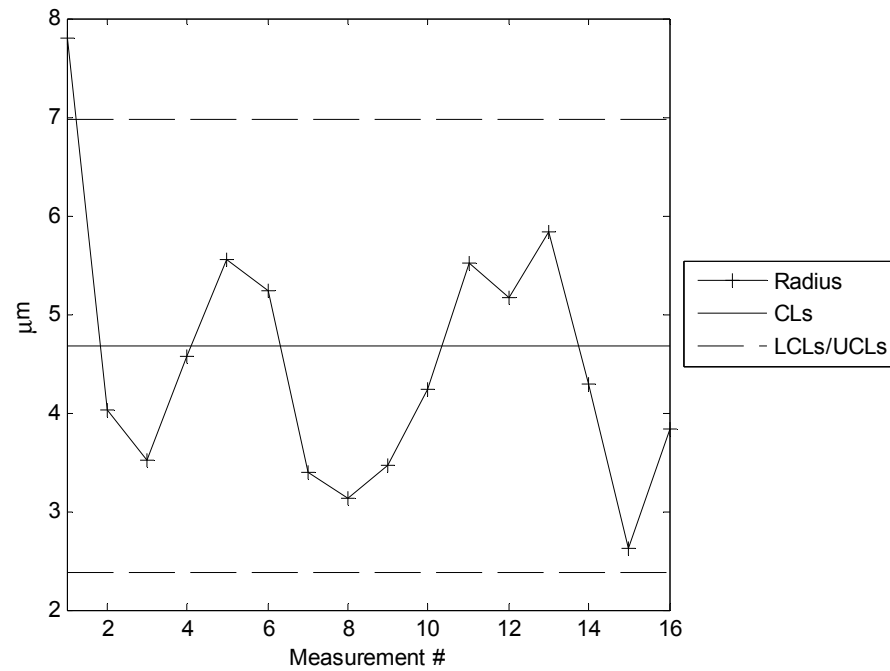


Figure 4.21: S chart for radius of honed tool, outliers removed from individual measurements

The data from measurement areas 3 and 9 (the maximum and minimum values) are considered more closely in order to explain the discrepancy between their average values. Unlike with the chamfered tool, there does not appear to be a clear explanation for the difference in average values. Most likely this is because the data collected for the honed tool are not complete. A full data set includes 512x512 data points, a total of 262,144. The average data set collected for the honed tool includes 155,270 points, or 59.2% of a complete data set. Additionally, the data appears to contain more variation (noise) than the chamfered data. This is clear in the data presented as Figure 4.22.

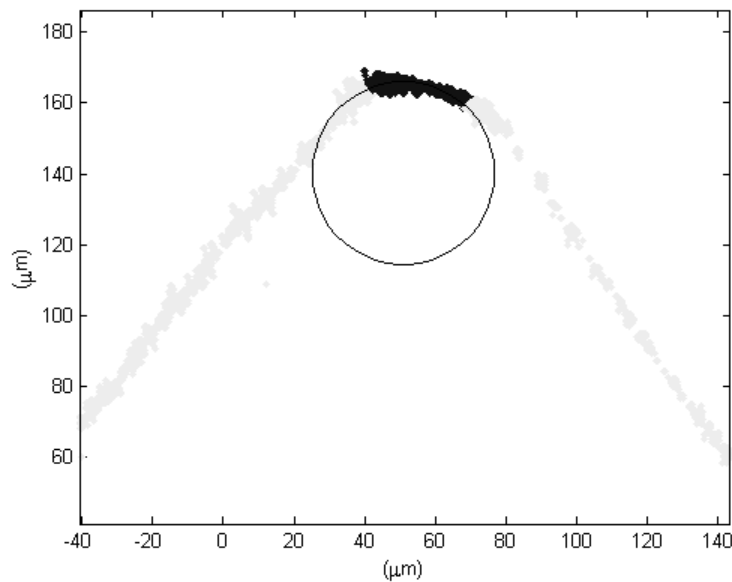


Figure 4.22: Honed edge tool data

With noisy data, it is more difficult to distinguish the edge from the top and the side. Small changes can have a large impact on the final measured quantities. Based on these results, it appears that the data collected by the CLSM is not sufficient for locating trends. Local inconsistencies in the top and side of the object are detectable using

methods described but edge problems (i.e., burrs) and global trends are not detectable due to the poor condition of the collected data.

Tool Insert Conclusions

Several conclusions may be drawn from the tool insert studies. The tools presented in Chapter 3 are used to successfully identify burrs and track edge size for the chamfered tool. Inconsistencies on the top and side of the tool are visible and appear as changes in the size of the edge and increased fit residuals. By the control charts there are no evident trends in tool size and it appears that the process used to create a chamfered edge is not well-controlled.

Measurement of the honed tool was not as successful and leads to difficulties with characterization. Local inconsistencies with the top and side were visible, but burrs and global trends were not detectable due to the poor condition of the data. A metric for wellness of CLSM measurement data is needed.

LIGA

In previous studies LIGA edges have been measured as circular with a radius of 2 to 2.5 μm , shown in Figure 4.23 [2; 62]. The small edge size requires a high power objective, in this case 150x.

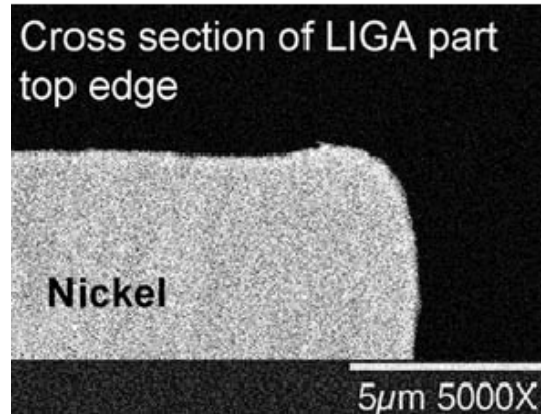


Figure 4.23: LIGA edge structure measured by X-SEM [62]

Using a high power objective results in a small measurement area, approximately $62 \times 62 \mu\text{m}$. For a 150x objective, the lateral point spacing is $0.12 \mu\text{m}$ and the lateral resolution of $0.35 \mu\text{m}$. The axial point spacing is $0.25 \mu\text{m}$ and the axial resolution is $0.84 \mu\text{m}$. Representative edge data are displayed as Figure 4.24.

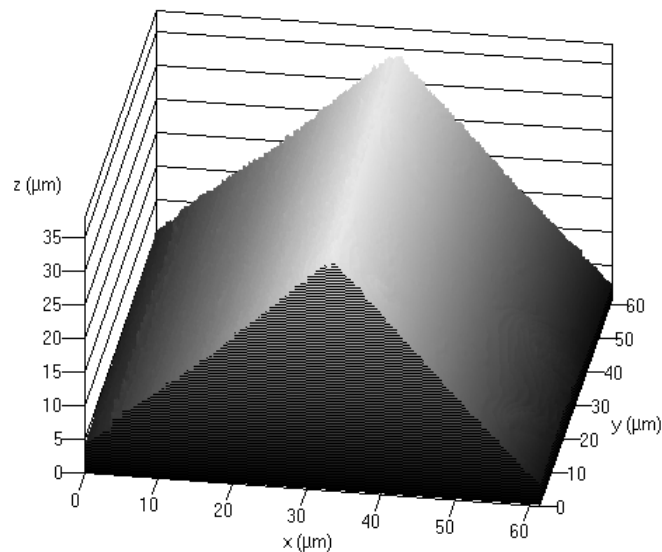


Figure 4.24: LIGA edge measured at 150x

Although the measurements successfully captured the edge area, the small edge size in combination with the relatively high lateral and axial resolutions (0.35 and 0.84 μm , respectively) leads to difficulty in distinguishing the edge from the top and the sides.

Four measurements were made along an edge created by two intersecting planar surfaces. Inquest, a software program which allows the fitting of data to models, is used to fit the edge data to a model of a cube. The results of these fits demonstrate the difficulty in differentiating between the edge and the top or side surface.

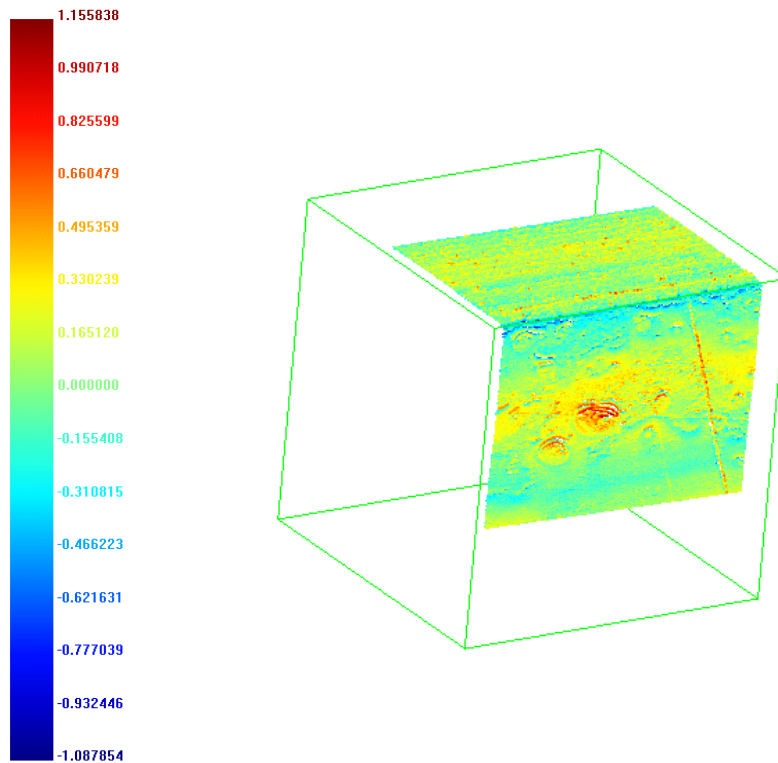


Figure 4.25: Representative fit of LIGA edge data to 70 x 70 x 70 μm cube

Figure 4.25 is representative of the results from the four data sets. For this fit, the standard deviation of error is 0.181 μm and the maximum error is 1.156 μm . Note that the maximum error is shaded in the darkest red, and does not occur at the edge but on the side plane of the data. This is true of all four data sets. Mean deviation, maximum error

and standard deviation of errors are presented in Table 4. To determine normality of the data, a QQ-plot is generated using the residuals of the data from the first scan. This plot, Figure 4.26, shows that the data are fairly normally distributed. The deviations from the line at the ends may be a result of surface scratches and imperfections.

Table 4: Resulting deviations and errors from LIGA edges

Scan #	Mean Deviation	Standard Deviation of Error	Maximum Error
1	0.000 μm	0.181 μm	1.156 μm
2	0.000 μm	0.190 μm	1.388 μm
3	0.000 μm	0.244 μm	1.675 μm
4	0.000 μm	0.312 μm	3.247 μm

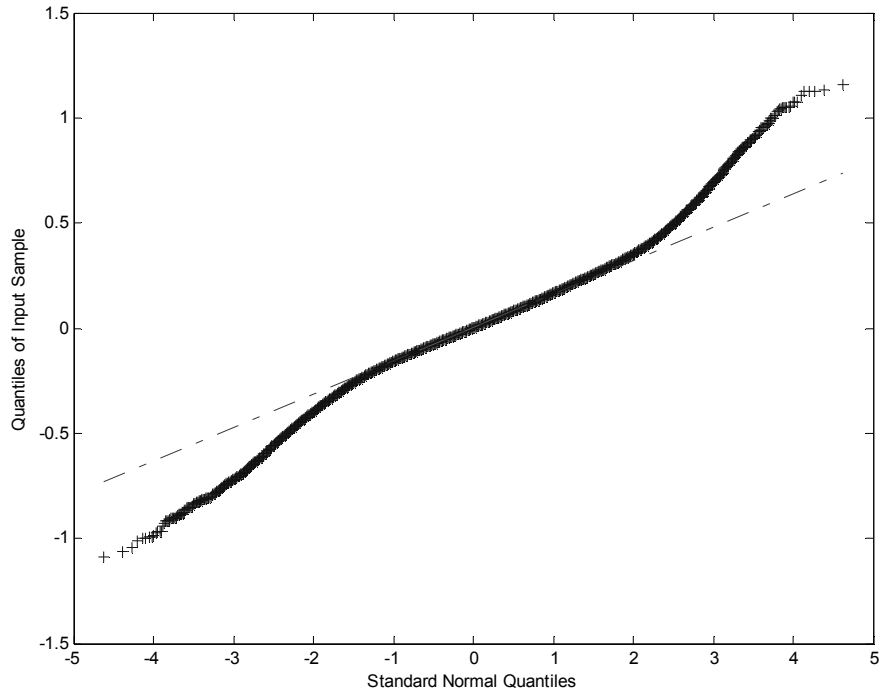


Figure 4.26: QQ plot of residuals vs. standard normal

In order to properly characterize the edge, it is necessary to understand where the edge starts and stops. Figure 4.27(a) shows representative edge data at an angle and Figure 4.27(b) shows a side view of the same data. The edge finding method described earlier uses the standard deviation of a line fit to the top and side data. The edge is difficult to locate when this methodology is applied to the LIGA due to a combination of CLSM noise levels and insufficient measurement resolution. An alternative measurement method is required to properly inspect these edges.

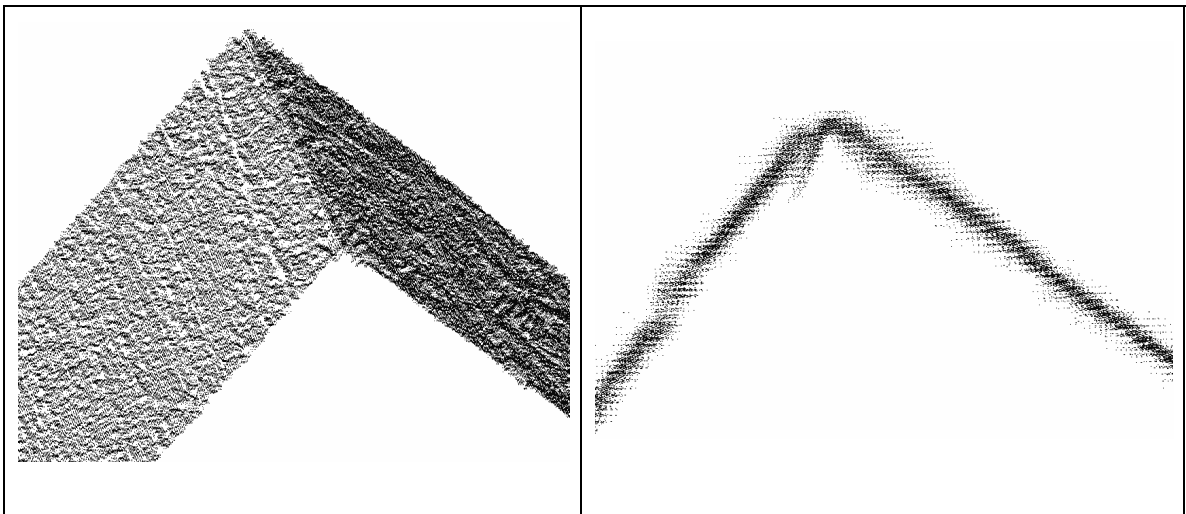


Figure 4.27: LIGA edge data

STEREOLITHOGRAPHY

Test parts that were previously built to test the smallest negative feature size of the SLA Viper Si are used as an edge measurement case study. The CAD model of the test parts is given in Figure 4.28. These parts have holes with diameters ranging from 0.05" to 0.005" in 0.005" increments, resulting in 10 holes per part. Using the Lightyear 1.2 slicing software, the layer thickness was set to 50 μm . Linewidth compensation was used, the small feature preservation option was turned on and the smallest feature size was set to zero.

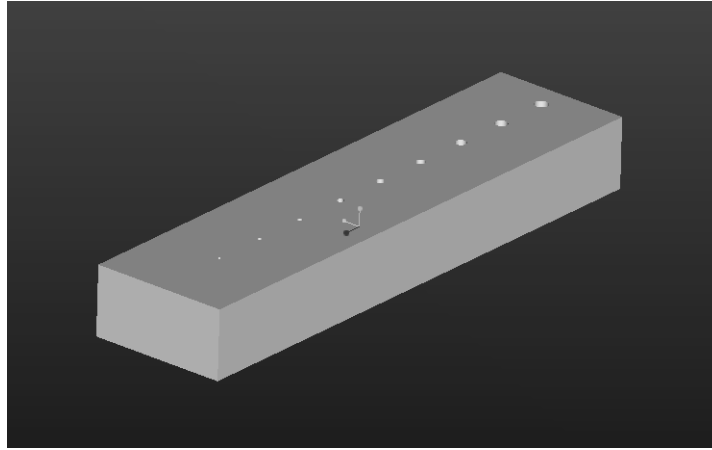


Figure 4.28: Model used for hole test

Originally, four parts were built, in the locations specified in Figure 4.29. Two of these parts were destroyed in initial testing, leaving those located in the plus-x and minus-x locations for edge measurement. All parts were cleaned with TMP and then in alcohol using the ultrasonic cleaner for 20 minutes. They were cured for 60 minutes in the UV oven.

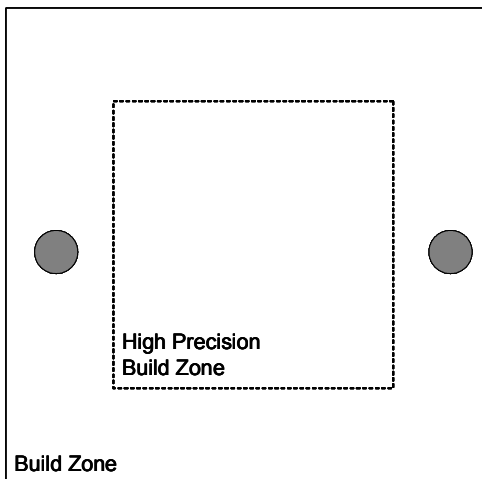


Figure 4.29: Build locations for SLA case study

Parts produced using stereolithography were measured with the CLSM. Like with the tool edges, the SLA edges were tilted at several angles to minimize the slope of the top and sides. Unfortunately, the SLA edges did not measure well at an angle because of

the shape and the relative low reflectivity of the material. However, acceptable measurements were obtained by measuring the edge perpendicular to the top or side plane. For measurements considered in this work, the edge is measured on the side as shown in Figure 4.30, because final edge condition is highly dependent on the top layers which are more visible from the side.

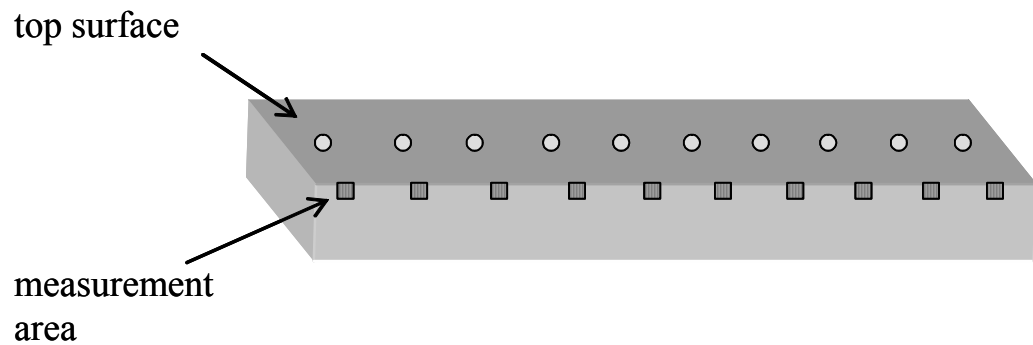


Figure 4.30: Location of measurement area for SLA parts

The data in Figure 4.31 show layers in the x-direction. These layers are a result of the layer-based manufacturing process. In this case the layer thickness was set to 50 μm at build time.

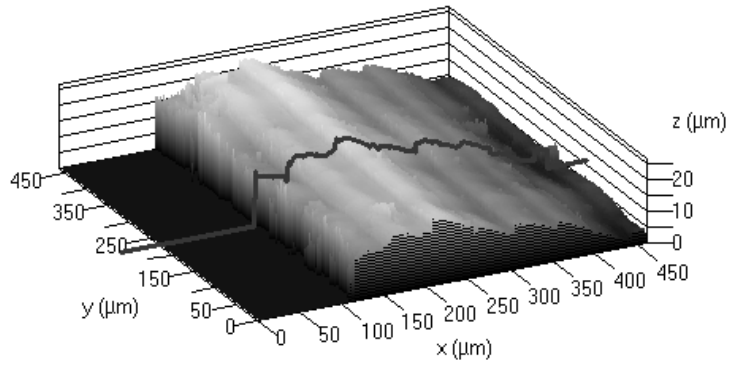


Figure 4.31: Edge of stereolithography part, captured at 20x

The cross section plot in Figure 4.31, with x-divisions at 50 μm , shows that the measured layer thickness is approximately 50 μm . These layers can also be seen at lower magnification, as shown in Figure 4.32, the same edge as Figure 4.31 at 10x magnification. It appears in Figure 4.32 that the edge (on the right) appears to extend to several layers in depth. This is consistent with findings from a previous study which considered grids produced with SLA. By inspection of the data collected, it is observed that edge does not extend past the fifth layer.

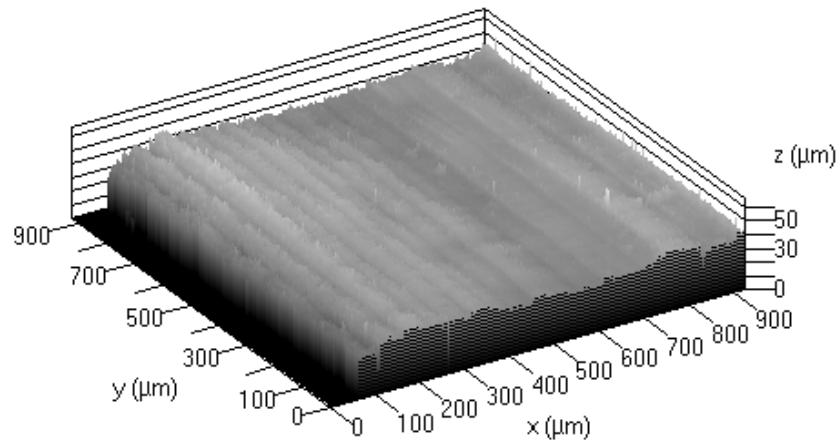


Figure 4.32: Edge of stereolithography part, captured at 10x

The method previously described for characterizing edge shapes is difficult to apply to the SLA edges because defining the start and stop of the edge is not possible by the same method applied to other cases. This is because one of the assumptions made, that top and side data are present is not valid for these SLA parts. For SLA measurements, it is assumed that no data from the top surface are collected so only side data need to be removed.

There is an additional concern present in characterization of these SLA edges; because the top plane does not exist and in most of the measurements, the side is not completely planar, it is difficult to estimate the x and y size of the edge because edge orientation can not be directly determined. To remedy this concern, the data collected from non-edge layers (below the fifth layer) are assumed to be nominally planar, as is specified in design, so a plane can be fit to determine the edge orientation. Figure 4.32 shows a large area from the side that is relatively planar.

Because the shape is not specified in design, a parabola, a circle and a line are all fit to each slice of edge data. Each edge measurement is divided into ten slices. Fitting a

parabola is computationally intense because it requires that roots be found for each point, for each iteration. With a slice containing tens of thousands of points, the process of fitting a parabola takes 10s of minutes. In order to decrease computation time, points containing the same x-value are averaged to create a single line. By averaging, burrs and small inconsistencies may be eliminated. The light gray line shown in Figure 4.33 is the result of averaging the points. Note that the scales for the two axes are different. Using the average line in place of all data points results in processing times of less than one minute per slice. After the points are averaged, the edge data is separated from the side data using the same algorithm described in Chapter 3, except only side data is removed because the top surface was not measured.

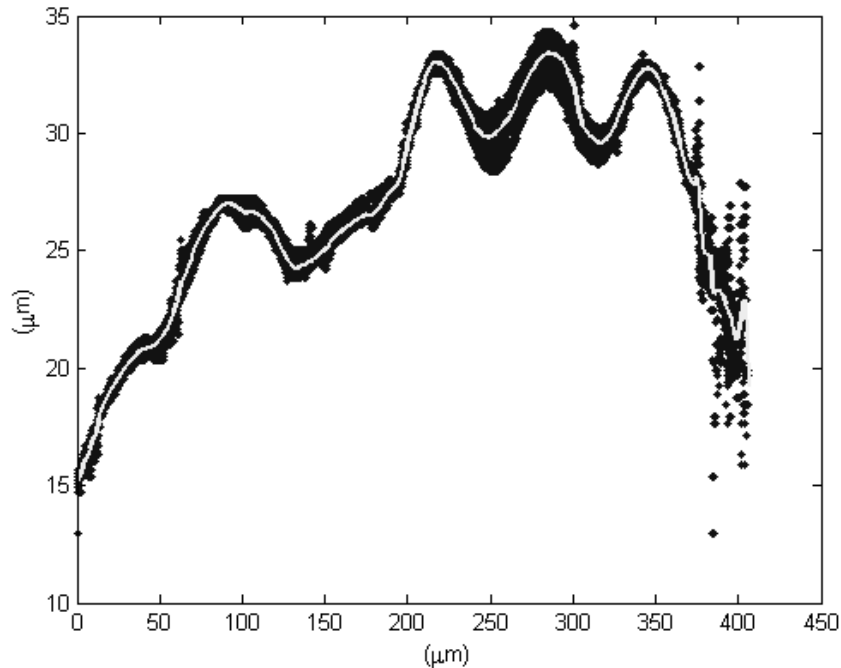


Figure 4.33: Line created from SLA edge data

In stereolithography, the final edge conditions are not well characterized. As a result, understanding edge shape and size are of great importance in this study. The

change in edge shape with respect to build location is also of interest. To determine the edge shape, a circle, line and parabola, are fit to each slice. Local inconsistencies are not considered. Trends are tracked by considering all measurement areas for each part.

Plus-X

The first part, made in the plus-x location, was measured in 20 places, evenly spaced across the two long sides of the top edge (10 per side). Each measurement is made with the 20x objective, resulting in a point spacing of $0.90\text{ }\mu\text{m}$, covering an approximate area of $460\text{ by }460\text{ }\mu\text{m}$. The axial point spacing is $2\text{ }\mu\text{m}$.

Edge shape is determined for each measurement area. For many of the measurement areas, the shape is between a line and a circle, therefore a parabola tends to fit best. In many cases, the vertex is not within the range of the data so parabola parameters are not acceptable for reasons discussed in Chapter 3. Examples of acceptable and unacceptable parabola fits are given in Figure 4.34 where vertex and focal point are shown as small circles. The vertex is within the data set in Figure 4.34(a), and not in Figure 4.34(b).

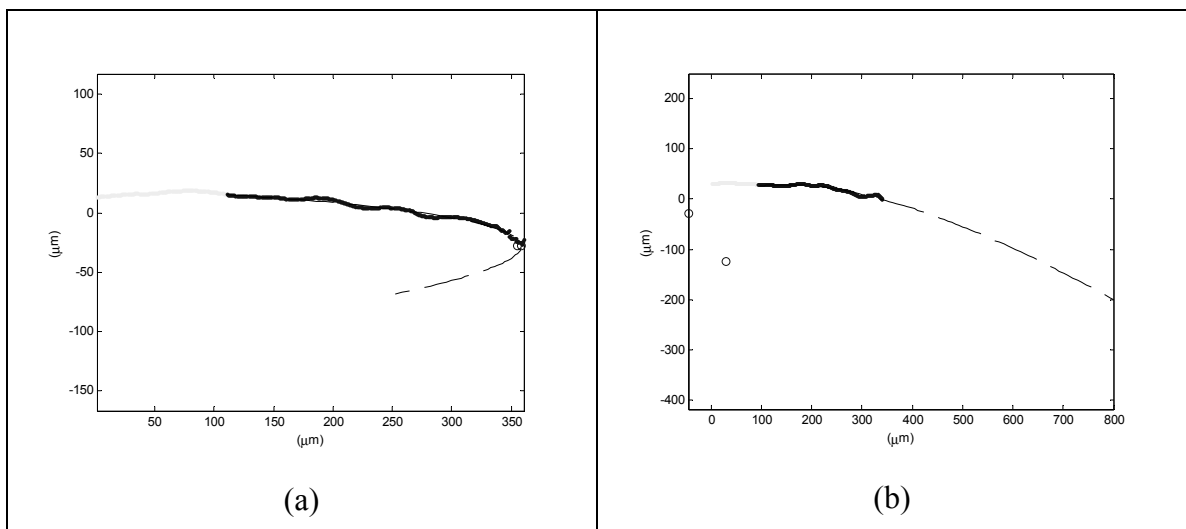


Figure 4.34: Example of acceptable (a) and unacceptable (b) best-fit parabola

The best-fit edge shape is the shape - circle, line, or parabola - which has the lowest residuals in the majority of the slices. Ten slices are considered for each measurement area. The edge shape for each of the measurement areas is presented in Table 5. All slices from measurement area 11, including the best fit line, are presented in the Appendix.

Table 5: Best-fit shape of measurement area for SLA part built in plus-x location

Measurement Area	Best-Fit Shape	Measurement Area	Best-Fit Shape
1	Line	11	Line
2	Line	12	Line
3	Line	13	Line
4	Circle	14	Line
5	Line	15	Line
6	Circle	16	Line
7	Circle	17	Line
8	Circle	18	Line
9	Circle	19	Line
10	Circle	20	Line

By inspection of the best-fit shapes given in Table 5 it appears that best-fit shape is related to part location. Recall that measurement areas 1-10 are from one side of the part, while 11-20 are from the other. The majority of measurements from the first side are best described as circles while all of the measurements from the second side are best described as lines. This will be further considered by analysis of X-bar and S charts for three variables, x-size, y-size and slope, presented as Figure 4.35 through Figure 4.40.

The data presented in Figure 4.35 to Figure 4.40 do not contain results from measurement area 17, because the data file became corrupt.

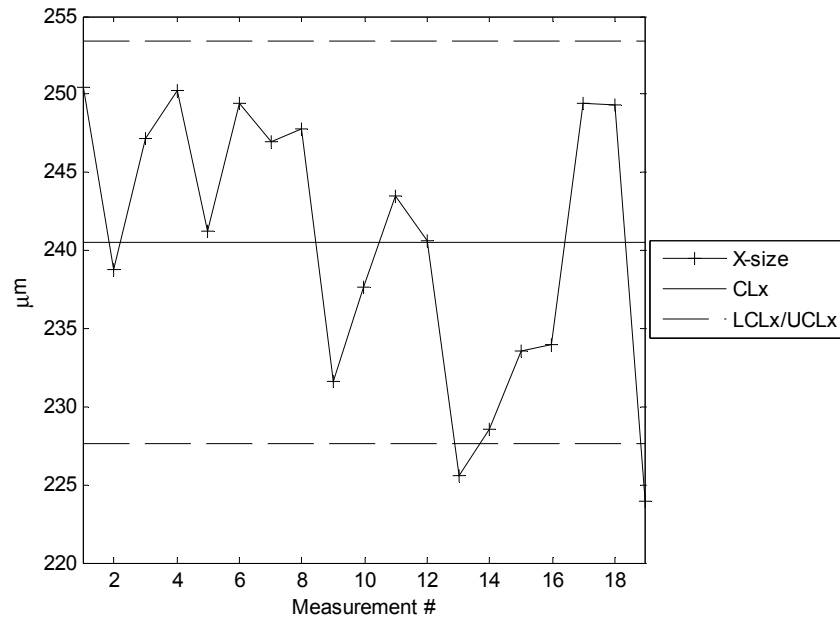


Figure 4.35: X-bar chart for x-size of SLA part built in plus-x location

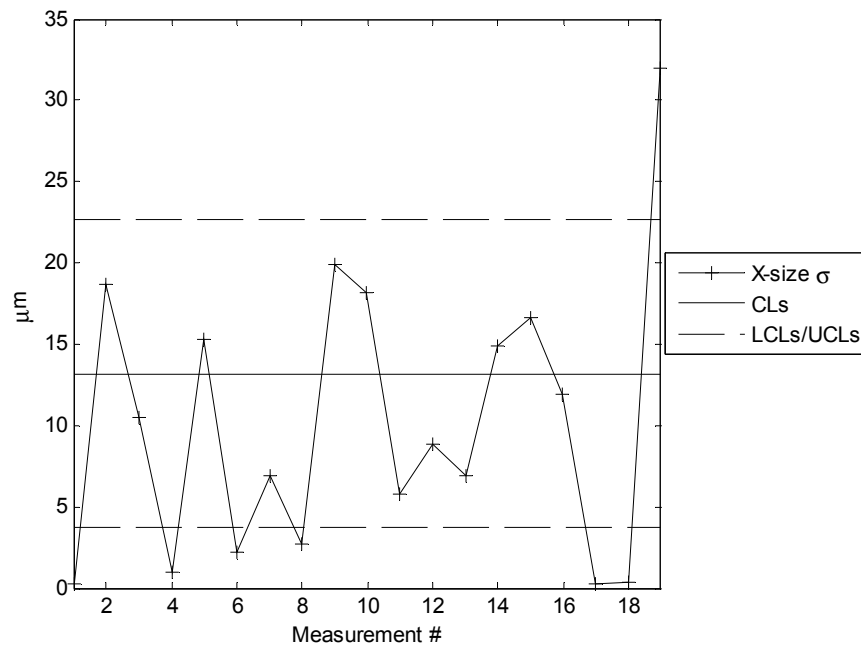


Figure 4.36: S chart for x-size of SLA part built in plus-x location

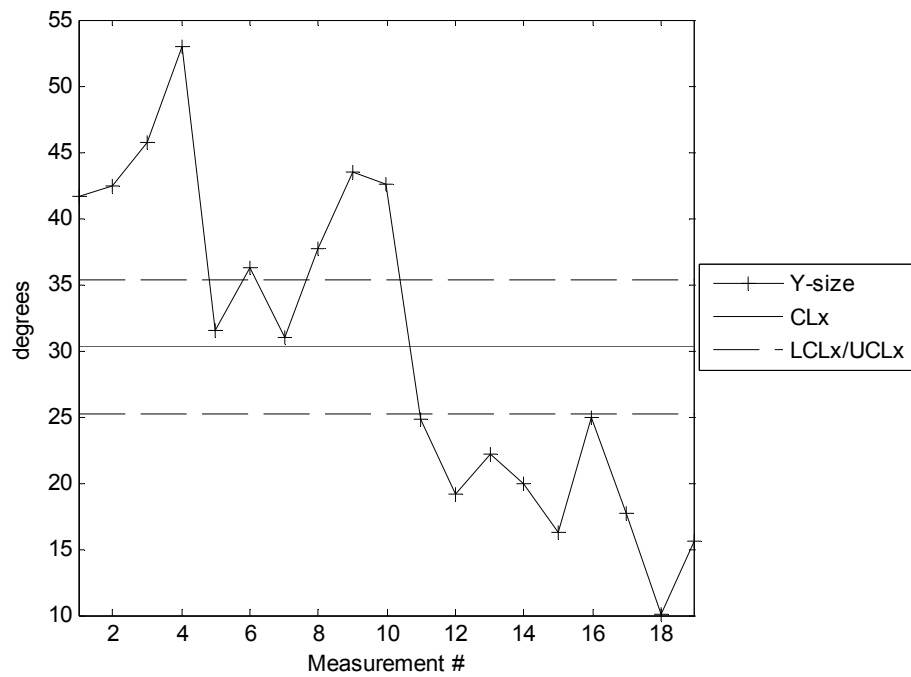


Figure 4.37: X-bar chart for y-size of SLA part built in plus-x location

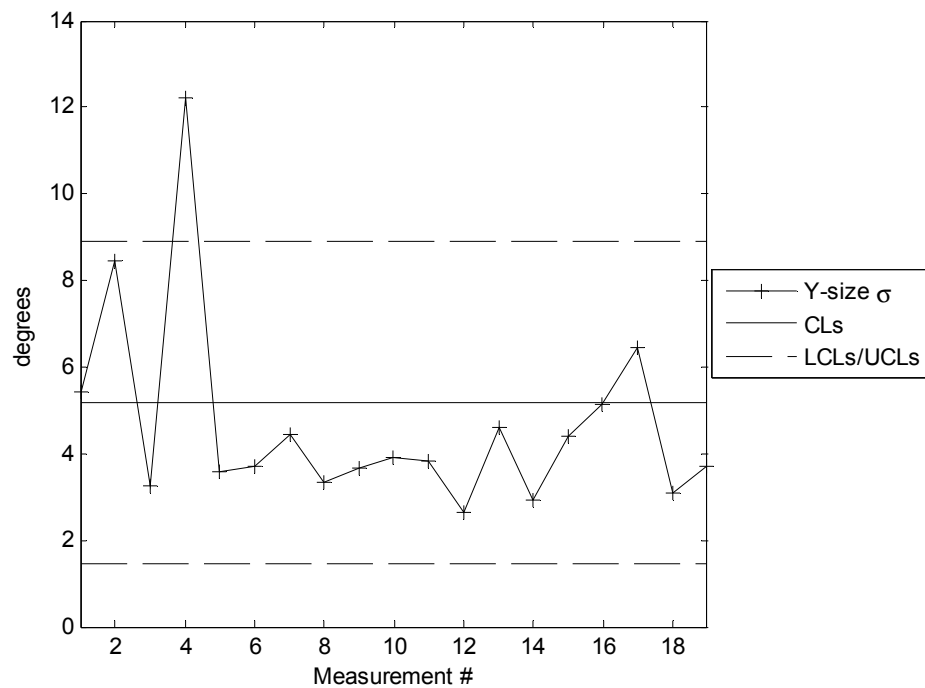


Figure 4.38: S chart for y-size of SLA part built in plus-x location

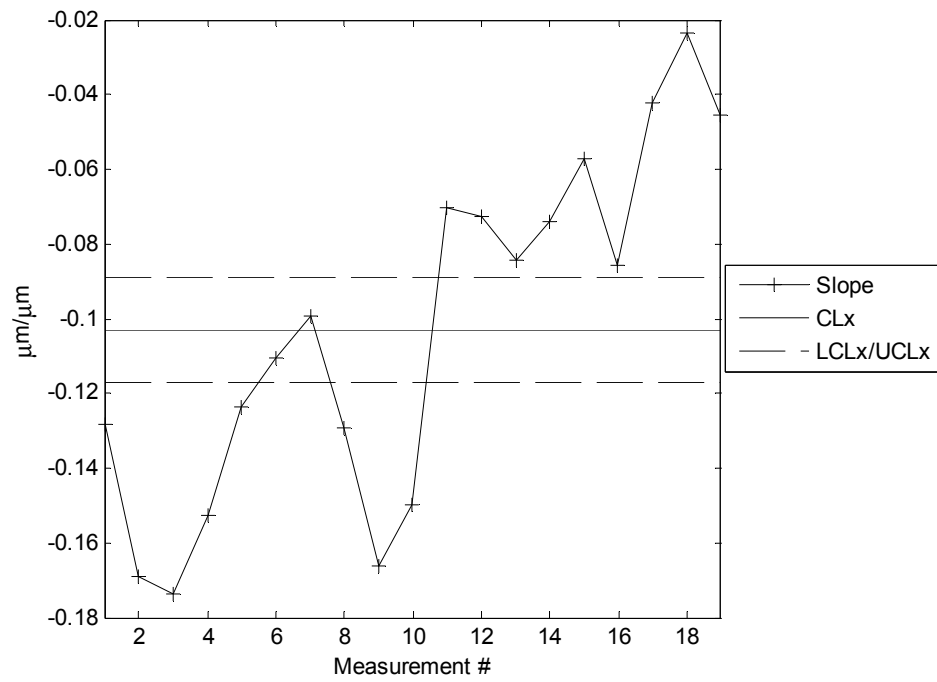


Figure 4.39: X-bar chart for slope of SLA part built in plus-x location

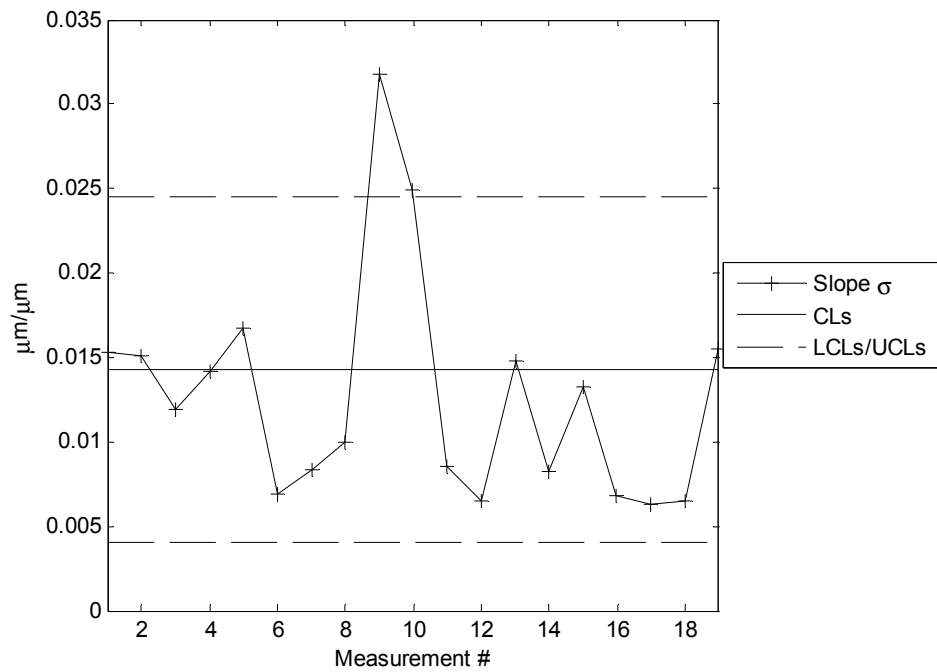


Figure 4.40: S chart for slope of SLA part built in plus-x location

It appears that the best-fit shape of the edge may be related to y-size. Inspection of data reveals that increased y-size can often be a result of a few measured points, as shown in the difference between Figure 4.41(b) and Figure 4.41(a). It is not possible to determine whether these points lie on the edge of the part due to the lack of data from the top. They are included in all calculations and have a direct impact on best-fit edge shape because the points have large deviations from a best-fit line causing an increase in the line residual.

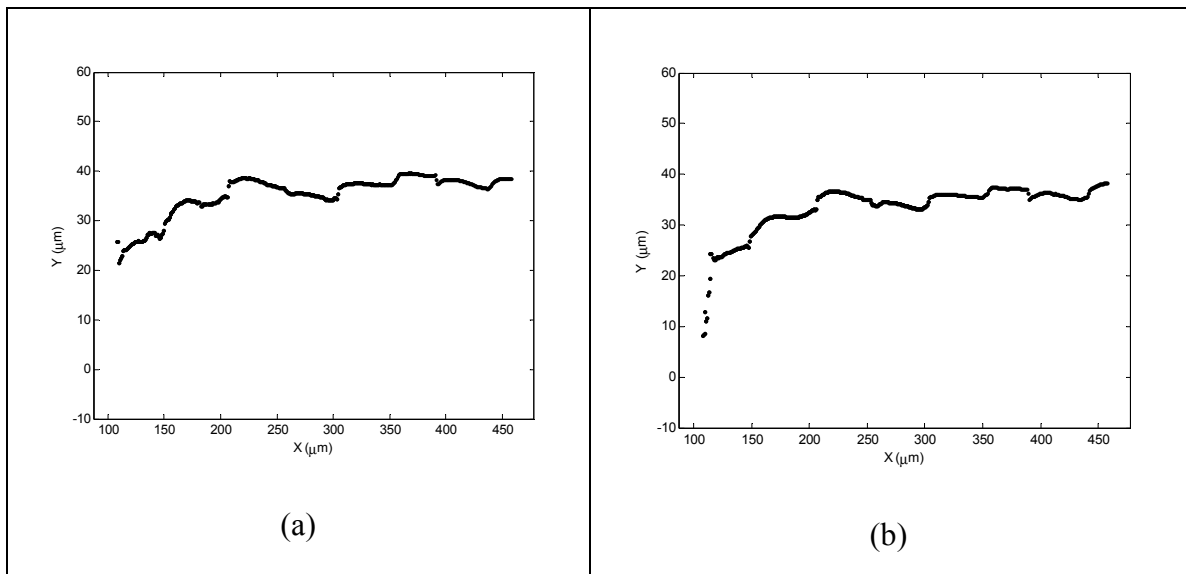


Figure 4.41: Data representative of change in y-size

Additionally, two major trends are noticeable between the two sides (slices 1-10 and slices 11-19) in the X-bar charts; the y-size, or height of the edge, is larger and the slope is smaller. The slope is highly dependent on the x and y size of the edge, thus the trends in the y-size and slope are related. As the y-size increases, shown in Figure 4.37, the slope becomes more pronounced, making a negative slope more negative, which can be seen in Figure 4.39.

Because the side surface, the edge, and the top surface could not be measured in the same scan, it is not clear whether the trends present in the data are a result of a change in edge size or a change in the amount of edge measured. Results from the part produced in the minus-x location may lend insight into the cause of the change in edge height.

Minus-X

The second part, made in the minus-x location, was measured in six locations, evenly spaced across the two long sides of the top edge (3 per side). Each measurement is made with the 20x objective, resulting in a point spacing of 0.90 μm , covering an approximate area of 460 by 460 μm . The axial point spacing is 2 μm .

The measurement data are processed in the same manner as the data for the part produced in the plus-x location. For all measurements of minus-x edges, a line fit the data better than the circle. Again, in several cases the residuals from the parabola fit were lower than those from the line, but because the vertex was not within range of the edge data the parabola is not useful for comparison.

Table 6: Best-fit shape of measurement area for SLA part built in plus-x location

Measurement Area	Best-Fit Shape
1	Line
2	Line
3	Line
4	Line
5	Line
6	Line

To aid in understanding the results from the study of the part produced in the plus-x location, X-bar charts are created for x-size, y-size, and slope for measurements of the part made in the minus-x location. These charts are presented as Figure 4.42, Figure 4.43, and Figure 4.44.

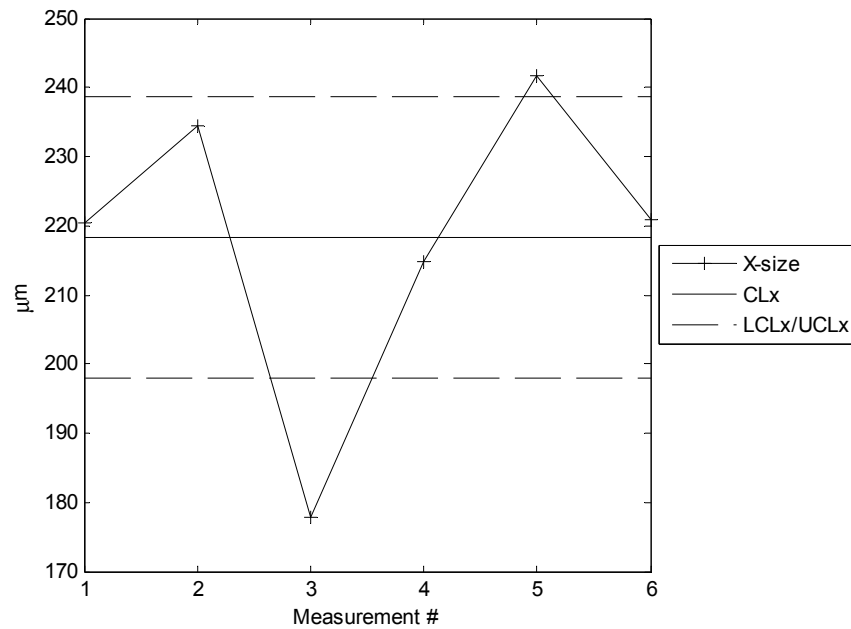


Figure 4.42: X-bar chart for x-size of SLA part built in minus-x location

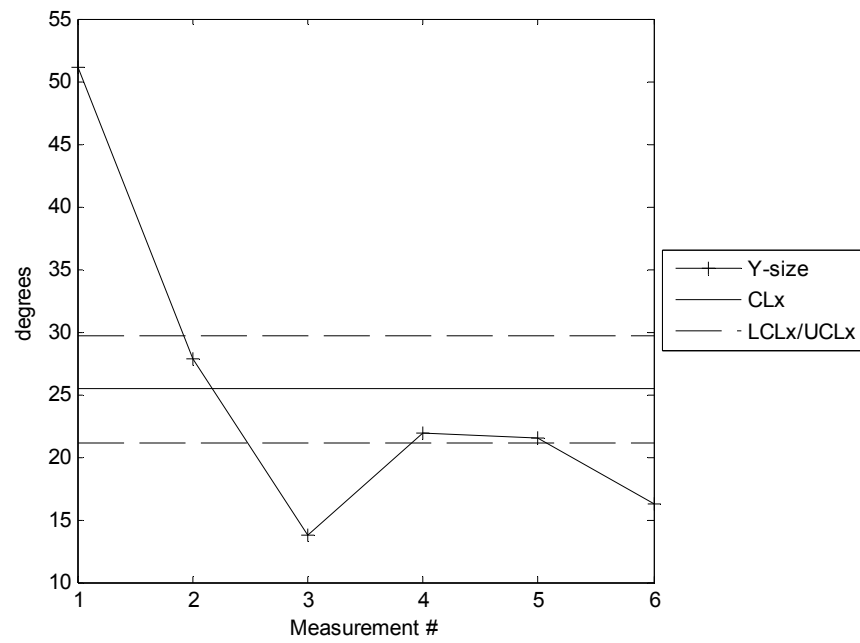


Figure 4.43: X-bar chart for y-size of SLA part built in minus-x location

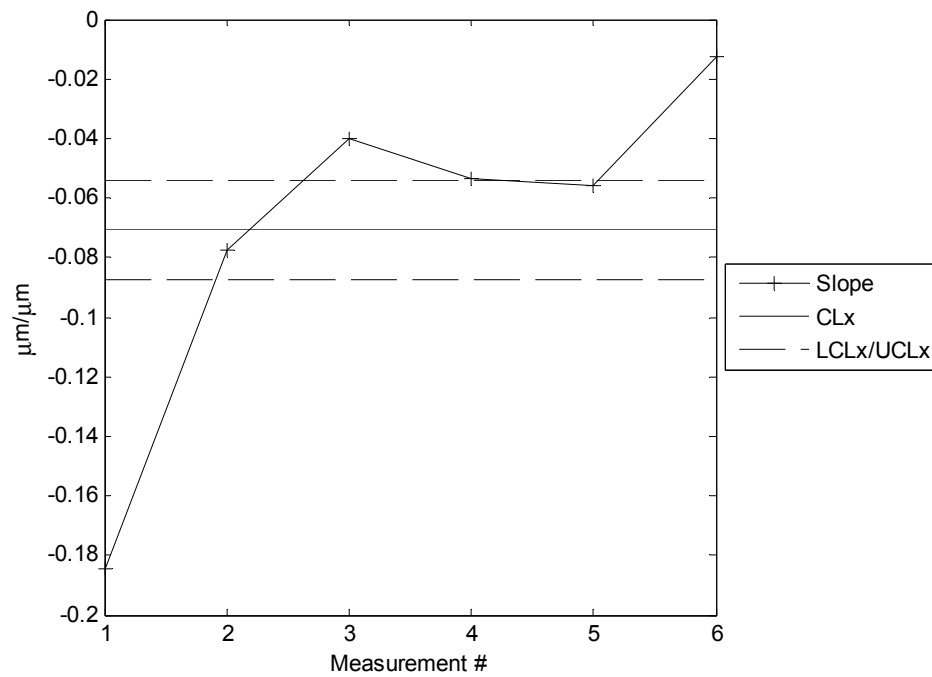


Figure 4.44: X-bar chart for slope of SLA part built in minus-x location

The results from the part produced in the minus-x location show trends similar to those of the part produced in the plus-x location. On average, the y-size is smaller on the second side and the slope is larger. However, because of the limited number of measurements and the limited number of measured parts, it is difficult to ensure that this trend is a result of processing conditions. Additional parts must be produced and measured to confirm and quantify this interaction.

SUMMARY

Parts made by three processes were measured using the CLSM. Analysis methods developed in Chapter 3 were used to analyze the collected data. Edges of two cutting tool inserts, one with a chamfered edge and one with a honed edge, were measured. The data are analyzed for edge shape and size, to locate burrs, and to detect trends. The analysis techniques are successful at analyzing the desired characteristics of the chamfered tool. Although the size and shape of the honed tool were successfully analyzed, the analysis tools are not able to analyze trends present due to poor data condition. LIGA edges are not characterized because of insufficient CLSM resolution. SLA edges are found to have a nominally linear shape and may be dependent on build location.

CHAPTER 5: EDGE SPECIFICATION

It is important that the edge of the mesoscale part be defined in design as it is in traditional manufacturing. It is possible to measure and characterize the edge, but in order for the characterization to be useful, the designer must specify edge requirements. This is especially critical because the edges frequently constitute a large percentage of the feature size, therefore the edge size, shape, and condition may have a large impact on the function/life of the component.

Edge finishing, including burr-removal, is a well-defined area of research. For a variety of reasons discussed in Chapter 1 burrs are almost universally undesirable and are eliminated or minimized to meet specifications. Several edge specification and characterization methods have been developed to ensure that the edge condition of the final part meets design requirements. In these characterization methods, two quantities are of particular importance; edge sharpness and edge condition (i.e., extent of burr removal)

EXISTING BURR AND EDGE CLASSIFICATION

Burrs and their properties are a function of material properties, manufacturing processes, and part configuration [4]. Although there are methods to remove burrs of all sizes, small burrs are particularly easy to remove. Because cost reduction is a primary concern, it is desirable to prevent or minimize the size of burrs. The manufacturing process, part geometry and workpiece material are often adjusted to prevent or minimize the size of produced burrs. Analyzing and predicting burr formation is consequently a large field of study. Dornfeld [96] provides a collection of papers on this subject.

Burr Types

Chern [97; 98] observed four types of burrs created by variations in depth of cut and in-plane exit angle in face-milling operations; knife, curl, wave and edge breakout. Burrs are characterized by type, height, and thickness, measured as shown in Figure 5.1.

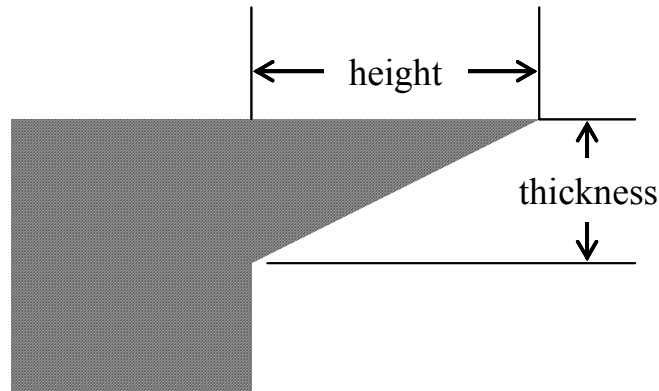


Figure 5.1: Burr size characteristics [97; 98]

Schafer's Burr Classification

In the 1970's Schafer [99] proposed a classification scheme for burrs to provide qualitative information on deburring quality. Similar to the characterization method presented in this work, the edge of the part was considered as a series of 2D slices, with burr characteristics being reported independently for each slice. For Schafer's scheme, characteristic properties for burrs are, F_k – edge radius, h_l - residual burr height, and b_k – missing edge width (radius or chamfer).

The classification method divides the edge into four quadrants formed by the intersecting top and side surfaces, as shown by the dotted lines in Figure 5.2. Each quadrant is assigned a class (1-9) corresponding to the amount of excess material present, or the amount of material missing. Several examples of edges with their quadrant-based classification are given in Figure 5.3.

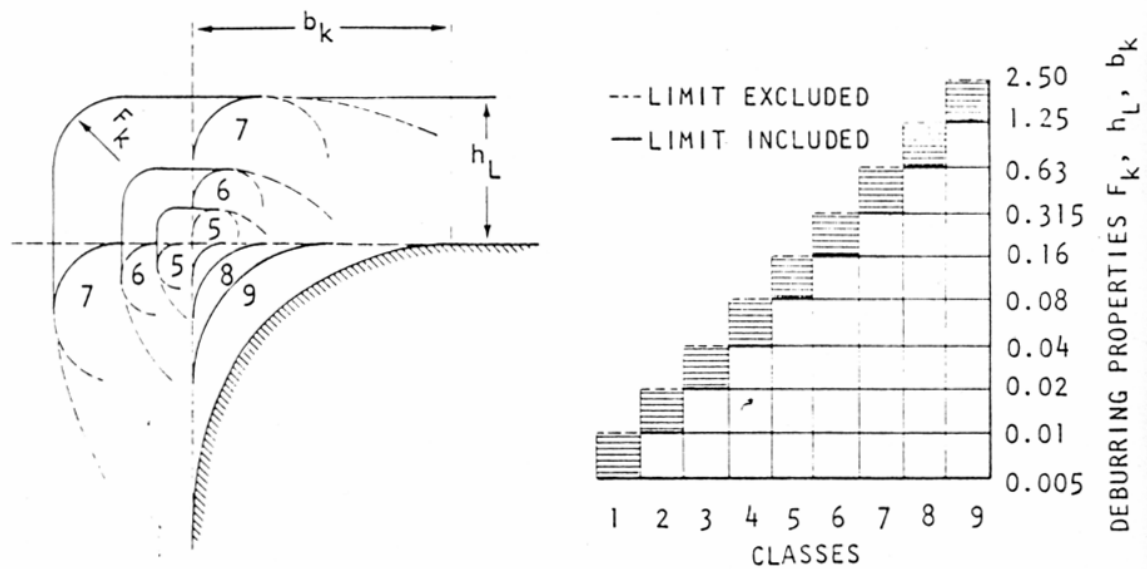


Figure 5.2: Quadrant-based classification scheme and corresponding classes of allowable edge quality proposed by Schafer [100]

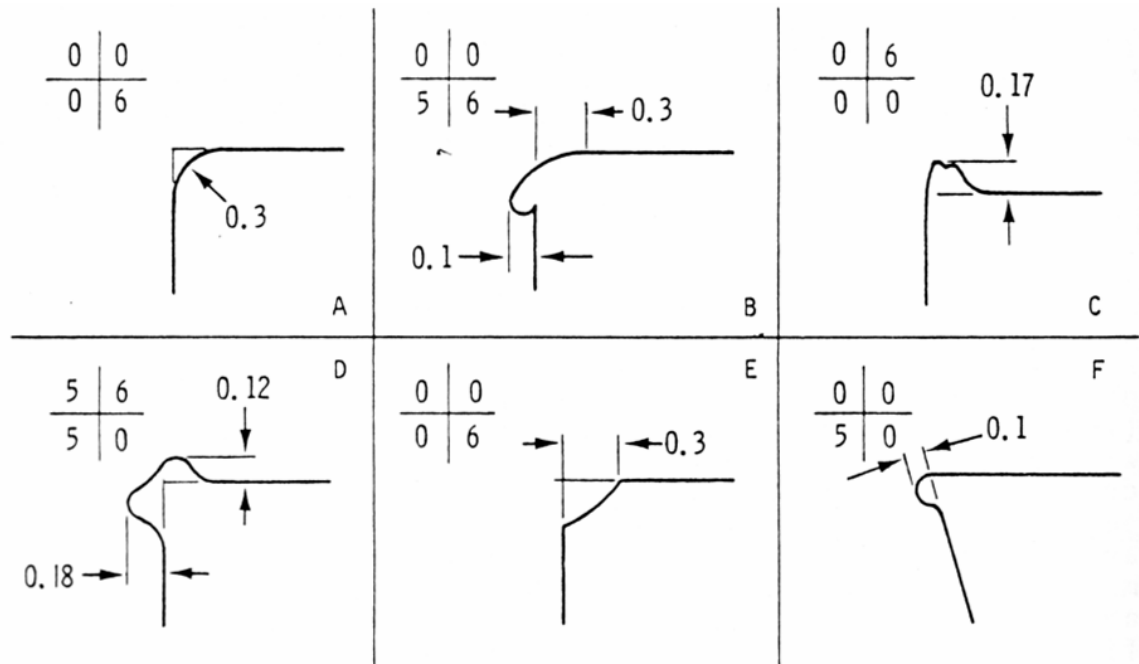


Figure 5.3: Classified edge conditions [100]

In Schafer's study, part edges were measured using a silicon microsectioning technique where the workpiece edge was cast in silicon caoutchouc [101]. After the

silicon hardened, the workpiece was removed. The silicon rubber cast was cut into thin slices, each considered independently. This measurement method is time consuming and suitable only for investigational purposes.

Gillespie's Edge Quality Classification Scheme

Gillespie proposed a national standard for specifying burrs and deburring in design [102]. Seven levels of edge quality, A to G, are specified and described below.

- A. Deburring is not required
- B. Remove sharp edges
- C. Remove all visible burrs
- D. Remove all burrs visible at ____X magnification
- E. Break edges at ____ x ____ mm minimum
- F. Round edges ____ to ____ mm. radius
- G. Do not deburr

Levels A to D are self-explanatory. Level E allows an edge that exists within a minimum chamfer line. The x and y chamfer dimensions are specified as shown in Figure 5.4. The edge does not necessarily have a chamfered shape, and not all burrs must be removed. Small burrs may exist on the edges of the chamfers, so long as the material does not fall beyond the product dimensions.

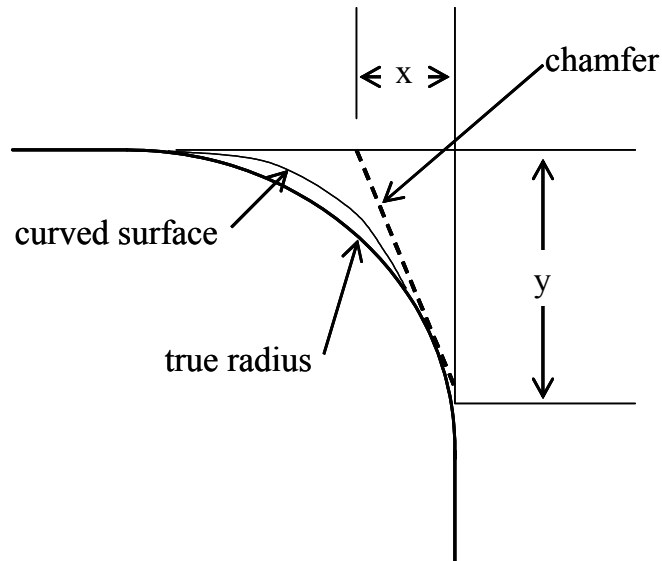


Figure 5.4: Allowable edge conditions with Level E, "Break edges ___ to ___ mm minimum" [102]

Level F specifies that allowable edge conditions must have a smooth curved shape. Although this shape is not required to be a true radius, the curvature must fall between the indicated limits as shown in Figure 5.5. Additionally, the edge must fall within part dimensions. Figure 5.6 illustrates an instance where the curvature of the radius is acceptable ($R3 > R1 > R2$), but because the edge is beyond the part dimensions, the edge condition is not allowable by these standards.

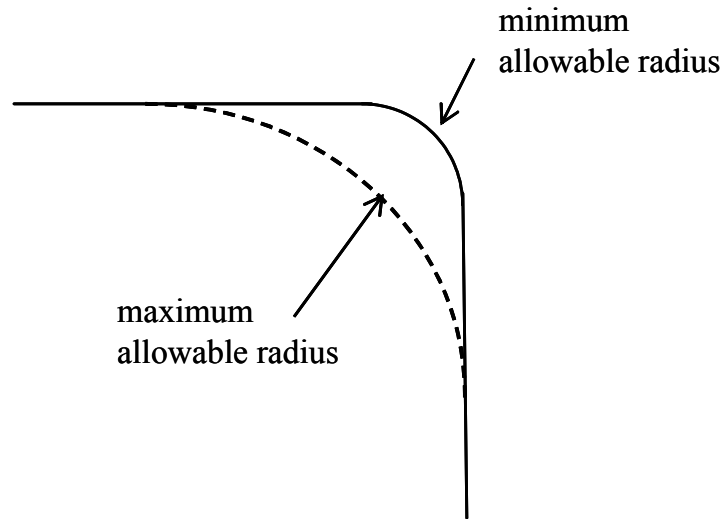


Figure 5.5: Allowable edge conditions with Level F, "Round edges ____ to ____ mm radius" [102]

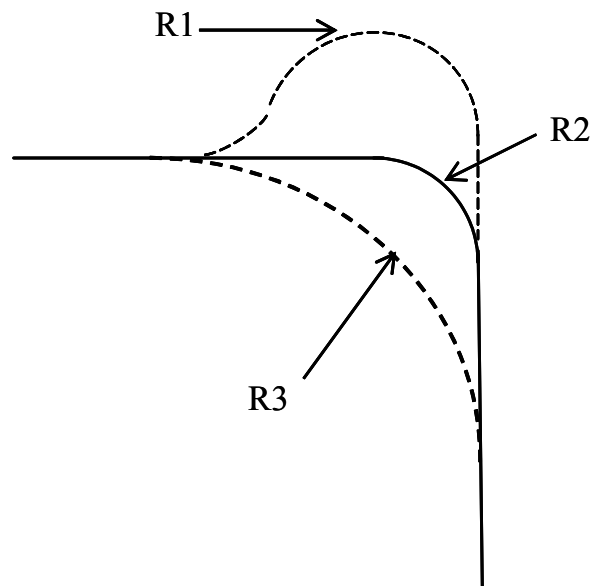


Figure 5.6: Edge condition not allowed by Level F, "Round edges ____ to ____ mm radius" [102]

Takazawa's Edge Quality Classes

In addition to Gillespie, Takazawa [4; 103] has created a set of edge quality classes. The specification of these classes is similar to previous system with the addition

of specific dimensions and evaluation techniques. With edge sizes from about 1 to 200 μm , mesoscale edges as defined for this thesis fall within the E0 and E1 classes. The E1 class has a radius of 20 μm and a tolerance of 0.3 to 5 μm . The E1 class has a radius of 2 μm with a tolerance of 0.01 to 0.02 μm . While the measured edges from the case studies presented fall within the drawing definition of these classes, the radius tolerance is an order of magnitude higher than the observed size variations.

Table 7: Overview of edge quality requirements [4; 103]

Class	Grade	Drawing Definition	Radius Tolerance	Qualitative Evaluation	Quantitative Evaluation	Typical Application
E0	Exceptional high-quality edge	0.0002R	0.01-0.02 μm		Interference microscope, SEM	Diamond microtome knife edge
E1	High-quality edge	0.002R	0.3–5 μm	Cuts paper	Universal tool microscope, profilometer, light section	Edge of cutting tools, edge of dies
E2	Sharp edge	0.02R	8–30 μm	Cuts fingernail	Universal tool microscope, profilometer, light section	Hydraulic orifice edge
E3	Rounded edge	0.2R or chamfer	0.08-0.3 mm	Will not cut finger	Stereo microscope Replica Measurements	Mechanical parts, gyro pivots, piston rings, hydraulic spools
E4	Chamfered edge	0.5R or chamfer	0.4-0.6 mm	Naked eye, magnifying glass	Optical comparator	Mechanical parts
E5	Dull edge			No cut fingers	UL sharpness gage	Some automotive parts

In addition to providing a class-system for edge quality, the table also offers a sense of the evaluation techniques used in industry. The qualitative techniques are seemingly primitive, but are commonly used to determine edge quality. Gillespie [4] outlines these techniques and others as part of a sample plant standard for inspection.

MESOSCALE EDGE SPECIFICATION

Edges of mesoscale structures can be relatively large compared to their smallest feature size, yet they are not often specified in design. In order to specify edges in design, a method for communication of desired and/or acceptable edge conditions is needed. Although the edge quality standards and classification schemes presented earlier in this chapter were not developed for mesoscale parts, they provide a well-tested starting point for development of a mesoscale edge specification system.

Components

There exist several classification schemes for edges of traditionally manufactured parts, but the majority of these methods were developed with elimination of burrs in mind. Burrs, although still a concern in the mesoscale, are only one of several critical considerations for edges. In addition to specifying of the acceptability of burrs, it is necessary to understand desired profile as well as size and shape limitations. Accordingly, the proposed classification scheme requires specification of three components – edge size, edge shape and edge condition. It is assumed that any material present outside the theoretical intersection of the top and side surfaces is unacceptable.

Size

The first, and most important, distinction between mesoscale edge classification and traditional edge classification is that the size of the edge is not simply a matter of sharpness. Because of the small feature sizes present in mesoscale objects, the edges, even if extremely sharp by traditional standards, may constitute a large percentage of total size and have an effect on performance. Thus it is necessary to specify both the minimum and maximum allowable size for the edge in both the x and y directions.

$$\begin{aligned} MAXIMUM &= \frac{\quad}{(x)} \quad by \quad \frac{\quad}{(y)} \\ MINIMUM &= \frac{\quad}{(x)} \quad by \quad \frac{\quad}{(y)} \end{aligned}$$

A line drawn from the minimum x value to the minimum y-value delineates the outside boundary for the edge. A line drawn from the maximum x value to the maximum y-value delineates the inside boundary for the edge. The inside and outside boundaries are depicted in Figure 5.7. The entire edge must fall between the inside and outside boundaries.

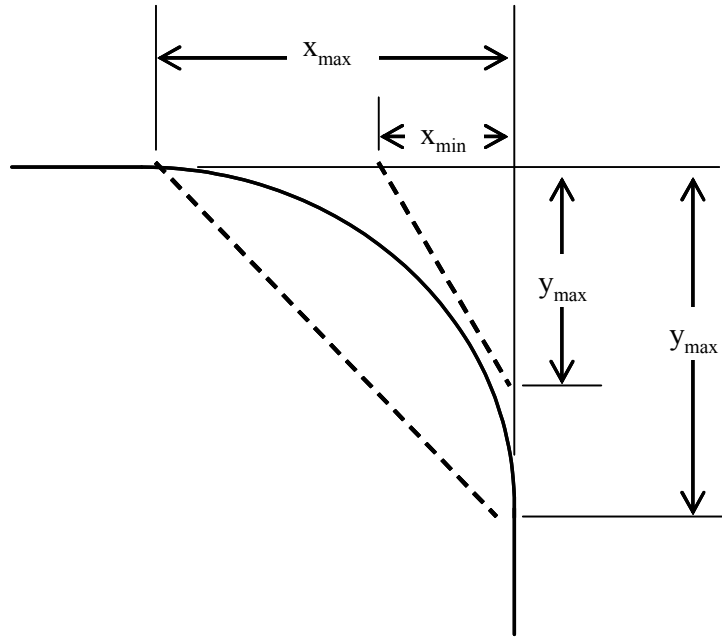


Figure 5.7: Edge size representation

Shape

In addition to edge size, it is necessary to specify the desired nominal shape of the edge. In this specification plan, three edge shapes are available; curved (R), chamfered (C), and undefined (U). Representations of these three types of edges are presented in Figure 5.8.

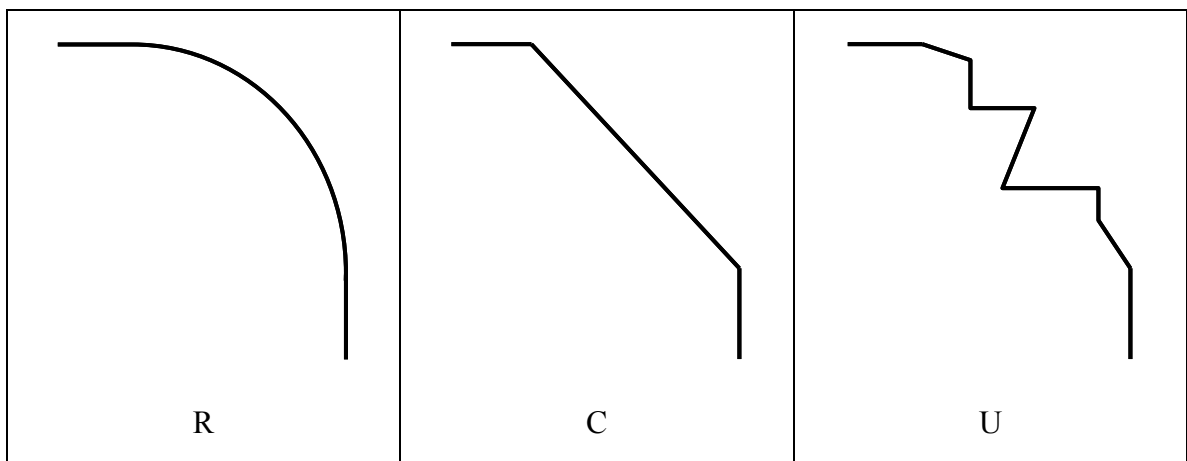


Figure 5.8: Example edge shapes for curved (R), chamfered (C), and undefined (U) edges

The curved edge, R, can represent an edge with a circular radius, or other curved shape, as long as the curve is continuous (i.e., contains no inflection points). A chamfered edge, C, has a nominally straight shape. An undefined edge, U, can take any shape, including curved or chamfered, continuous or non-continuous, so long as the entire edge lies between the defined maximum and minimum size. All example edge shapes in Figure 5.8, are acceptable shapes for an undefined edge.

Edge Condition

Edge condition is directly related to burrs and other protrusions that exist on the part edge. Burrs can create problems in mesoscale systems even if they do not exist outside the specified size limits. If a burr remains attached to the part it can cause interference in assembly, disrupted fluid flow, and changes in heat transfer levels due to increased surface area. If a burr breaks off it has the potential to contaminate the system or create a stress concentration leading to premature part failure.

Two burr removal levels are available in this specification methodology; burrs are acceptable below a specified size, and all burrs are acceptable. Both levels assume that no material extends past the two planes that define the top and the side of the object under consideration. For an undefined edge, the second removal level, all burrs are acceptable, is required. Because the edge is undefined, there is no way to determine whether a protrusion should be considered a burr or a part of the edge shape.

If there is a limit to the size of acceptable burrs, it is necessary to designate a burr measurement metric to provide consistency in application. Chern evaluates burrs of machined parts by determining the height and size, as shown in Figure 5.1. Schafer [101] considers the 2D area of the burr. Burrs can also be quantified by volume or attachment

area. The quantification method must be chosen to reflect the application and the concerns associated with small protrusions. For example, an application where the chief concern is contamination caused by removed burrs may use attachment area as a quantification method.

Discussion

Having an edge specification method that is process independent has both positive and negative aspects. A standard method can be applied universally so a new specification method does not need to be developed for each individual process. Also, if edge condition requirements are related to part function there is no need to translate between specification methods for various processes. However, a process-independent specification method does not allow specific processing factors to be considered.

SUMMARY

In this chapter, a specification methodology was developed that provides a standardized method for specification of desired final edge conditions for mesoscale objects. This methodology includes specification of three quantities – size, shape, and edge quality. The specification system builds on burr and edge classification schemes developed for traditionally manufactured objects.

CHAPTER 6: CONCLUSIONS

SUMMARY

This thesis provides a methodology for the consideration of mesoscale edges. This methodology includes three major components; measurement, characterization, and specification.

In order to provide recommendations for tools to collect edge data from mesoscale parts, current mesoscale measurement methods are analyzed. Of greatest importance in recommending an edge measurement tool is the ability of the tool to non-destructively measure an object containing a range of angles at sufficient resolution. Due to the wide range of materials and size, no single tool can be recommended to collect edge data. Three tools, the atomic force microscope (AFM), the confocal laser scanning microscope (CLSM), and the profilometer are recommended as edge measurement techniques. The CLSM is chosen as the data collection tool for this thesis because it has properties suitable for measurement of the widest range of mesoscale parts. The CLSM was able to capture data from all parts, although the data is not always adequate for edge characterization due to noise and insufficient resolution.

In order to analyze the collected data, analysis methods are developed to characterize shape and size, locate local inconsistencies such as burrs, and reveal global trends. Size is calculated directly by the algorithm to separate edge data from top and side data. Shape is determined by fitting circles, lines, parabolas or a combination of the three to edge data. The tracking of changes in best-fit parameters, residuals, and size over a single measurement area is used to locate local inconsistencies such as burrs.

Analysis techniques derived from statistical process control are applied over measurements from the entire part to identify global trends.

The analysis tools developed for characterization are applied to several case studies which contain edges of both known and unknown shape. Each case study uses a different combination of analysis tools to create a characterization scheme specific to the edge being inspected. Two cutting tool inserts, one with a chamfered edge and one with a honed edge are studied. Local inconsistencies and global changes are successfully identified using the described characterization for the chamfered edge tool. Although local problems are indicated, data collected from the honed tool are not sufficient for global inspection due to high noise levels. LIGA measurement data present another problem; the edges present in the measured part cannot be distinguished from data collected on the top and the side due to insufficient CLSM resolution. A final case study of edges from parts produced by SLA shows that the top edge is best characterized by a line. Additional studies of SLA edges are needed to determine the effect of build position on edge shape and size.

In order to understand the acceptability of produced edges, it is necessary to consider and communicate edge requirements as part of the design. A mesoscale edge specification method is developed based on burr classification techniques, with considerations specific to mesoscale in mind. The specification method requires statement of the maximum and minimum edge size, the desired edge shape, and the edge condition (i.e., burrs are not acceptable).

CONCLUSIONS

It is possible to measure mesoscale edges. The CLSM is shown to have the ability to measure edges of various sizes made from different materials. However, the quality of the measured data varies from edge to edge. It is necessary to establish a metric for determining the quality of the measured data.

Characterization methods are highly dependent on the quality of measured data. The characterization techniques developed in this thesis are able to calculate shape and size, locate burrs, and track trends. These techniques were shown to work well for high-quality data, but did not perform as well for lower-quality or incomplete data.

The processes that create mesoscale edges do not produce consistent edges. Good control of edge shape and size is desirable because it shows understanding of process parameters and allows for less testing because of higher predictability. Often, when performing initial analysis of a process, as is the case in the presented studies, the process lacks control. These initial data can be used to improve the process by finding assignable causes of variation and removing those that are undesirable.

It is necessary for desired edge conditions to be specified in design. Undefined edge geometry can result in measurement, assembly, and operational difficulties. It is important to specify the limits of acceptable size, the desired shape, and required edge quality so that an edge with the potential to cause problems can be identified.

CONTRIBUTIONS

Listed below are the five intellectual contributions of this work.

- The definition of the mesoscale edge measurement and characterization problem.

- The analysis of mesoscale measurement techniques in order to provide an edge measurement recommendation based on size and part properties. This includes the suggestion of a reference artifact to validate measurements.
- The development of a set of analysis methods to characterize edge shape and size, pinpoint local inaccuracies, and reveal global trends. This includes the development of edge separation and non-axis aligned parabola fitting algorithms. Individual analysis methods can be combined to create a strategy specific to the part and process.
- The completion of several case studies that use a recommended measurement method in combination with a characterization strategy specific to the part to understand edge size, shape, and condition.
- An edge specification method to communicate mesoscale design requirements.

FUTURE WORK

The work in this thesis is intended to be a starting point for mesoscale edge consideration. As a result there is a considerable amount of future work to be done in order to ensure that the processes used to create mesoscale edges are understood and capable of producing a well-controlled edge.

The first critical component to edge consideration is measurement. There are several avenues for future work in this area. First, a three dimensional mesoscale reference artifact needs to be developed to allow for measurement tool validation. To be

useful for validation of mesoscale edge measurement, this tool must contain a range of angles and be manufacturable in a variety of materials.

Second, a metric for quality of CLSM measurements would allow for determination of the quality of collected data. There are many CLSM parameters which can be adjusted and, with a metric, it would be possible to identify ideal measurement parameters specific to each edge. This would lead in higher quality data which would result in the ability to perform a more complete characterization of the edge. Additionally, tests are needed to check the repeatability of the system.

If capturing an entire edge with the CLSM is desired, a stitching method in combination with a fixture must be developed. Along the same lines, a stitching method can be developed for a series of measurements of the same object at different detector gain settings. This may allow for measurement of highly sloping reflective surfaces such as the small spheres discussed in Chapter 2.

The second critical component to edge consideration is characterization. This thesis developed a set of useful tools. Additional tools specific to a process may be developed and used in combination with those presented in Chapter 4 to consider other aspects of edge production and quality.

The tools developed can also be used to identify the effect of process parameters on final edge conditions for a specific process. The characterization tools are not limited to use on mesoscale edges and can be used on edges of all sizes. After the effects of process parameters are identified, and those parameters that negatively impact the edge condition removed, it may be possible to create a well-controlled edge.

The third critical component of edge consideration is specification. The edge specification method developed in this thesis is a starting point. Further refinement will be necessary as additional edge qualities are considered and edge specification, as a part of design, is adopted.

CONCLUDING REMARK

This thesis developed a strategy for the measurement, characterization and specification of mesoscale edges. The techniques presented can be used to understand a produced edge and can be extended to make process improvements with the goal of creating a well-controlled edge that meets design requirements.

APPENDIX A: CHAMFERED TOOL EDGE DATA

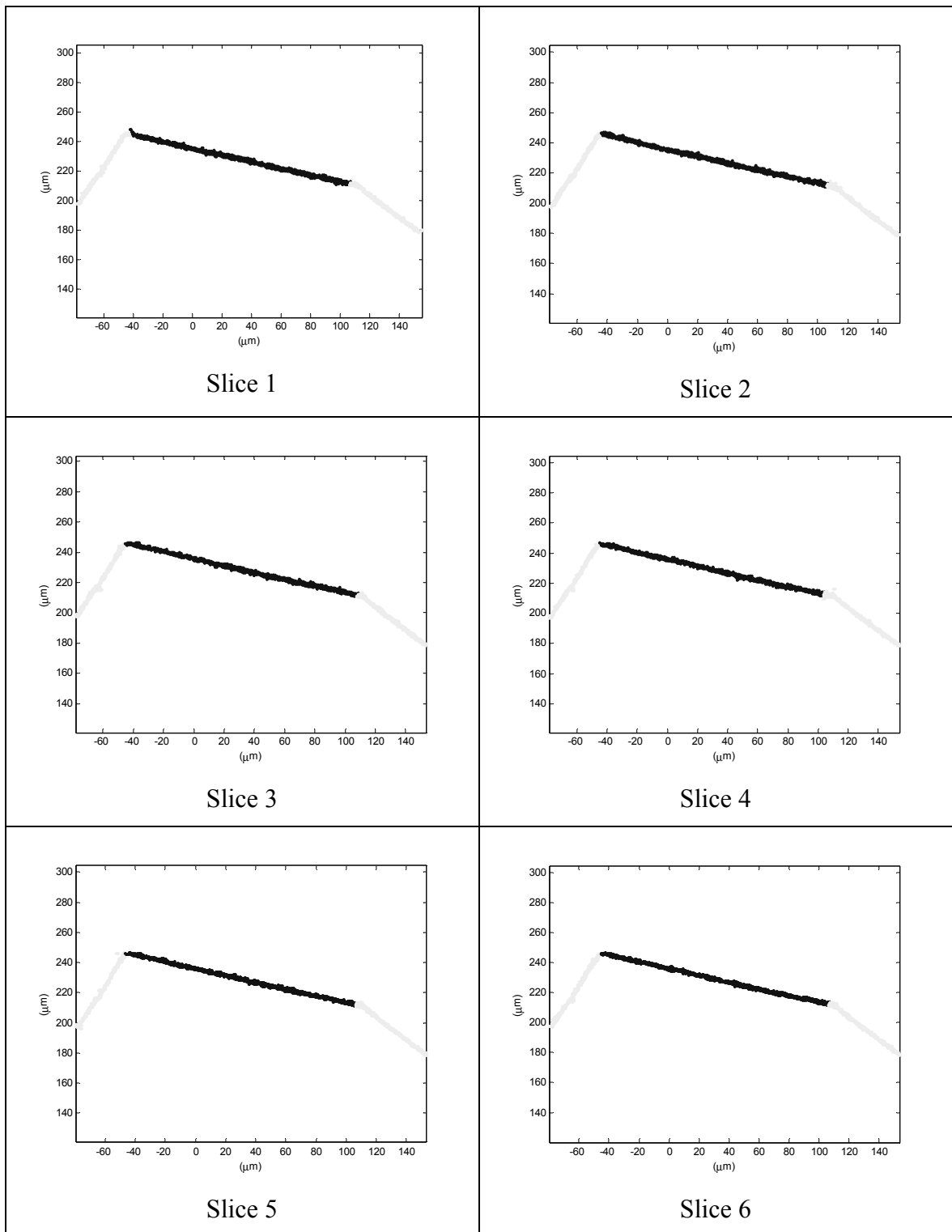


Figure A.1: Slices 1-6 for representative chamfer data

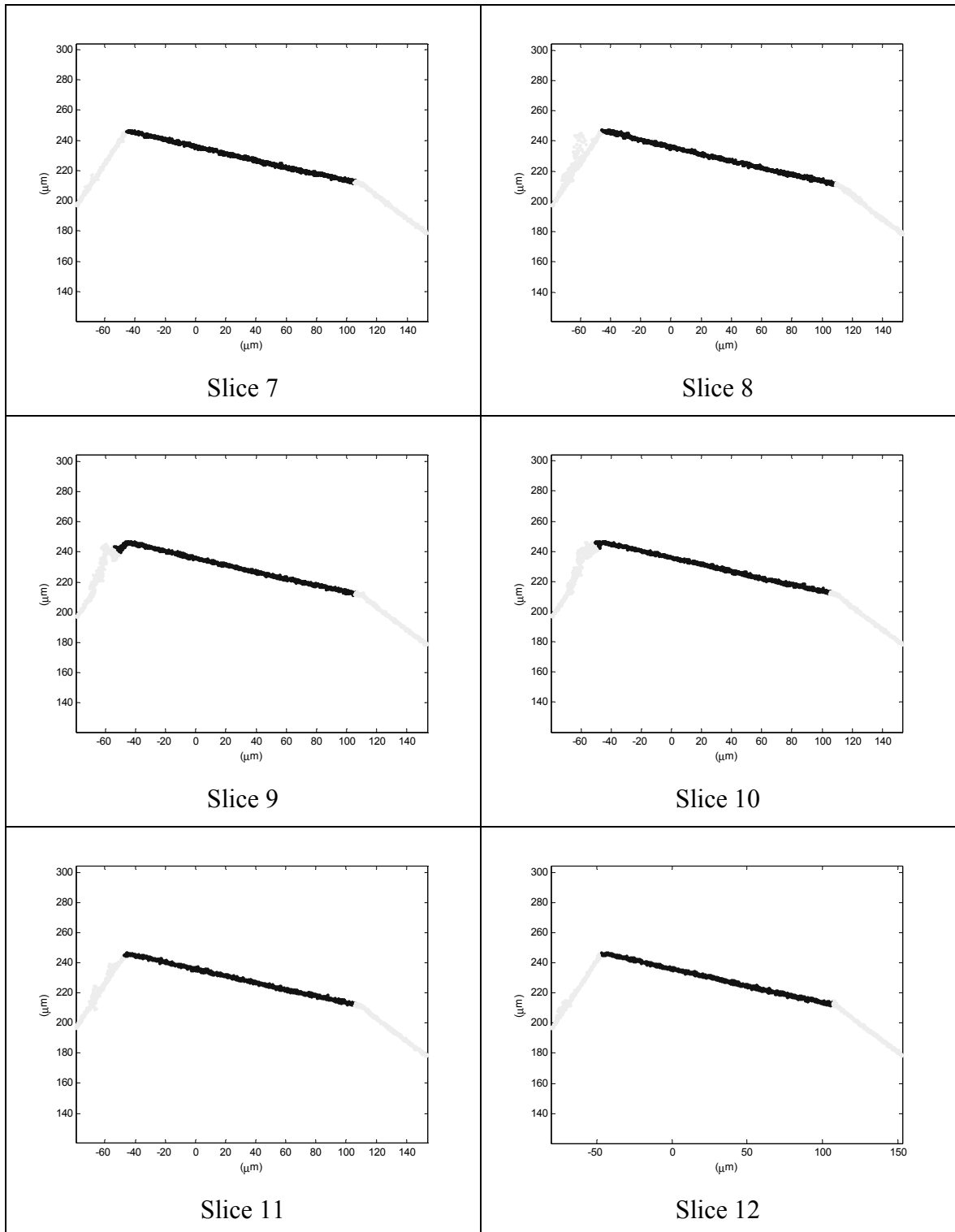


Figure A.2 Slices 7-12 for representative chamfer data

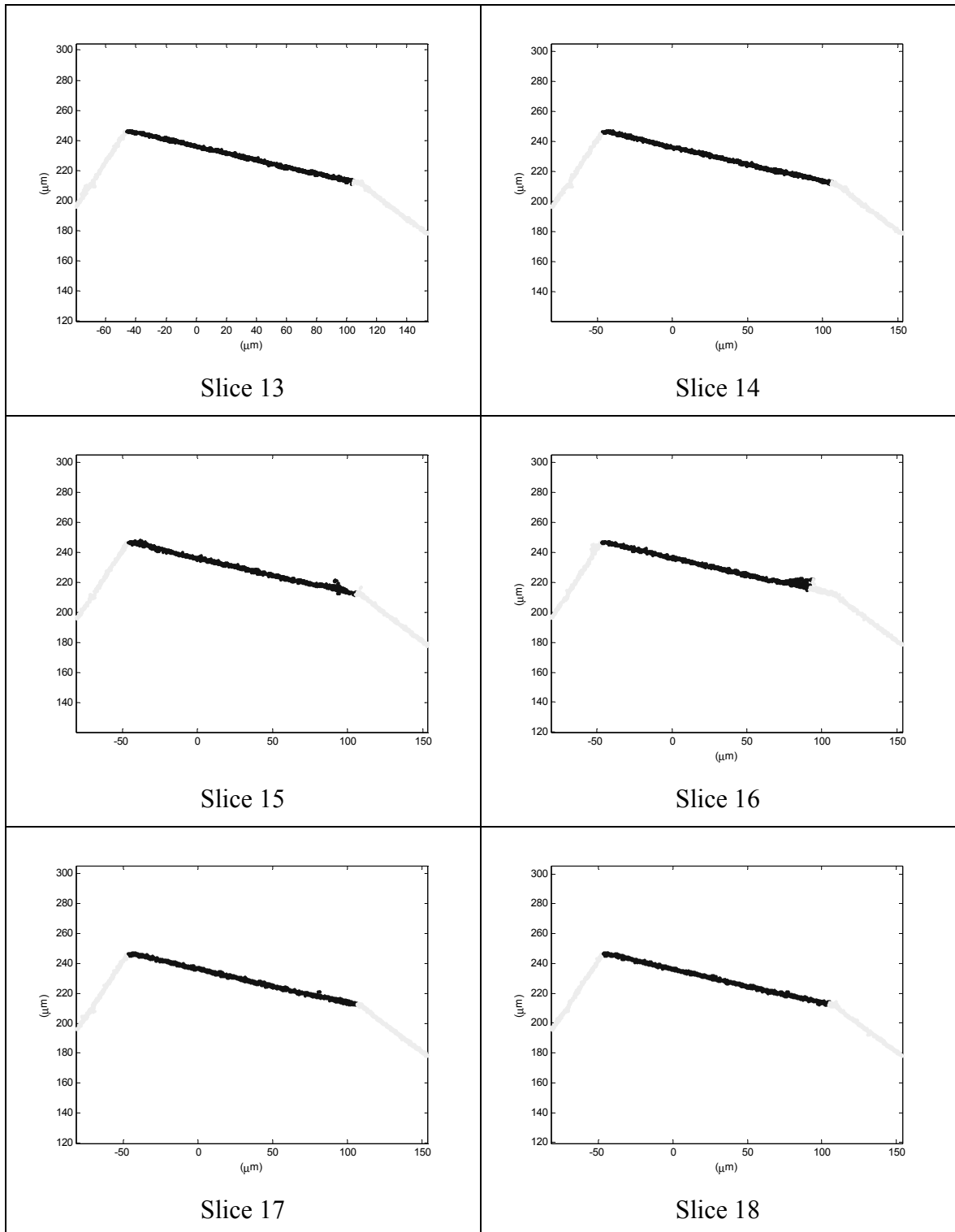


Figure A.3: Slices 13-18 for representative chamfer data

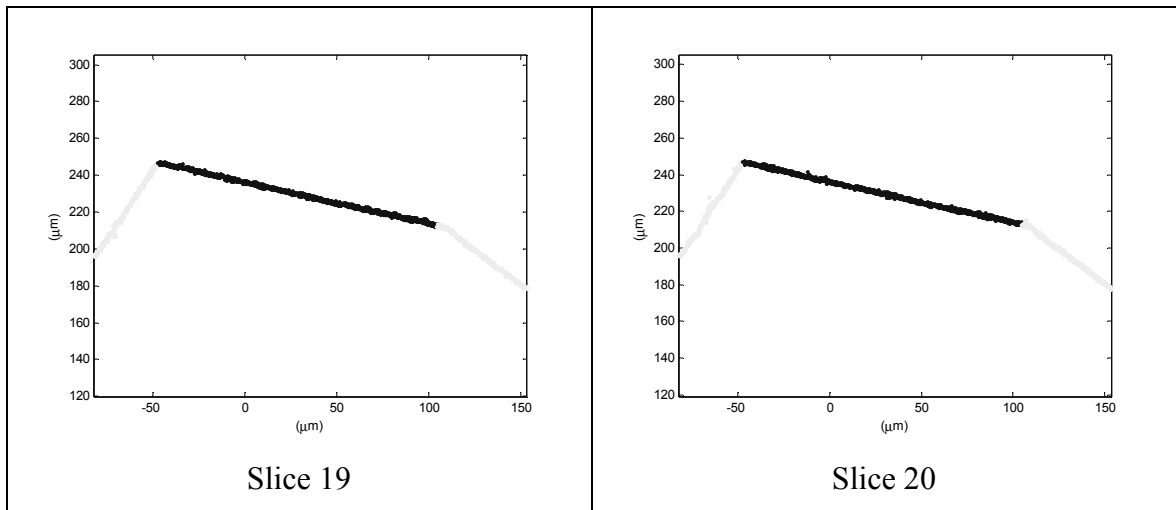


Figure A.4: Slices 19-20 for representative chamfer data

APPENDIX B: HONED TOOL EDGE DATA

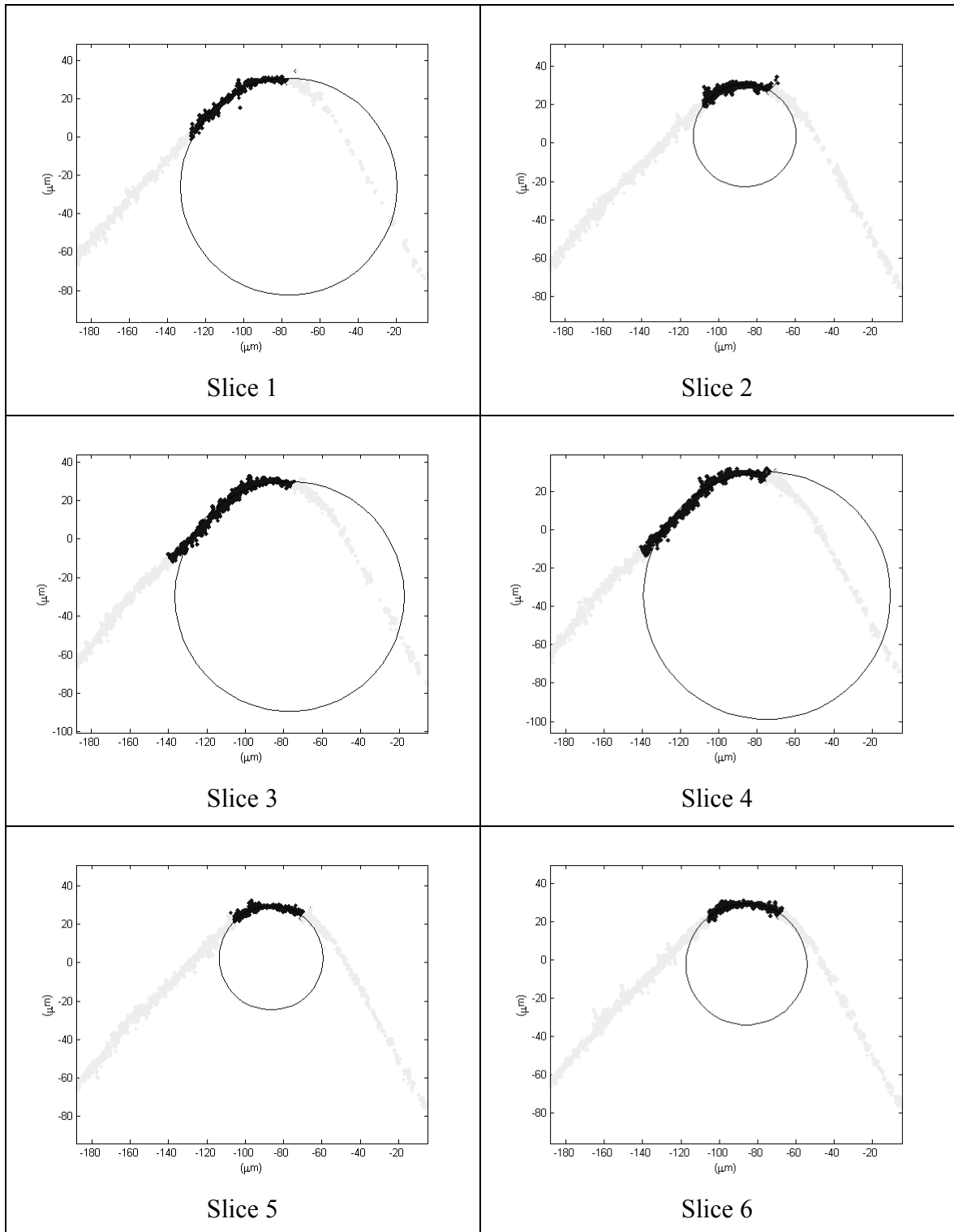


Figure B.1: Slices 1-6 for representative honed data

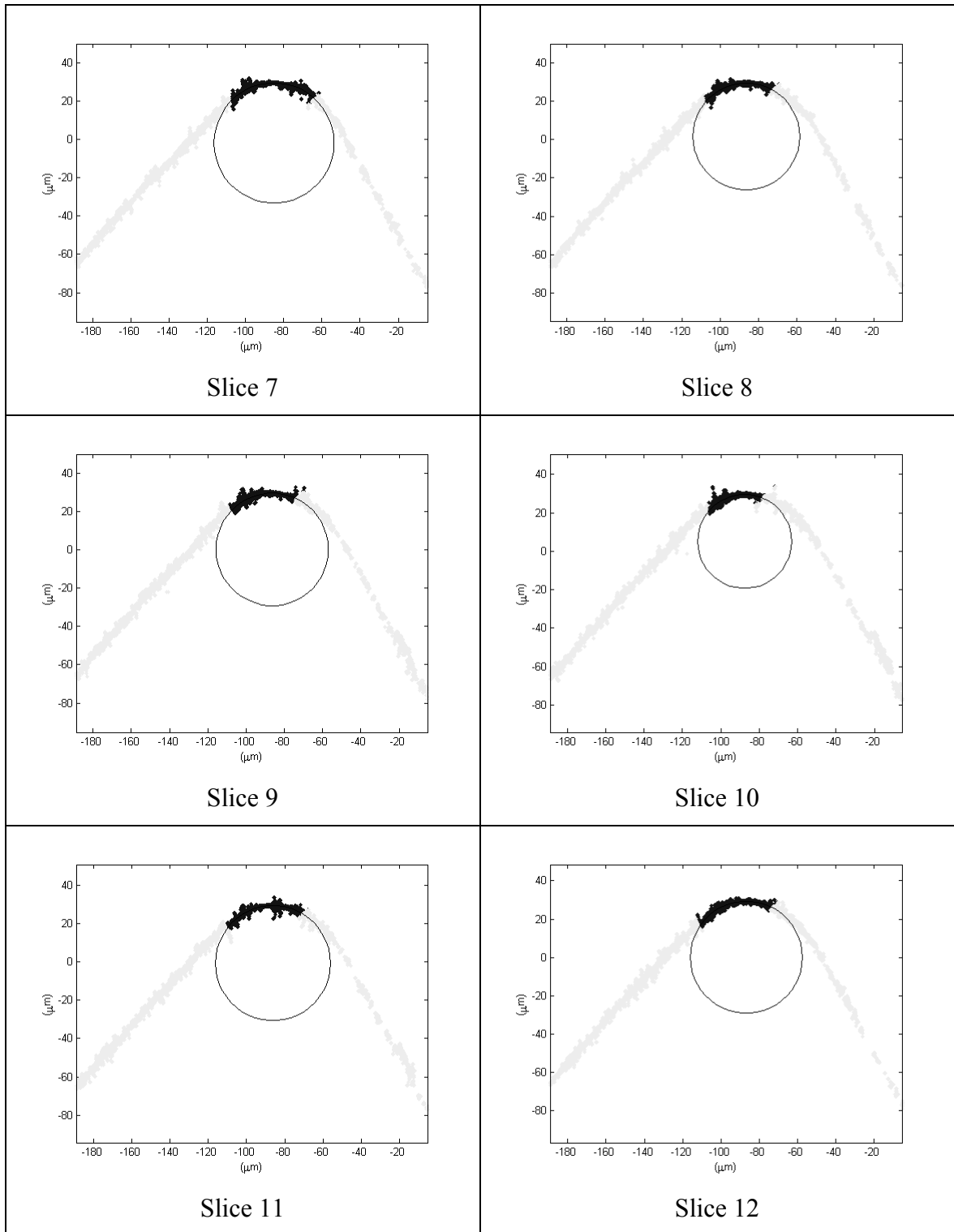


Figure B.2: Slices 7-12 for representative honed data

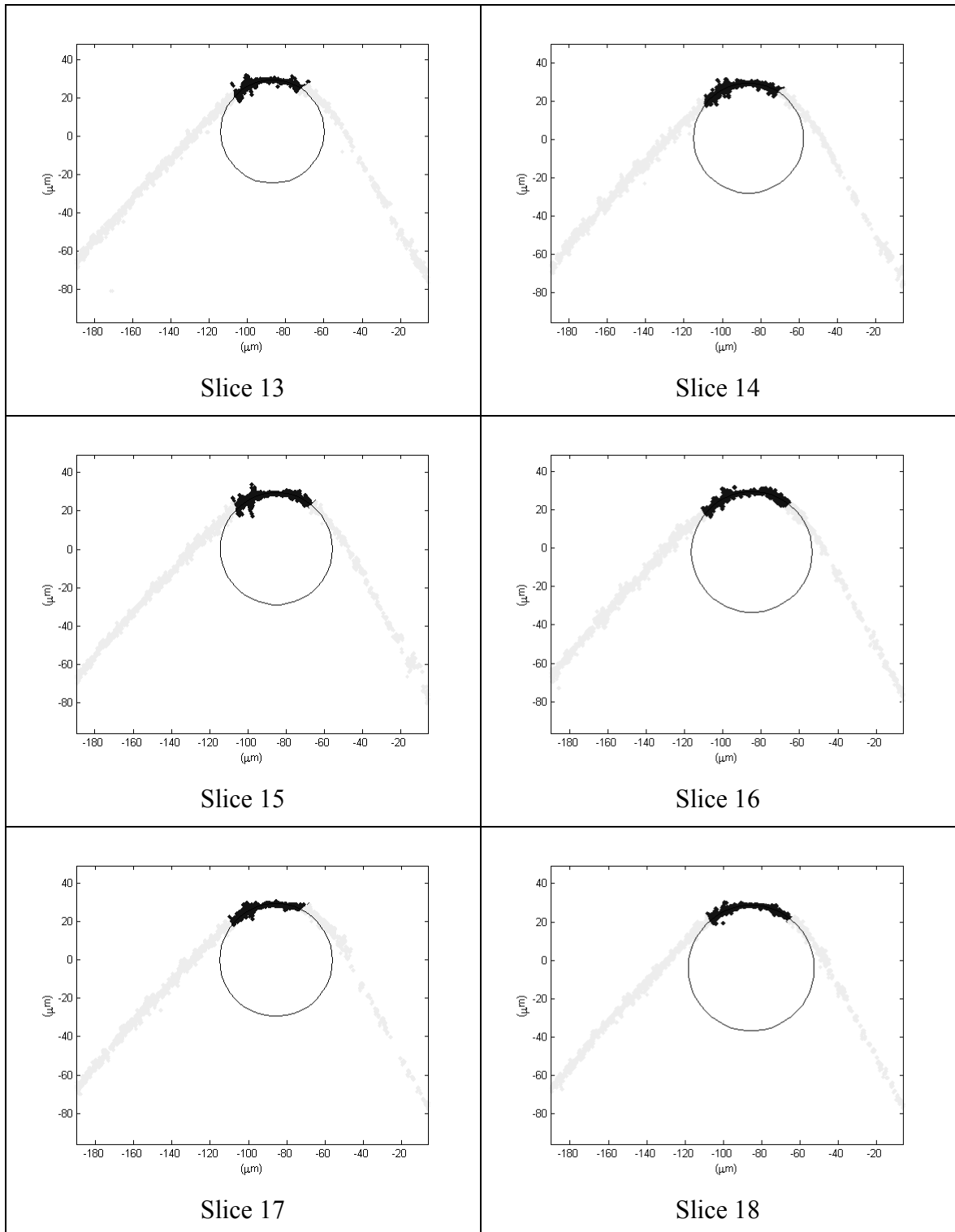


Figure B.3: Slices 13-18 for representative honed data

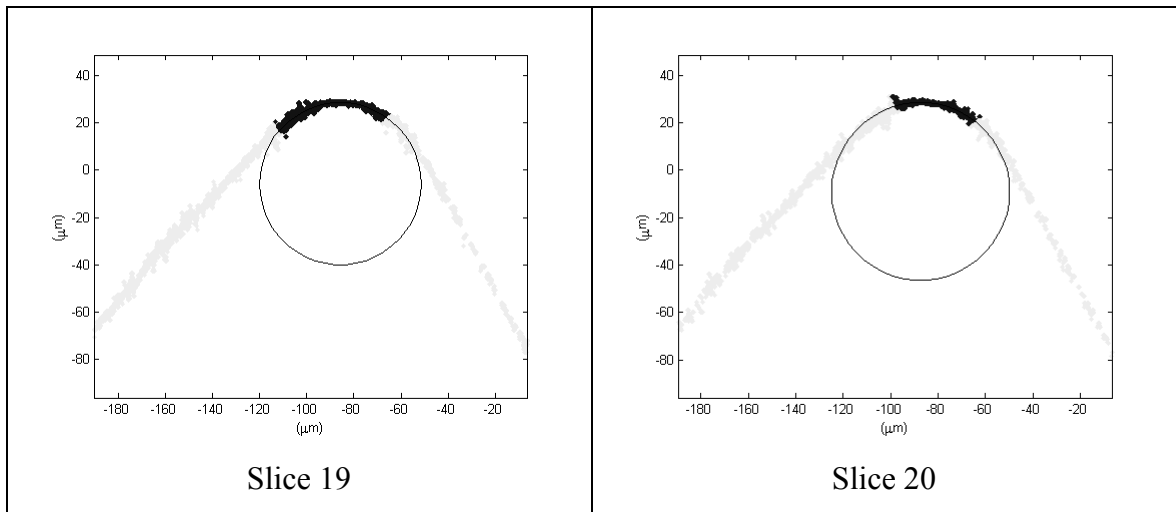


Figure B.4: Slices 19-20 for representative honed data

APPENDIX C: SLA EDGE DATA

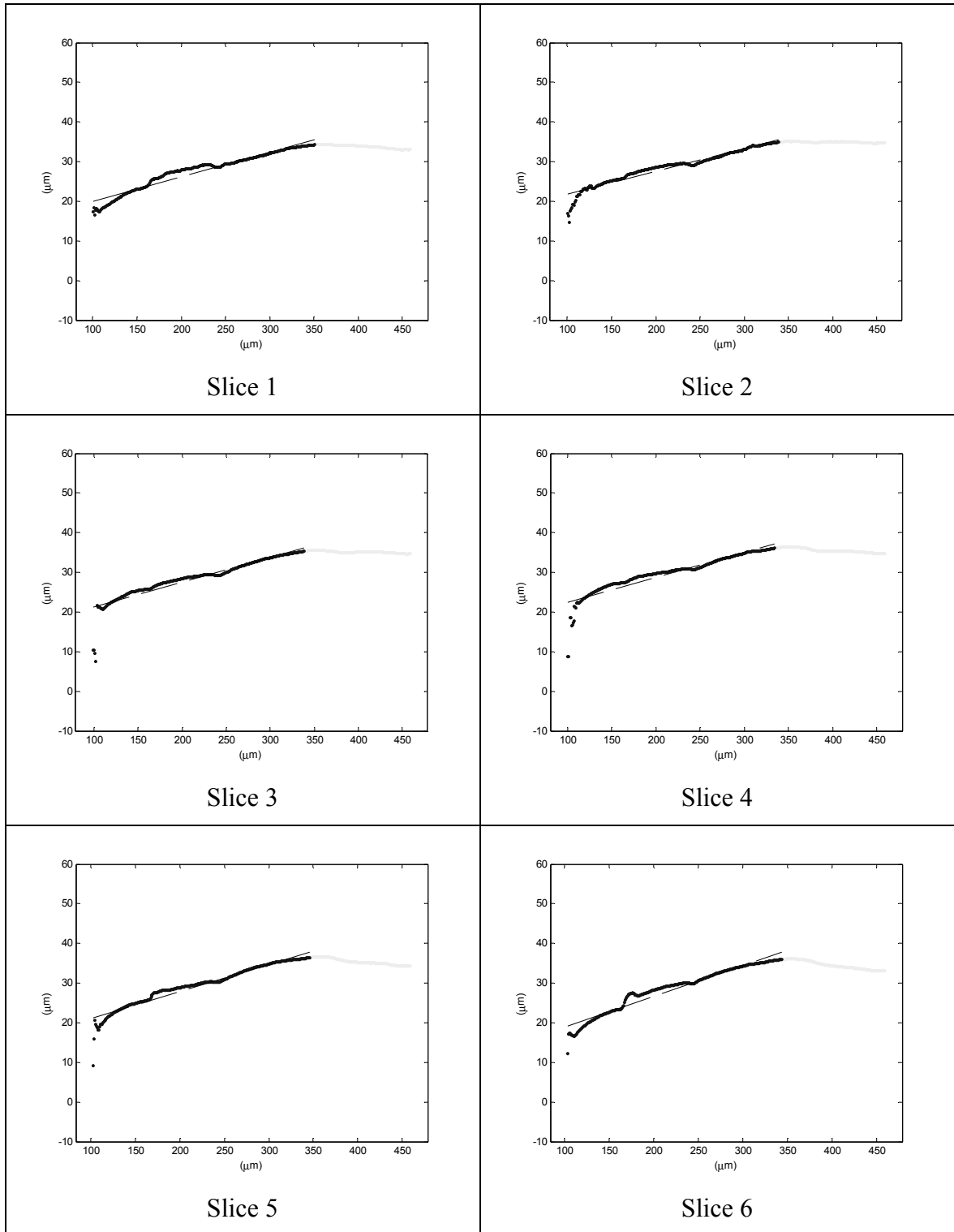


Figure C.1: Slices 1-6 for representative SLA data

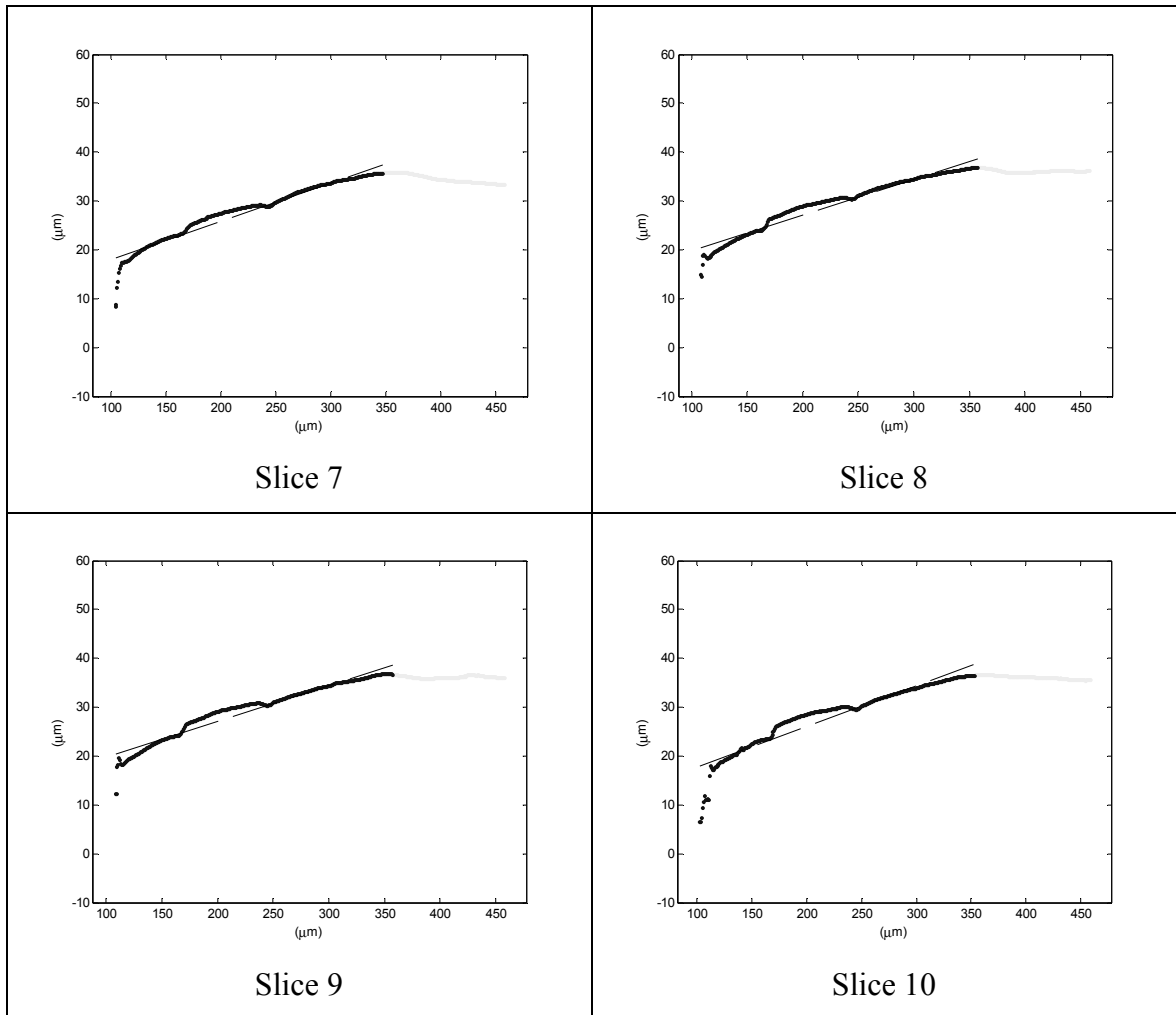


Figure C.2: Slices 7-10 for representative SLA data

REFERENCES

- [1] Shilling, M. Two Dimensional Analysis of Mesoscale Parts using Image Processing Techniques. Master of Science, Georgia Institute of Technology, Atlanta, 2003.
- [2] Ceremuga, J. Obtaining Inspection of High Aspect Ratio Microstructures using a Programmable Optical Microscope. Master of Science, Georgia Institute of Technology, Atlanta, 2003.
- [3] Definition of burr - Merriam-Webster Online Dictionary. Retrieved January 2, 2006 from <http://www.m-w.com/dictionary/burr>.
- [4] Gillespie, L. K. *Deburring and Edge Finishing Handbook*. Dearborn: Society of Manufacturing Engineers, 1999.
- [5] Ohnsorge, J. and Holm, R. *Scanning Electron Microscopy: An Introduction for Physicians and Biologists*. Stuttgart: Georg Thieme Publishers, 1973.
- [6] El-Hakim, S. Some solutions to vision dimensional metrology problems. *Close-Range Photogrammetry Meets Machine Vision*. SPIE 1395, 1990, 480-487.
- [7] Marchman, H. and Dunham, N. AFM: A valid reference tool? *SPIE Metrology, Inspection, and Process Control for Microlithography XIII*. 3332, 1998, 2-9.
- [8] Svetkoff, D. and Kilgus, D. Influence of object structure on the accuracy of 3D systems for metrology. *SPIE Optics, Illumination, and Image Sensing for Machine Vision VI*. 1614, 1991, 218-230.
- [9] VIEW. Voyager 6x12 specifications. 2003. Retrieved February 8, 2004 from <http://www.vieweng.com>.
- [10] Postek, M. Scanning electron microscope metrology. *Proceedings of SPIE - The International Society for Optical Engineering*. CR52, 1994, 46-90.
- [11] Marchman, H. Critical dimension metrology. In *Microlithography: Science and Technology*. New York: Marcel Dekker, Inc., 1998.
- [12] Opsal, J., Chu, H., Wen, Y., Chang, Y. and Li, G. Fundamental solutions for real-time optical CD metrology. *SPIE Metrology, Inspection, and Process Control for Microlithography XVI*. 2002.
- [13] Lagerquist, M., Bither, W. and Brouillette, R. Improving SEM linewidth metrology by two-dimensional scanning force microscopy. *SPIE Metrology, Inspection, and Process Control for Microlithography X*. 2725, 1996, 494-503.

- [14] Marschner, T., Eytan, G. and Dror, O. Determination of best focus and exposure dose using CD-SEM side-wall imaging. *SPIE Metrology, Inspection, and Process Control for Microlithography XV*. 4344, 2001.
- [15] Groot, P. and Deck, L. Surface profiling by frequency-domain analysis of white light interferograms. *Proceedings of SPIE - The International Society for Optical Engineering*. 2248, 1994, 101-104.
- [16] St.Claire, L. and Mirza, A. Metrology for MEMS manufacturing. *Sensors*. 17:7, 2000.
- [17] Wyant, J. White Light Interferometry. *Proceedings of SPIE - The International Society for Optical Engineering*. 4737, 2002, 98-107.
- [18] Zygo Corporation, NewView 5000 specifications. 2003.
- [19] O'Mahony, C., Hill, M., Brunet, M., Duane, R. and Mathewson, A. Characterization of micromechanical structures using white-light interferometry. *Measurement Science and Technology*. 14, 2003, 1807-1814.
- [20] Oles, E. Honed Cutting Tool Inserts, Kennametal. personal communication to Shilling, M., 2006
- [21] Sager, B., Rosen, D. W., Shilling, M. and Kurfess, T. R. Experimental Studies in Stereolithography Resolution. *Solid Freeform Fabrication Symposium*, Austin, 2003.
- [22] Roth, J., Felkel, E. and Groot, P. Optical Metrology. *Proceedings of Machines and Processes for Micro-scale and Meso-scale Fabrication, Metrology, and Assembly*. 2003, 87-92.
- [23] Shilling, M. and Kurfess, T. R. Using White Light Interferometry for Mesoscale Part Inspection. *Proceedings of IMECE*. 2003.
- [24] Corle, T. and Kino, G. *Confocal Scanning Optical Microscopy and Related Imaging Systems*. Academic Press, 1996.
- [25] Sung, L.-P., Jasmin, J., Gu, X., Nguyen, T. and Martin, J. W. Use of Laser Scanning Confocal Microscopy for Characterizing Changes in Film Thickness and Local Surface Morphology of UV-Exposed Polymer Coatings. *JCT Research*. 1:4, 2004, 267-276.
- [26] Uhlmann, E., Oberschmidt, D. and Kunath-Fandri, G. 3D-analysis of microstructures with confocal laser scanning microscopy. *Proceedings of Machines and Processes for Micro-scale and Meso-scale Fabrication, Metrology, and Assembly*. 2003, 93-97.

- [27] ASTM, ASTM Standard Guide for Computed Tomography (CT) Imaging. 1993, Designation: E 1441-93.
- [28] Aracor. Features of Aracor computed tomography systems. 2002. Retrieved February 17, 2004 from <http://www.aracor.com/pages/products/ct.html>.
- [29] Heller, A. Nondestructive characterization at the mesoscale. *Science and Technology Review, Lawrence Livermore National Laboratory*. 2003.
- [30] Martz, H. and Albrecht, G. Nondestructive characterization technologies for metrology of micro/mesoscale assemblies. *Proceedings of Machines and Processes for Micro-scale and Meso-scale Fabrication, Metrology, and Assembly*. 2003, 131-141.
- [31] Simon, M. and Sauerwein, C. Quality control of Light Metal Castings by 3D Computed Tomography. 2001. Retrieved March 6, 2006 from <http://www.ndt.net/article/wcndt00/papers/idn730/idn730.htm>.
- [32] Binnig, G. and Rohrer, H. Scanning tunneling microscopy. *IBM Journal of Research and Development*. 44:1-2, 2000, 179-293.
- [33] Binnig, G., Quate, C. and Gerber, C. Atomic Force Microscopy. *Physical Review Letters*. 56, 1986, 930-933.
- [34] Veeco Instruments, Scanning probe/atomic force microscopy: Technology overview and update. 2003.
- [35] Marchman, H. Nanometer-scale dimensional metrology with noncontact atomic force microscopy. *SPIE Metrology, Inspection, and Process Control for Microlithography X*. 2725, 1996.
- [36] Rizivi, S. and Meyyappan, A. Atomic force microscopy: A diagnostic tool (in) for mask making in the coming years. *SPIE Metrology, Inspection, and Process Control for Microlithography XIII*. 3677, 1999.
- [37] Walch, K., Meyyappan, A., Muckenhirn, S. and Margail, J. Measurement of Sidewall, Line and Line-edge Roughness with Scanning Probe Microscopy. *SPIE Metrology, Inspection, and Process Control for Microlithography XV*. 4344, 2001.
- [38] Meyyappan, A., Klos, M. and Muckenhirn, S. Foot (bottom corner) measurement of a structure with SPM. *SPIE Metrology, Inspection, and Process Control for Microlithography XV*. 4344, 2001, 733-738.
- [39] Griffith, J., Marchman, H., Miller, G. and Hopkins, L. Dimensional metrology with scanning probe microscopes. *Journal of Vacuum Science & Technology*. 13:3, 1995, 1100-1105.
- [40] Rank Taylor Hobson Limited, Form Talysurf Mark 1 Brochure. 1986.

- [41] Oles, E. Edge measurement and standards, Kennametal. personal communication to Shilling, M., 2004
- [42] Sandvik. 940938. Retrieved December 16, 2005 from http://doc.coromant.sandvik.com/cat_drawings/940938.jpg.
- [43] Peggs, G., Lewis, A. and Oldfield, S. Design for a compact high-accuracy CMM. *CIRP Annals - Manufacturing Technology*. 48:1, 1999, 417-420.
- [44] Shiozawa, H., Fukutomi, Y., Ushioda, T. and Yoshimura, S. Development of ultra-precision 3D-CMM based on 3D metrology frame. *Proceedings of ASPE*. 18, 1998, 15-18.
- [45] Peggs, G., Lewis, A. and Leach, R. Measuring in three dimensions at the mesoscopic scale. *Proceedings of Machines and Processes for Micro-scale and Meso-scale Fabrication, Metrology, and Assembly*. 2003, 53-57.
- [46] Cao, S., Brand, U., Kleine-Besten, T., Hoffmann, W., Schwenke, H., Bütefisch, S. and Büttgenbach, S. Recent developments in dimensional metrology for microsystem components. *Microsystems Technologies*. 8, 2002, 3-6.
- [47] Takamasu, K., Hiraki, M., Enami, K. and Ozono, S. Development of nano-CMM and parallel-CMM. *International Dimensional Metrology Workshop*, 1999.
- [48] Ogura, I. and Okazaki, Y. A study of development of small cmm probe detecting contact angle. *ASPE Summer Topical Meeting - Coordinate Measurement Machines*. 2003.
- [49] Takamasu, K., Fujiwara, M., Yamaguchi, A., Hiraki, M. and Ozono, S. Evaluation of thermal drift of nano-CMM. *2nd EUSPEN International Conference*, Turin, 2001.
- [50] Schellekens, P., Haitjema, H. and Pril, W. A silicon-etched probe for 3-D coordinate measurements with an uncertainty below 0.1 μm . *IEEE Transactions on Instrumentation and Measurement*. 50:6, 2001, 1519-1523.
- [51] Seitz, K. F25 Measuring Machine for Microsystem Technology. *Carl Zeiss Innovation SPECIAL Metrology*. 7, 2005, 18-19.
- [52] Chinn, D., Ostendorp, P. and L. Garrett, P. G., M. Haugh, R. Kershmann, T. Kurfess Three Dimensional Imaging of LIGA-Made Micromachines Using Digital Volumetric Imaging. *The Japan - USA Symposium on Flexible Automation*, Hiroshima, 2002.
- [53] Kurfess, T., Chinn, D., Ostendorp, P., Claudet, A. and Tucker, T. Metrology for Micro-Components. *JSME/ASME International Conference on Materials and Processing*, Honolulu, 2002.

- [54] Fan, K., Chu, C. and Mou, J. Development of a low-cost autofocus probe for profile measurement. *Measurement Science and Technology*. 12, 2001, 2137-2146.
- [55] Kirkland, E. A nano coordinate machine for optical dimensional metrology. Master of Science, Georgia Institute of Technology, Atlanta, 2003.
- [56] Kim, B., Razavi, A., Degertekin, L. and Kurfess, T. Micromachined interferometer for MEMS metrology. *Proceedings of Machines and Processes for Micro-scale and Meso-scale Fabrication, Metrology, and Assembly*. 2003, 73-78.
- [57] Schmitt diel, M. Active Control of a Diffraction Grating Interferometer for Microscale Devices. Master of Science, Georgia Institute of Technology, Atlanta, 2004.
- [58] Hall, A. and Degertekin, L. Integrated optical interferometric detection method for micromachined capacitive acoustic transducers. *Applied Physics Letters*. 80, 2002, 3859-3861.
- [59] Rosen, D. Stereolithography Technology. In *Course notes for ME7227, Rapid Prototyping in Engineering*. Atlanta: Georgia Institute of Technology, 2002.
- [60] Madou, M. *Fundamentals of Microfabrication*. Washington DC: CRC Press, 1997.
- [61] Cai, G. Q., Lu, Y. S., Cai, R. and Zheng, H. W. Analysis on Lapping and Polishing Pressure Distribution. *Annals of the CIRP*. 47, 1998, 235-238.
- [62] Aigeldinger, G., Ceremuga, J. T. and Skala, D. M. Large batch dimensional metrology demonstrated in the example of a LIGA fabricated spring. *Microsystem Technologies*. 11:4 - 5, 2005, 379-384.
- [63] Smith, M. and Kowalsky, J. For Good Measure. *Cutting Tool Engineering*. 47:9, 1995, 46-51.
- [64] Varga, G., Balajti, Z., Dud and s, I. Advantages of the CCD camera measurements for profile and wear of cutting tools. *Journal of Physics: Conference Series*. 2005, 159-162.
- [65] Li, X., Rahman, M., Liu, K., Neo, K. and Chan, C. Nano-precision measurement of diamond tool edge radius for wafer fabrication. *Journal of Materials Processing Technology*. 140, 2003, 358-362.
- [66] Lucca, D. A. and Seo, Y. W. Effect of Tool Edge Geometry on Energy Dissipation in Ultraprecision Machining. *Annals of the CIRP*. 42:1, 1993, 83-86.
- [67] Weckenmann, A. and Nalbantic, K. Precision Measuremetn of Cutting Tools with Two Matched Optical 3D-Sensors. *Annals of the CIRP*. 52:1, 2003, 443-446.

- [68] Budinski, K. G. Needs and Applications in Precision Measurement and Monitoring and Wear. *Journal of Testing and Evaluation*. 25:2, 1997, 226-232.
- [69] Dow, T. A. and Scattergood, R. O. Mesoscale and Microscale Manufacturing Processes: Challenges for Materials, Fabrication and Metrology. *Winter Topical Meeting: American Society for Precision Engineering*, 2003.
- [70] Schaller, T., Bohn, L., Mayer, J. and Schubert, K. Microstructure grooves with a width of less than 50 μm cut with ground hard metal micro end mills. *Precision Engineering*. 23:4, 1999, 229-235.
- [71] Lee, K. and Dornfeld, D. A. Micro-burr formation and minimization through process control. *Precision Engineering*. 29:2, 2005, 246-252.
- [72] Stein, J. M. and Dornfeld, D. A. Burr Formation in Drilling Miniature Holes. *Annals of the CIRP*. 46:1, 1997, 63-66.
- [73] Hibbs, A. R. *Confocal Microscopy for Biologists*. New York: Kluwer Academic/Plenum Publishers, 2004.
- [74] Spring, K. R., Fellers, T. K. and Davidson, M. W. Theory of Confocal Microscopy: Resolution and Contrast in Confocal Microscopy. 2004. Retrieved January 22, 2006 from <http://www.olympusconfocal.com/theory/resolutionintro.html>.
- [75] Sheppard, C. J. R. and Shotten, D. M. *Confocal Laser Scanning Microscopy*. BIOS Scientific Publishers Limited, 1997.
- [76] Webb, R. and Dorey, C. K. The pixelated image. In *Handbook of Biological Confocal Microscopy*, 41-51. Pawley, J. B., ed. New York: Plenum, 1990.
- [77] Pawley, J. B. Fundamental and Practical Limits in Confocal Light Microscopy. *Scanning*. 13, 1991, 184-198.
- [78] Pawley, J. B. Sources of Noise in Three-Dimensional Microscopical Data Sets. In *Three-Dimensional Confocal Microscopy: Volume Investigation of Biological Specimens*, 47-93. Stevens, J. K., Mills, L. R. and Trogadis, J. E., ed. New York: Academic Press, 1994.
- [79] Weckenmann, A. and Lorz, J. Monitoring coordinate measuring machines by calibrated parts. *Journal of Physics: Conference Series*. 2005, 190-193.
- [80] Needham, G. H. Micrometry. Calibration and Measurement with The Microscope. In *The practical use of the microscope*, 359-366. Springfield, IL: Charles C. Thomas, 1958.
- [81] Vorburger, T. V., Teague, E. C., Scire, F. E. and Rosberry, F. W. Measurements of Stylus Radii. *Wear*. 57, 1979, 39-49.

- [82] Hubner, U., Morgentroth, W., Meyer, H. G., Sulzbach, T., Brendel, B. and Mirande, W. Downwards to metrology in nanoscale: determination of the AFM tip shape with well-known sharp-edged calibration structures. *Applied Physics*. A76, 2003, 913-917.
- [83] Vesenka, J., Miller, R. and Henderson, E. Three-dimensional probe reconstruction for atomic force microscopy. *Review of Scientific Instruments*. 65:7, 1994, 2249-2251.
- [84] Dixon, R., Schneir, J., McWaid, T., Sullivan, N., Tsai, V. W., Zaidi, S. H. and Brueck, S. R. J. Toward Accurate Linewidth Metrology using Atomic Force Microscopy and Tip Characterization. *Metrology, Inspection, and Process Control for Microlithography X*. 2725, 1996, 589-607.
- [85] McNally, J. G., Cogswell, C. J., Fekete, P. W. and Conchello, J.-A. Comparison of 3D microscopy methods by imaging a well characterized test object. *Three-Dimensional Microscopy: Image Acquisition and Processing IV*, 1997, 52-63.
- [86] Acko, B. Calibration of electronic levels using a special sine bar. *Precision Engineering*. 29:1, 2005, 48-55.
- [87] Griffith, J. E., Marchman, H. M. and Hopkins, L. C. Edge position measurement with a scanning probe microscope. *The 38th international symposium on electron, ion, and photon beams*, New Orleans, 1994.
- [88] Mortenson, M. E. *Geometric Modeling*. New York: John Wiley and Sons, 1997.
- [89] Piegl, L. and Tiller, W. Circles: A Menagerie of Rational B-Spline Circles. *IEEE Computer Graphics and Applications*. 1989, 48-56.
- [90] Lee, E. T. Y. The Rational Bezier Representation for Conics. In *Geometric Modeling: Algorithms and New Trends*, 3-19. Farin, G. E., ed.: SIAM, 1987.
- [91] Bourke, P. Minimum Distance between a Point and a Line. 1988. Retrieved August 3, 2002 from <http://astronomy.swin.edu.au/pbourke/geometry/pointline>.
- [92] Chernov, N. and Lesort, C. Least Squares Fitting of Circles. *Journal of Mathematical Imaging and Vision*. 23, 2005, 239-252.
- [93] Burr, J. T. *Elementary Statistical Quality Control*. New York: Marcel Dekker, 2005.
- [94] Claudet, A. Analysis of Three Dimensional Measurement Data and CAD Models. Doctor of Philosophy, Georgia Institute of Technology, Atlanta, 2001.
- [95] Hattori, M., Kurita, T., Tsutsumi, C. and Kasashima, N. A Study of Measurement and Evaluation of Micro Geometrical Surface. *International Progress on Advanced Optics and Sensors*. 2003, 67-72.

- [96] Dornfeld, D., Ed. *Publications of CODEF: The Consortium on Deburring and Edge Finishing*. 2001.
- [97] Chern, G. Analysis of burr formation and breakout in metal cutting. Ph.D., University of California, Berkeley, 1993.
- [98] Lee, S. H. and Lee, S.-H. Optimisation of cutting parameters for burr minimization in face-milling operations. *International Journal of Production Research*. 41:3, 2003, 497-511.
- [99] Schafer, F. Methods of Defining Edge Condition (Deburring Quality). Dearborn: Society of Manufacturing Engineers, 1977.
- [100] Gillespie, L. K. *Deburring Technology for Improved Manufacturing*. Dearborn: Society of Manufacturing Engineers, 1981.
- [101] Schafer, F. Deburring Processes in Perspective. Dearborn: Society of Manufacturing Engineers, 1975.
- [102] Gillespie, L. K. National Standard for Burr Conditions on Products/Deburring: Deburring a Proposed Product Standard. *Deburring and Surface Conditioning* Cincinnati, 1993.
- [103] Takazawa, K. and Kato, Y. Edge Quality Classification and Grade. *Proceedings of BEST-J*. 3:17, 1997, 45.